General Disclaimer

One or more of the Following Statements may affect this Document

- This document has been reproduced from the best copy furnished by the organizational source. It is being released in the interest of making available as much information as possible.

- This document may contain data, which exceeds the sheet parameters. It was furnished in this condition by the organizational source and is the best copy available.

- This document may contain tone-on-tone or color graphs, charts and/or pictures, which have been reproduced in black and white.

- This document is paginated as submitted by the original source.

- Portions of this document are not fully legible due to the historical nature of some of the material. However, it is the best reproduction available from the original submission.

Produced by the NASA Center for Aerospace Information (CASI)

STUDIES OF ATMOSPHERIC WATER VAPOR BY MEANS OF PASSIVE MICROWAVE TECHNIQUES

NORMAN E. GAUT

TECHNICAL REPORT 467

DECEMBER 20, 1968

MASSACHUSETTS INSTITUTE OF TECHNOLOGY

RESEARCH LABORATORY OF ELECTRONICS

Technical Report 467   December 20, 1968

STUDIES OF ATMOSPHERIC WATER VAPOR BY MEANS OF
PASSIVE MICROWAVE TECHNIQUES

Norman E. Gaut

Abstract

Expressions describing the absorption by water vapor near its two lowest rotational
spectral lines (22.235 GHz and 183.310 GHz) have been developed. These expressions
are used to investigate the absorption from model and real atmospheres. Absorption
measurements taken near the lower frequency line are compared with computed spectra
based on data from simultaneous nearby radiosonde ascents. Comparable spectra
occur only on days of high static stability. The spectral spike which excessive strato-
spheric water vapor might produce was searched for, but not found, in the observed
absorption data. Under reasonable assumptions about the distribution of water vapor in
the stratosphere, this result follows. A method for determining integrated water vapor
using zenith opacity at several frequencies has been derived and evaluated. Estimations
within ±5% of the true values are consistently obtainable. Finally, the statistical scheme
of C. D. Rodgers (Clarendon Laboratory) for inverting spectral data in order to obtain
the vertical distribution of water vapor has been evaluated for 34 radiosondes from
Boston and vicinity. The procedure is shown to be stable against a variety of errors in
the data and statistical assumptions.

PRECEDING PAGE BLANK NOT FILMED

TABLE OF CONTENTS

CONTENTS

I. INTRODUCTION

Important advances in numerical weather prediction have occurred during the last fifteen years. They have paralleled the introduction and rapid improvement of electronic computing machines. Indeed, the advances of both are inextricably related.

The pace of improvement in electronic computers has not slackened. It is reasonable to expect that microelectronics and other innovations will increase the capacity, speed, and versatility of future machines. Numerical weather prediction, however, appears to be on a plateau of achievement that will be substantially unaltered by new opportunities provided by computer technology. It has become apparent that the limiting factor for predicting future weather events (somewhere near two or three days in advance at the present time) is not the speed or capacity for processing data, but the observations to be processed. (See Lorenz[1] for a possible theoretical upper time limit to forecasting the state of the atmosphere.)

One unconventional approach to the data problem involves remote sensing of the atmosphere's properties from artificial satellites of the Earth. It has long been realized that satellites offer unique opportunities for world-wide surveillance of the atmosphere. The simplicity of their orbits, world-wide coverage, the number of observations per day, all combine to provide an ideal observational platform.

Already, weather satellites using television and infrared sensors have widened our knowledge of world-wide cloud formations, cloud-top heights, and through the use of infrared spectrometers have begun to probe the vertical profiles of temperature and water vapor above the clouds. The information so gathered, however, does not provide the necessary data concerning the lower troposphere which are necessary for numerical weather prediction. The cloud-top limit effectively shields the majority of the lower atmosphere from infrared sensors.

In order to circumvent this limitation, attention has been drawn to the microwave region, which extends arbitrarily from millimeter to meter wavelengths. There are important advantages in passively probing the atmosphere in this part of the electromagnetic spectrum rather than in the infrared: (i) clouds are not opaque at these frequencies, thereby making it possible to study the cloud itself and the region below the cloud; and (ii) instrumentation exists whose bandwidth is much smaller than the widths of spectral lines arising from several of the most important atmospheric gases. This last fact allows detailed analysis of line shape, which in turn facilitates the inference of the atmospheric conditions in which the lines arise.

With these possibilities in mind, the purpose of this report is to present a theoretical, numerical, and, whenever possible, observational investigation of the potential meteorological uses of passive microwave measurements in determining the distribution and total amount of atmospheric water vapor.

1

II. THEORETICAL ABSORPTION OF MICROWAVE
RADIATION BY WATER VAPOR

The purpose now is (i) to give sufficient background for understanding the nature of atmospheric absorption arising from pure rotational spectral lines of water vapor, and (ii) to provide expressions of sufficient detail to compute absorption attributable to the two lowest frequency lines, one of which is 22.2 GHz and the other 183.3 GHz.

2.1 PURE ROTATIONAL SPECTRAL LINES OF WATER VAPOR

The energy associated with the motion of a water molecule (illustrated in Fig. 1) is partitioned among its rotational, vibrational, and translational motions. The first two
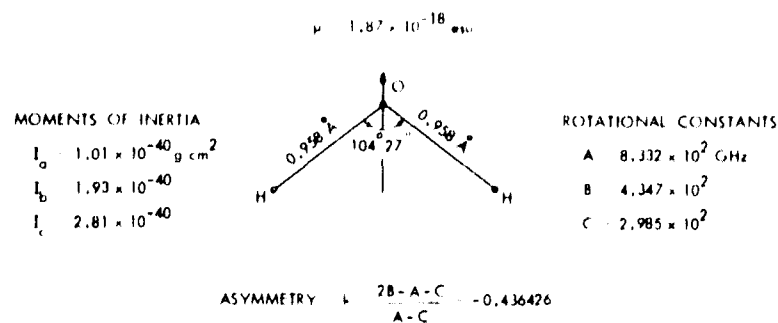
Fig. 1. Geometrical configuration and physical constants of the water-vapor molecule.

modes of motion are quantized. If the molecule is not vibrating, the resulting quantized energy states are called pure rotational energy states. Transitions can occur between some of these states, and thus give rise to spectral lines of absorption if the final state is at a higher energy level than the initial state, or to spectral lines of emission if the final state is at a lower energy level.

Energy states for asymmetric molecules like H_2O, that is, molecules whose three moments of inertia have different values, are designated in one of two ways. In the most explicit method, the quantum number J associated with the total angular momentum is expressed with two subscripts K_{-1} and K_{+1}. These last two numbers are internal quantum numbers associated with limiting prolate and oblate symmetrical molecules rotating in a manner similar to the asymmetric one of interest.

More concise is the J_τ notation. J remains the quantum number associated with the total angular momentum, but it now has a single subscript. This subscript is associated with the order of the energy level in question in the possible $(2J+1)$ levels which can occur for the same total angular momentum. If K_{-1} and K_{+1} are known, τ may always be found from the expression $\tau = K_{-1} + K_{+1}$.

In the $J_{K-1, K+1}$ notation, the transition producing the lowest frequency water-vapor line occurring at 22.2 GHz is denoted $5_{2,3} \rightarrow 6_{1,6}$. The 183.3 GHz line is produced by

the transition between the energy states $2_{1,2} \rightarrow 3_{1,3}$. In the J_τ notation, these transitions are $5_{-1} \rightarrow 6_{-5}$ and $2_{+2} \rightarrow 3_{-2}$, respectively. (For a list of rotational transitions of water vapor resulting in the 53 lowest resonant frequency spectral lines, together with their strengths, initial and final term values, linewidths, and statistical weights, see Appendix A, Table 7.)

2.2 MICROWAVE ABSORPTION COEFFICIENT FOR WATER VAPOR

The general expression for the absorption coefficient resulting from the transition of molecules between the energy states i and j is given (adapted from Eq. 1 of Van Vleck[2]) by

$$\gamma_{ij} = \frac{8\pi^3 \nu}{3hc} \, |F(\nu_{ij}, \nu)| \left\{ N_i |\mu_{ij}|^2 - N_j |\mu_{ji}|^2 \right\}, \tag{1}$$

in which γ_{ij} is the absorption coefficient for the transition $i \rightarrow j$; ν is the frequency of the incident radiation; N_i and N_j are the number densities of molecules in the lower and higher energy states, respectively; $|\mu_{ij}|^2$ is the square of the dipole matrix element associated with the transition $i \rightarrow j$, $F(\nu_{ij}, \nu)$ may be called the "structure" factor or "line-shape" factor for the transition; c is the speed of light, and h is Planck's constant.

2.2.1 Partition Function

The number of molecules in a given state, say the ith, may be found from Boltzmann theory for a gas in thermal equilibrium. For the case of water vapor, N_i may be written

$$N_i = N\, P_i, \tag{2}$$

where N is the total number of absorbing particles per cm^3, and P_i is a number between 0 and 1 which gives the fraction of N in the state i.

For the case of water vapor P_i is given (see Herzberg[3]) by

$$P_i = P_{V_i} P_{R_i}, \tag{3}$$

in which P_{V_i} represents the fraction of all molecules that are in the vibrational state of interest, and P_{R_i} the fraction in the rotational energy state of interest. In Eq. 3 it is assumed that all molecules remain in the electronic ground state.

When P_{V_i} is expanded (see Townes and Schawlow[4]) it is found that for temperatures that occur in the atmosphere below 100 km the great majority of water molecules are in the zero vibrational state. It is this state for which pure rotational energy states are valid, and from which the spectral lines of interest for this report arise. P_{V_i} may be very closely approximated by unity, so that P_i may be taken to be equal to P_{R_i}.

The fraction of molecules in a given rotational state may be expressed (see Townes and Schawlow[4] and their discussion of nuclear spin, or the discussion of G by Van Vleck[5]) as

$$P_{R_i} = \frac{g_{\tau_i}(2J_i+1)\, e^{-E(J_i,\tau_i)/kT}}{\sum\limits_{J}\sum\limits_{\tau} g_{\tau}(2J+1)\, e^{-E(J,\tau)/kT}}. \tag{4}$$

In Eq. 3, the numerator is the Boltzmann factor for the stationary energy state i in the transition $i \to j$ of Eq. 1. The rotational energy associated with the state is given in the J, τ notation. The factor g arises from consideration of the statistical weight of each state because of nuclear spin. It has a value of 1 for even τ, and 3 when τ is odd. The $(2J+1)$ factor exists because the energy does not depend upon the space orientation of the angular momentum J (a $(2J+1)$ degeneracy).

The double sum in the denominator of (3) is called the rotational partition function G and is only a function of the temperature, since the rotational energy states are fixed. An approximation to the sum with its temperature dependence is given by Van Vleck[5] as

$$G = 170\left(\frac{T}{273}\right)^{3/2}. \tag{5}$$
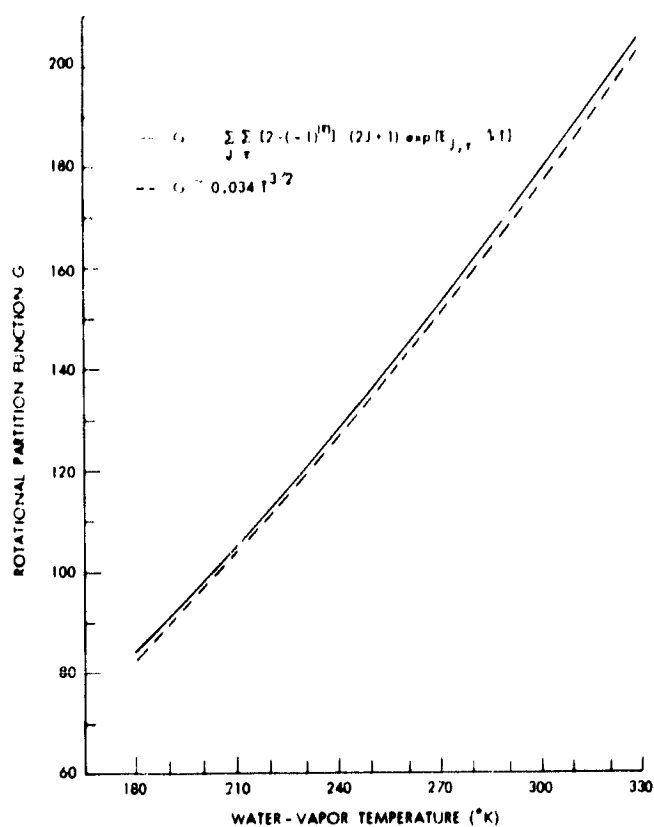
Fig. 2.

Rotational partition function G and the approximation to it by Van Vleck.[5]

A comparison of computations of Eqs. 4 and 5 is presented in Fig. 2. A re-evaluation of the constant in (5) based upon the results above yielded a new value of 172.4. A final form for P_{R_i} with the re-evaluation of G included may be written

$$P_{R_i} = \frac{g_{\tau_i}(2J+1)\, e^{-E(J_i,\tau_i)/kT}}{0.0344\, T^{3/2}} \tag{6}$$

The statistical weights arising from nuclear spin and space quantization factor $(2J+1)$ cause P_R to deviate substantially from a straight Boltzmann distribution for a

4
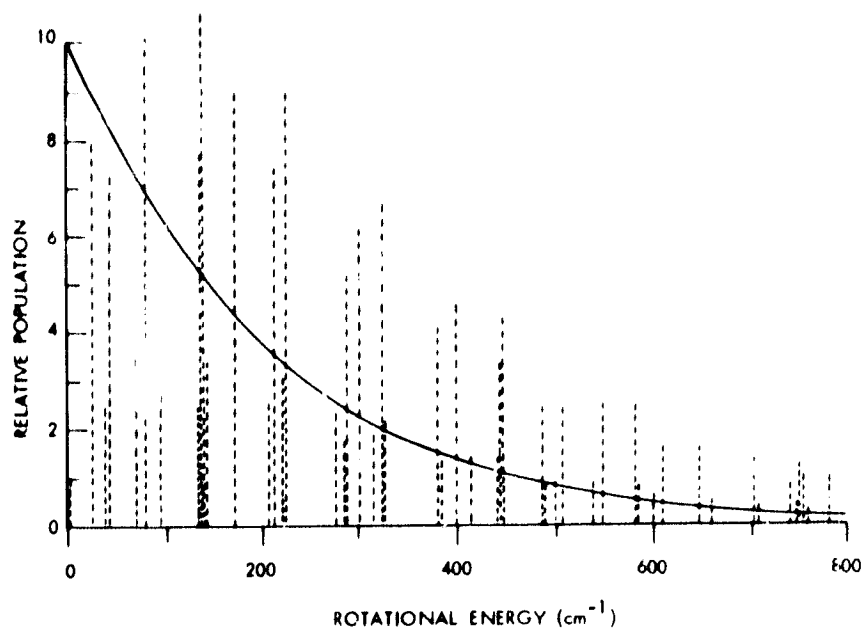
Fig. 3. Relative distribution of water-vapor molecules over the first
52 energy states at 293°K compared with a straight Maxwell-
Boltzmann distribution.

system in thermal equilibrium. Figure 3 presents the relative distribution of molecules
as a function of their energy, together with a straight Boltzmann curve.

2.2.2 Line-Strength Parameter

Explicitly, the value of μ_{ij} used in (1) is given by the solution to the following equation:

$$\mu_{ij} = \int \psi_i \mu \psi_j^* \, d\omega. \tag{7}$$

Here, μ_{ij} refers to a particular transition between states i and j; ψ_i is the wave function for the state i; μ is the permanent dipole moment of the molecule; ψ_j^* is the complex conjugate of the wave function for state j, and ω is the integration variable taken over all possible spatial configurations of the molecule.

The reverse transition, that is j → i, has an effective dipole moment related to μ_{ij} when thermal equilibrium exists as follows.

$$(2J+1)\left|\mu_{ij}\right|^2 = (2J'+1)\left|\mu_{ji}\right|^2, \tag{8}$$

where J and J' are the total angular momentum quantum numbers for the states i and j, respectively.

The so-called "transition strength" more generally describes the two effective dipole moments and is defined as

$$\sum \left|\Phi_{ij}\right|^2 = \frac{\left|\mu_{ij}\right|^2 (2J+1)}{\mu^2}, \tag{9}$$

where the meaning of the symbols is retained from above.

Tabulations of $\Sigma \, |\Phi_{ij}|^2$ for the particular asymmetry of the water-vapor molecule occur in King, Hainer, and Cross.[6] General tables for all asymmetries appear in Wacker and Piatto.[7]

Incorporating Eqs. 6 and 7 in (1), one finds that the absorption coefficient for a single microwave absorption line of water vapor is given by

$$Y_{ij} = \frac{8\pi^3 N\nu}{3hc} \frac{\mu^2 g_{ij} \, \Sigma \, |\Phi_{ij}|^2}{0.0344 \, T^{3/2}} \left\{ e^{-E_i/kT} - e^{-E_j/kT} \right\} \left\{ |F(\nu_{ij}, \nu)| \right\},$$ (10)

where i and j are particular energy states designated by some J, τ and J', τ'.

Since the difference between energy levels which produce microwave spectra must be small, the term in brackets is the difference between terms which are almost equal. To remove this compensation, the following approximation is commonly made:

$$e^{-E_i/kT} - e^{-E_j/kT} \cong e^{-E_i/kT} \left(\frac{h\nu_{ij}}{kT} \right)$$ (11)

It should be emphasized that the temperature T appearing in Eq. 11 is an excitation temperature and is conceptually unrelated to the kinetic temperature of the gas. The approximation made in (11) is valid for $\nu_{ij} \ll 3600$ GHz.

By using Eq. 11, the absorption coefficient may be written

$$Y_{ij} = \frac{8\pi^3 N\nu}{3ckT} \frac{\mu^2 g_{ij} \, \Sigma \, |\Phi_{ij}|^2}{0.0344 \, T^{3/2}} \nu_{ij} \, e^{-E_i/\kappa T} \, |F(\nu_{ij}, \nu)|,$$ (12)

where i now refers to the initial energy state, and N to the total number density of absorbing particles.

2.2.3 Line-Shape Factor

Several mechanisms can broaden a spectral line[4]: the natural linewidth; Doppler effects; collisions between molecules; saturation effects; and collisions with the container of the gas. In the atmosphere, collisional broadening dominates below 70 km. Above this level Doppler broadening is also important.

Derivations of theoretical line shapes for collision-broadened lines have been done by Lorentz,[8] Van Vleck and Weisskopf,[9] Anderson,[10] Ben Reuven,[11] Zhevakin and Naumov,[12] and Gordon,[13] among others. The original work was done by Lorentz who was concerned mainly with spectral lines in the visible region.

Certain conceptual difficulties with the Lorentz line shape led Van Vleck and Weisskopf to alter certain assumptions in the original derivation. The result was more self-consistent. The assumptions as utilized by Van Vleck and Weisskopf were

(i) rotating molecules could be treated as classical oscillators of natural frequency ω_0 driven by the external field to oscillate at ω; and (ii) collisions between rotating molecules leave the phases of the oscillators constrained by the external field to a Boltzmann distribution for thermal equilibrium. By using these assumptions, the line-shape factor can be expressed as

$$F(\nu_{ij}, \nu) = \frac{\nu}{\pi \nu_{ij}} \left[\frac{\Delta\nu}{(\nu_{ij} - \nu)^2 + \Delta\nu^2} + \frac{\Delta\nu}{(\nu_{ij} + \nu)^2 + \Delta\nu^2} \right], \tag{13}$$

where ν is the frequency of penetrating radiation, ν_{ij} the resonant frequency of the molecule, and $\Delta\nu$ the half-width of the line at half-maximum intensity.

The line shape mentioned above was shown to qualitatively describe the shape of spectral lines. Experimental work[12, 14-17] showed, however, several shortcomings to the quantitative fit between theoretical and observational line shapes. Several of the shortcomings of Eq. 13 are the following.

1. If the shape is quantitatively accurate near resonance, the wings of spectral lines are not accurately represented.

2. As higher pressures are encountered, the resonant frequency tends to shift toward lower frequencies, an effect unobtainable from Eq. 13.

3. The linewidth per unit pressure is not constant over all pressures so that the use of (13) is applicable only in the pressure region in which binary collisions occur.

Despite its shortcomings, however, the Van Vleck-Weisskopf line shape is adequate for most atmospheric work, and because more sophisticated line shapes have not yet shown better agreement with experimental results, it will be used throughout the rest of this report.

In order to provide some feeling for the problems associated with the Van Vleck-Weisskopf line shape, Figs. 4 and 5 are included. The circled dots in Fig. 4 represent the data from an experiment conducted by Becker and Autler[16] to fix the shape of the 1.35-cm resonance. The lower solid line represents the theoretical line from the Van Vleck-Weisskopf expression with the effect of all lines at higher frequencies taken as originally estimated by Van Vleck. The upper solid curve has the same expression for the resonant term but has the effect of the higher frequency lines multiplied by a factor of six.

Near 183.3 GHz, a similar situation to the 1.35-cm region is found. Frenkel and Woods[17] have made measurements with a Fabry-Perot type of resonant transmission cavity to determine the line shape. Their conclusions are that near resonance a Lorentzian line shape which is also consistent with the theory of Van Vleck and Weisskopf is justified, but in the wings the theoretically predicted effect of other lines is too low by at least a factor of from 4 to 5. Figure 5 compares the results of Frenkel and Woods with two variations of calculated Van Vleck-Weisskopf line profiles.
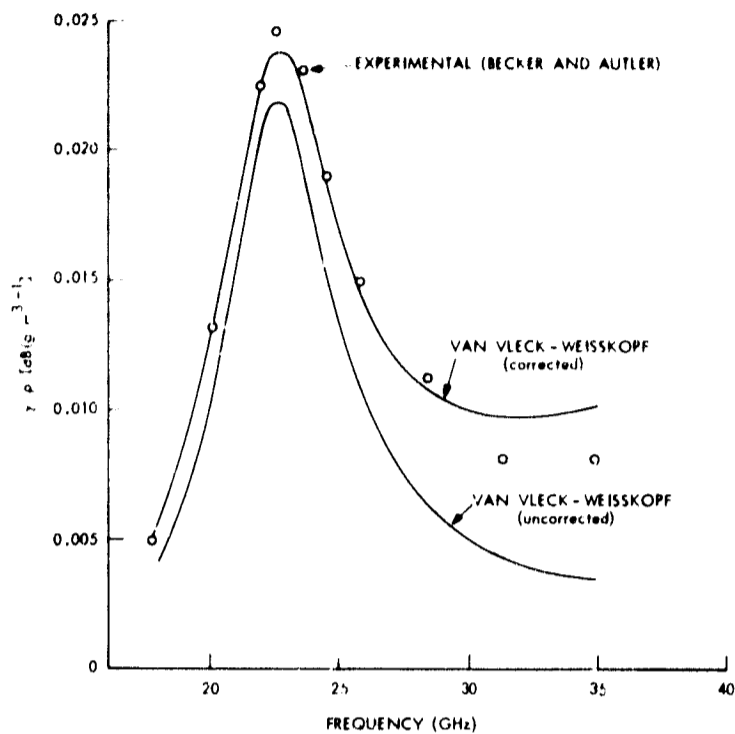
Fig. 4.

Two theoretical representations of the 22 GHz resonance of water vapor compared with experimental data: Van Vleck with the nonresonant term multiplied by a factor of six; and Van Vleck with no correction to the nonresonant term.
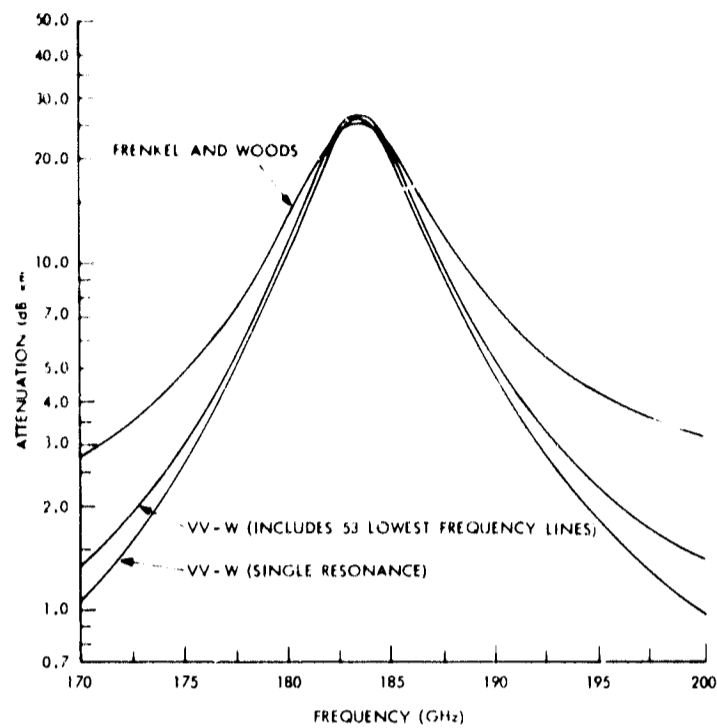
Fig. 5.

Comparison of absorption near the 183-GHz water-vapor rotational line as predicted by the Van Vleck-Weisskopf single-resonance expression, the Van Vleck-Weisskopf expression considering the first 53 water-vapor rotational resonances, and the Frenkel and Woods empirical formula. Conditions in the gas: 1000 mb nitrogen; 7.23 g/m^3 water vapor (7.50 mm Hg); temperature 300°K.

2.2.4 Linewidth Parameter

Of the several mechanisms that can cause spectral-line broadening, only Doppler and collisional broadening are important for atmospheric studies.

Doppler broadening occurs because molecules are moving along the direction of propagation of the radiation. There is a frequency shift of $\pm \nu\left(\dfrac{v}{v_p}\right)$, where ν is the frequency of the radiation, v is the speed of the absorbing molecule along the line of sight, and v_p is the phase speed of the radiation, very close to the speed of light in most cases. When translated to a change in intensity, it is found[4] that the half-width of the Doppler-broadened spectral line is given by

$$\Delta\nu_D = 3.581 \times 10^{-7} \left(\frac{T}{M}\right)^{1/2} \nu \quad sec^{-1}, \tag{14}$$

where T is the temperature in °K, M is the molecular weight, ν is the frequency of the penetrating radiation in sec^{-1}, and it is assumed that the molecular velocities are distributed according to conditions of thermal equilibrium.

8

The exact treatment of the problems of collisional broadening requires detailed knowledge of the interacting forces and processes occurring during collisions, not all of which are well known. Anderson's[10] formulation for computing linewidths has been the basis for the study of the spectra of several molecules including water vapor. Extension of Anderson's theory by Gordon has brought excellent agreement between experiment and theory with the line shape of oxygen at high pressures. This more sophisticated theory has still not been applied to water vapor and, therefore, the functional dependence of the linewidth on atmospheric parameters is based on the work of Anderson and on empirical facts.

The first empirical fact is in accordance with physical intuition: When binary collisions are the dominant interaction, the width of a spectral line is observed to be directly proportional to the number of particles colliding. $\Delta\nu$ is therefore proportional to the pressure over a wide range of values; for water vapor, from a few millimeters of mercury to more than one atmosphere.

The temperature dependence of $\Delta\nu$ is much more difficult to predict theoretically than its pressure dependence. Normally, for temperatures of meteorological interest, it is assumed that $\Delta\nu$ follows a power law of T of the form

$$\Delta\nu \propto T^{-n}, \tag{15}$$

where n for atmospheric gases is in the range from -0.2 to $+1.2$. Actual theoretical prediction, however, of linewidths and their variation with temperature (see Benedict and Kaplan[20,24]) cast doubt upon the exactness of (15). Nevertheless, because (15) does approximate the behavior of $\Delta\nu$ with temperature and a more precise dependence is not available, the power-law temperature dependence is generally retained.

The widths of different spectral lines at constant temperature and pressure are found to depend upon the rotational states of the molecule before and after transition, and upon the perturbing potential of the molecule causing the transition. Moreover, it is predicted and it is observed that a molecule is much more effective in perturbing an identical molecule than some foreign species.

If we draw together the information above, the result is Eq. 16 for the dependence of $\Delta\nu$ on pressure, temperature, and the density of water vapor:

$$\Delta\nu = S\frac{P}{1013.25}\left(\frac{T}{300}\right)^{-n}\left(1 + a\frac{e}{P}\right). \tag{16}$$

In (16), S is the breadth of the line at 1 atm pressure, 300°K temperature, and an infinitesimal amount of water vapor; n is the exponent describing the temperature dependence; T is the ambient temperature in °K; P is the total pressure in mb; e is the partial pressure of water vapor in mb; and a is a factor that is a measure of the increased effectiveness of H_2O molecules for broadening water-vapor lines over the foreign gas broadeners that determine S.

9

2.3 ABSORPTION COEFFICIENT FOR THE WATER-VAPOR ROTATIONAL RESONANCE CENTERED AT 22.2 GHz

It has long been customary to think of the absorption coefficient in terms of linear combinations of separate spectral lines. Contributions to the absorption near resonance have consequently been written as

$$\gamma = \gamma_{RES} + \gamma_{NON}, \tag{17}$$

where γ_{RES} and γ_{NON} are separate and unrelated, and refer to the contribution of the line that is being studied and to the contribution from all other lines, respectively.

In light of the work by Gordon[13] this is not satisfactory for strongly overlapping lines. The 22.2-GHz line is, however, almost an order of magnitude in frequency below the next water-vapor line (183 GHz); therefore, even from Gordon's work, it appears that (17) is valid.

We therefore write

$$\gamma_{1.35} = (\gamma_{RES})_{1.35} + (\gamma_{NON})_{1.35}. \tag{18}$$

Consider the resonant term first. From Eqs. 12 and 13, $(\gamma_{RES})_{1.35}$ may be written in complete form as

$$(\gamma_{RES})_{1.35} = \frac{8\pi^2 \nu^2 N}{3ckT} \frac{\mu_{H_2O}^2 g_o \Sigma |\Phi_{1.35}|^2}{0.0344\ T^{3/2}} e^{-E_{5_{-1}}/kT}$$

$$\left\{ \frac{\Delta\nu}{(\nu_{1.35}-\nu)^2 + \Delta\nu^2} + \frac{\Delta\nu}{(\nu_{1.35}+\nu)^2 + \Delta\nu^2} \right\}, \tag{19}$$

where $\Delta\nu_{1.35}$ is given by Eq. 16 as

$$\Delta\nu_{1.35} = \int_{1.35} \frac{P}{1013.25} \left(\frac{T}{300}\right)^{-n_{1.35}} \left(1 + a_{1.35} \frac{\rho_{H_2O} T}{P}\right). \tag{20}$$

$(\gamma_{RES})_{1.35}$ is given in nepers/cm when ν is in Hz, N is in particles/cm^3, the speed of light, c, is in cm/sec, Boltzmann's constant, k, equals 1.3804×10^{-16} ergs/°K, the kinetic temperature T is in °K, total atmospheric pressure is in mb, water vapor density is in ι ^{3}, and the molecular parameters are used as they appear in Table 1.

Only $a_{1.}$ needs further explanation. The value of the linewidth in the Becker and Autler experim varied linearly with the water-vapor density. When extrapolated to zero water-vapor density, $\Delta\nu$ was found to be 0.087 cm^{-1}, while for a water-vapor density of 50 g/m^3 it was found to have a value of 0.107 cm^{-1}. By assuming that each water-vapor molecule that was substituted for an air molecule is more effective in the

Table 1. Values and sources for the parameters of Eqs. 19 and 20 for $(\gamma_{RES})_{1.35}$.

Parameter	Value	Theoretical or Measured	Source
μ_{H_2O}	1.87×10^{-18} e.s.u.	M	18
g_o	3	τ odd	
$\Sigma \left|\Phi_{1.35}\right|^2$	0.0549	T	6
$E_{5_{-1}}/C$	446.39 cm^{-1}	M	27
$\nu_{1.35}$	$(22.237 \pm .005) \times 10^9$ Hz	M	19
$S_{1.35}$	2.70×10^9 Hz/atm	M	16
$n_{1.35}$	0.626	T	20
$\alpha_{1.35}$	1.46×10^{-2} mb$(g/m^3)^{-1}$ $(°K)^{-1}$	M	16

process by some factor $\eta_{1.35}$, it is not difficult to show, with the aid of the Becker and Autler data, that a correction of the form used in Eq. 20, with a value of $\alpha_{1.35}$ as presented in Table 1, is justified. The value of $\eta_{1.35}$ is approximately 4.2.

The detailed expression for the nonresonant part of Eq. 18 is much less satisfactory than (19) and (20). Van Vleck[5] offers the approximation to this contribution as

$$(\gamma_{NON})_{1.35} = \frac{8\pi^2 \nu^2 N}{3ckT} \mu_{H_2O}^2 \sum_{ij} g\tau_i \sum \left|\Phi_{ij}\right|^2 e^{-E_i/kT} \frac{2\Delta\nu}{\nu_{ij}^2}, \tag{21}$$

where the indices i, j range over all of the spectral lines above the 22.2-GHz resonance, and each parameter is appropriately chosen for a given resonance i,j. The approximation of $F(\nu_{ij}, \nu)$ as $2\Delta\nu/\nu_{ij}^2$ should be valid when $\nu_{ij} \gg \nu$ and $\nu_{ij} \gg \Delta\nu$, both of which are true for resonances other than the 22.2-GHz line. An approximation of the sum over rotational states was given by Van Vleck[21] at 293°K as

$$(\gamma_{NON})_{1.35} = \frac{0.012 \, \rho_{H_2O} \frac{\Delta\nu}{c}}{\lambda^2} \text{ dB/km}, \tag{22}$$

which transposes into our notation as

11

$$(\gamma_{NON})_{1.35} = 2.21 \times 10^{-3} \frac{\rho_{H_2O} {\nu'}^2 \Delta\nu'}{T^{3/2}} \quad dB/km, \tag{23}$$

where primed frequencies are in GHz, and the temperature dependence has been given in Van Vleck.[21]

The expression (21) has already been shown to be too small by a factor of 4 to 6 (see Fig. 4); therefore, hereafter in this report Eq. 23 will be increased by a factor of five.

For convenience, Eqs. 19, 20, and 23, the last with the factor of five included, are reduced to their simplest forms and combined into the two following equations. In each case more familiar inputs replace less familiar ones and all constants are evaluated.

$$\gamma_{1.35} = (\gamma_{RES})_{1.35} + (\gamma_{NON})_{1.35} = 1.570 \times 10^3 \frac{\rho_{H_2O} {\nu'}^2 e^{-642/T}}{T^{5/2}}$$

$$\left\{ \frac{\Delta\nu'_{1.35}}{(\nu'_{1.35} - \nu')^2 + \Delta\nu'^2_{1.35}} + \frac{\Delta\nu'_{1.35}}{(\nu'_{1.35} + \nu')^2 + \Delta\nu'^2_{1.35}} \right\} + 1.11 \times 10^{-2} \frac{\rho_{H_2O} {\nu'}^2 \Delta\nu'_{1.35}}{T^{3/2}} \quad dB/km \tag{24}$$

$$\Delta\nu'_{1.35} = 2.62 \left(\frac{P}{1013.25} \right) \left(\frac{T}{300} \right)^{-0.626} \left\{ 1 + 0.046 \frac{\rho_{H_2O} T}{P} \right\} \quad GHz \tag{25}$$

Primed frequencies are in GHz, ρ_{H_2O} is in g/m^3, temperature is in °K, and total pressure P is in mb.

2.4 ABSORPTION COEFFICIENT FOR THE WATER-VAPOR ROTATIONAL RESONANCE CENTERED AT 183.3 GHz

The nearest line to the 1.35-cm line occurs at 1.64 mm (183 GHz) removed by a factor of eight in frequency. Toward even higher frequencies, we find that in the interval between the 1.64-mm line and eight times its resonant frequency 53 other water-vapor resonances appear. We shall now develop a usable expression for this second lowest frequency water-vapor rotational resonance.

There appears to be no reason why the line shape near resonance will be better fitted by any other than the Van Vleck-Weisskopf formulation. Therefore, it is retained. The equation for the resonance at 183 GHz may be written, analogously to Eqs. 19 and 20 as

Table 2. Various parameters associated with the 183-GHz water-vapor rotational line as reported from several sources. Parentheses indicates derived values; measured values are without parentheses. K. H. C. refers to King, Hainer, Cross[6] line strength.

Molecules	Temperature (°K)	$\left(\gamma/\rho_{H_2O}\right)_{RES} \dfrac{db}{km} \left(\dfrac{g}{m^3}\right)^{-1} (atm)^{-1}$	$\Delta\nu/P$ MHz/mm Hg	% H_2O	n	Source
$H_2O - N_2$	300°K	(3.81) K.H.C.	3.76	0		(22)
	300	(3.38) K.H.C.	4.24	0	0.649	(20) (24)
	300	(3.21)	4.4	0		(17)
	300		3.54	0	0.736	(23)
	301.5	3.00		0		(23)
$H_2O - O_2$	300		2.72	0		(22)
	302.5	4.30	2.62	0		(23)
$H_2O - $ Air	300		19.06	100	1.2	(22)
	300		19.0	100		(17)
	300		(19.5)	100	0.90	(24)
$H_2O - $ Air	300	(4.00) K.H.C.	(3.52)	0		(23)
	300	(3.76) K.H.C.	(3.79)	0	0.649	(20) (24)
	302	(3.28)	(3.27)	0		(23)

$$(\gamma_{RES})_{0.164} = \frac{8\pi^2 \nu^2 N}{3ckT} \mu_{H_2O}^2 g_e \sum |\Phi_{0.164}|^2 e^{-E_{2_{+2}}/kT}$$

$$\left\{\frac{\Delta\nu_{0.164}}{(\nu_{0.164}-\nu)^2 + \Delta\nu_{0.164}^2} + \frac{\Delta\nu_{0.164}}{(\nu_{0.164}-\nu)^2 + \Delta\nu_{0.164}^2}\right\}, \tag{26}$$

where $\Delta\nu$ for this case is given by

$$\Delta\nu_{0.164} = S_{0.164}\left(\frac{P}{1013.25}\right)\left(\frac{T}{300}\right)^{-n_{0.164}}\left\{1 + a_{0.164}\frac{\rho_{H_2O}T}{P}\right\}. \tag{27}$$

The choice of values for the molecular parameters in the case of air broadening is more difficult for the 183-GHz resonance, however, than for the 22-GHz line. Table 2 draws together all the information on the 183-GHz line for the various broadeners that make up air, and presents the derived (and in one case measured) parameters for an air-water vapor mixture. There are many conflicting measurements and values in Table 2 and the final choices must be based on judicious, but unavoidably subjective, reasoning.

We start by choosing the theoretical line strengths as computed by King, Hainer, and Cross.[6] No substantial uncertainties have been presented to throw doubt on these results. This choice, together with the other well-known molecular parameters of (26) (that is, $\mu_{H_2O}^2$, g_e, $E_{2_{+2}}$, k, c, $\nu_{0.164}$) leaves the main uncertainties with $S_{0.164}$, $n_{0.164}$, and $a_{0.164}$ all connected with the linewidth parameter.

The most precise measurements for the linewidth appear to have been done by Rusk,[22] for nitrogen, oxygen, and self-broadening. The derived value of $\Delta\nu$ for air from that work (equal to 3.52 MHz/mm Hg) is the choice we make for $S_{0.164}$.

The most difficult parameter to choose a value for is $n_{0.164}$. Benedict and Kaplan[20] computed this value for nitrogen broadening as 0.649. Hemmi[23] measured this value in nitrogen with about 1% water vapor present as 0.579, and computed the nitrogen value alone from those measurements as 0.736. This last value agrees quite well with the Benedict and Kaplan estimate. Values of the temperature exponent for oxygen, were not reported by Benedict and Kaplan,[24] and in Hemmi these values show no resemblance to a power law of T. (See Supplement.[22] Rusk did measure a value for $n_{0.164}$ for the case of water vapor self-broadening as 1.2.)

A highly convincing choice for $n_{0.164}$ for air from all of these reports is not possible. Since it appears, however, that both oxygen and water vapor have values of n greater than that for nitrogen alone, it would appear that a value near 0.70 would be a defensible estimate. In any case, that is the value that we choose. For a rough idea of the error involved in this exponent, it can be remembered that if the value of $\Delta\nu$ is measured with perfect accuracy at 300°K and the power law is used to extrapolate to,

say, 250°K, a discrepancy of 3.5% occurs between values computed by using $n_{0.164} = 0.6$ and $n_{0.164} = 0.8$.

The value of $n_{0.164}$ may be obtained by using the following reasoning: The effective collision cross section for two gases may be written

$$\sigma_e = \sigma_1 R_1 + \sigma_2(1-R_1), \qquad (28)$$

in which σ_e is the effective cross section, σ_1 is the collision cross section for gas 1, R_1 is its fraction of the total molecules, and σ_2 is the collision cross section for gas 2. The cross section for collisions is directly proportional to the linewidth for a given gas. Therefore, we can write

$$\Delta\nu_e = \Delta\nu_{H_2O-H_2O}R_{H_2O} + \Delta\nu_{H_2O-AIR}(1-R_{H_2O}). \qquad (29)$$

From the data of Rusk,

$$\frac{\Delta\nu_{H_2O-H_2O}}{\Delta\nu_{H_2O-AIR}} = \frac{19.06}{3.52} = 5.4,$$

where $\Delta\nu_{H_2O-AIR}$ is the linewidth with negligible water vapor in the mixture. For 50 g/m^3 of water vapor in 1 atm total pressure of air, a temperature of 318°K, $R_{H_2O} = 0.0724$. Therefore,

$$\frac{(\Delta\nu)_{\rho=50}}{(\Delta\nu)_{\rho=0}} = \frac{\Delta\nu_{H_2O-H_2O}R_{H_2O} + \Delta\nu_{H_2O-AIR}\left(1-R_{H_2O}\right)}{\Delta\nu_{H_2O-AIR}}$$

$$= \frac{1}{1 + a_{0.164}\rho_{50} T/P}. \qquad (30)$$

Solving for $a_{0.164}$ in Eq. 30 results in a value equal to 2.03×10^{-2} mb (g/m^3)$^{-1}$ (°K)$^{-1}$.

Table 3 collects the values for the molecular parameters of the 1.64-mm line which we use in Eqs. 26 and 27. If cgs units are used for general constants, and ν is given in Hz, N in particles/cm^3, pressure P in mb, temperature T in °K, and water-vapor density ρ_{H_2O} in g/cm^3, then, by using the values listed in Table 3, $\Delta\nu_{0.164}$ is given in Hz and $(\gamma_{RES})_{0.164}$ in nepers/cm.

Note that by using 2.68 GHz/atm for the linewidth per unit pressure and the King, Hainer, and Cross line strength, the value of $(\gamma_{RES})_{0.164}/\rho_{H_2O}$ at 1 atm pressure and 300°K is 19% higher than the same parameter estimated by Hemmi from his measurements on nitrogen and oxygen. This is true despite the estimation in Hemmi that $\Delta\nu/P$ for air is 2.48 GHz/atm. If Hemmi's measurements are correct, it would mean that the true line strength is actually 25% smaller than that computed by King, Hainer, and Cross.

Table 3. Values and sources for molecular parameters needed to compute $(\gamma_{RES})_{0.164}$.

Parameter	Value	Theoretical or Measured	Source
μ_{H_2O}	1.87×10^{-18} e. s. u.	M	18
g_e	1	τ even	
$\Sigma \lvert \Phi_{0.164} \rvert^2$	0.1015	T	6
$E_{2_{+2}}/C$	136.15 cm^{-1}	M	27
$\nu_{0.164}$	$183,310.12 \pm 0.10 \times 10^{6}$ Hz	M	22
$S_{0.164}$	2.68×10^{9} Hz/atm	M	22
$n_{0.164}$	0.70		20, 22, 23
$a_{0.164}$	2.03×10^{-2} mb(g/m^3)$^{-1}$ (°K)$^{-1}$	T	22

Only Frenkel and Woods[17] have attacked the nonresonant absorption dilemma and achieved results that can be considered as reliable. But these measurements were done with nitrogen and water vapor only, so there is no direct analogy with air broadening. Nevertheless, so sparse is quantitative data in the region around 183 GHz that we shall rely heavily on the results and procedures in Frenkel and Woods.

As was pointed out, the nonresonant absorption in and around the 183 GHz line was handled by Frenkel and Woods by using the resonant expression for the nearest higher line of consequence (324 GHz) and an empirically determined function proportional to ν^2 for the contributions of all remaining lines. [Note: There are actually two lines very near to 324 GHz. One, however, has a term value for the lower state equal to 1283 cm^{-1}. The Boltzmann population factor is consequently proportional to $\exp[-1283 \, c/kT]$, a value which, at 300°K, is more than 450 times smaller than the Boltzmann factor for the 183-GHz line. This line $(9_{-3} \rightarrow 10_{-7})$ will be disregarded in favor of the line arising from the $4_0 \rightarrow 5_{-4}$ transition. Its lower term value of 326.5 cm^{-1} which, at 300°K, causes the population, when in thermal equilibrium, to be less than that of the lower energy state for the 183-GHz line by a factor of 4 to 5. It will be the line that we refer to as the 324-GHz line or 0.093-cm resonance.] We shall do the same; however, to be consistent with $(\gamma_{RES})_{0.164}$, the 324-GHz line parameters will be those determined from theory and applied to an equation of the form used for

$(\gamma_{RES})_{1.35}$ and $(\gamma_{RES})_{0.164}$ (Eqs. 19 and 26). The equation for the contribution of the remaining lines will be slightly modified from the Frenkel and Woods expressio.. $(\gamma_{NON})_{0.164}$ will therefore be given by

$$(\gamma_{NON})_{0.164} = \frac{8\pi^2\nu^2 N}{3ckT} \frac{\mu^2_{H_2O}g_e \Sigma |\Phi_{0.164}|^2}{0.0344\, T^{3/2}} e^{-E_{4_0}/kT}$$

$$\left\{ \frac{\Delta\nu_{0.093}}{(\nu_{0.093}-\nu)^2 + \Delta\nu^2_{0.093}} + \frac{\Delta\nu_{0.093}}{(\nu_{0.093}+\nu)^2 + \Delta\nu^2_{0.093}} \right\}$$

$$+ C_3 \frac{\nu^2}{(\nu_{0.164})^3} \left(\Delta\nu^w_{wv}+\Delta\nu^w_N\right) \left(\frac{300}{T}\right)^{3/2}, \tag{31}$$

where

$$\Delta\nu_{0.093} = S_{0.093}\left(\frac{P}{1013.25}\right)\left(\frac{T}{300}\right)^{-n_{0.093}} \left(1 + \alpha_{0.093}\frac{\rho_{H_2O}T}{P}\right) \tag{32}$$

$$\Delta\nu^w_{wv} = C_4 k^w_{wv}\rho_{H_2O}\left(\frac{T}{300}\right)^{-n_{0.093}} \left(1 + \alpha_{0.093}\frac{\rho_{H_2O}T}{P}\right) \tag{33}$$

$$\Delta\nu^w_N = C_5 k^w_N P\left(\frac{T}{300}\right)^{0.62}, \tag{34}$$

in which w stands for the line wings; N for nitrogen, and wv for water vapor. $\Delta\nu^w_N$ is corrected for oxygen by reducing th' fective linewidth by a factor 1/2.11 for the fraction of oxygen molecules.[25a]

The temperature dependencies of $\Delta\nu^w_{wv}$ and $\Delta\nu^w_N$ have been established as follows: $\Delta\nu^w_{wv}$ is proportional to the partial pressure of water vapor which, in turn, is proportional to $\rho_{H_2O}T$. Benedict and Kaplan[25b] have established, however, that the line intensity weighted average for the .emperature exponent is -0.9, that is, the temperature dependence of the rotational band is proportional to $T^{-0.9}$ and, therefore, the $T^{0.1}$ dependence of $\Delta\nu^w_{wv}$.

For the nitrogen derived linewidth, $\Delta\nu^w_N$, the $T^{-0.62}$ temperature dependence is that derived for the line intensity weighted average for all of the nitrogen broadened water-vapor linewidths computed by Benedict and Kaplan.[26]

Table 4 presents the values for the molecular parameters of Eqs. 31-34 which are necessary to compute $(\gamma_{NON})_{0.164}$. When cgs units are used for general constants and ν is given in Hz, N in particles/cm^3, pressure P in mb, temperature T in °K, and water-vapor density ρ_{H_2O} in g/cm^3, then the values in Table 4 apply. The units of linewidths which result are in Hz and those of $(\gamma_{NON})_{0.164}$ are in nepers/cm.

Table 4. Molecular parameters needed to compute $(\gamma_{NON})_{0.164}$.

Parameter	Value	Theoretical or Measured	Source
μ_{H_2O}	1.87×10^{-18} e.s.u.	M	18
g_e	1	τ odd	
$\Sigma\|\Phi_{0.093}\|^2$	0.0891	T	6
$E(4_0)/C$	315.70 cm^{-1}	M	27
$\nu_{0.093}$	$323,758 \times 10^9$ Hz	T	27
$S_{0.093}$	2.79×10^9 Hz/atm	T	20
$n_{0.093}$	0.619	T	20
$a_{0.093}$	2.10×10^{-2} mb(g/m^3)$^{-1}$ ($^\circ$K)$^{-1}$	T	28
C_3	2.55×10^9	M	17
C_4	1.04		
C_5	0.66		
k_{wv}^w	200×10^6 Hz/mm Hg	M	17
k_N^w	$19. \times 10^6$ Hz/mm Hg	M	17

When the constants of Eqs. 26 and 31 are evaluated and more familiar parameters are substituted, the final operational equations for the 183-GHz line are the following:

$$\gamma_{0.164} = (\gamma_{RES})_{0.164} + (\gamma_{NON})_{0.164} = 978 \frac{\rho_{H_2O} {\nu'}^2}{T^{5/2}} e^{-197.3/T}$$

$$\left\{ \frac{\Delta\nu'_{0.164}}{(\nu'_{0.164}-\nu')^2 + {\Delta\nu'}^2_{0.164}} + \frac{\Delta\nu'_{0.164}}{(\nu'_{0.164}+\nu')^2 + {\Delta\nu'}^2_{0.164}} \right\}$$

$$+ 849 \frac{\rho_{H_2O} {\nu'}^2}{T^{5/2}} e^{-454/T} \left\{ \frac{\Delta\nu'_{0.093}}{(\nu'_{0.093}-\nu')^2 + {\Delta\nu'}^2_{0.093}} + \frac{\Delta\nu'_{0.093}}{(\nu'_{0.093}-\nu')^2 + {\Delta\nu'}^2_{0.093}} \right\}$$

$$+ 2.55 \frac{{\nu'}^2}{{\nu'}^3_{0.164}} \left(\Delta\nu'^{W}_{wv} + \Delta\nu'^{W}_{N} \right) \left(\frac{300}{T} \right)^{3/2} \quad dB/km. \tag{35}$$

The temperature dependence of the last term of (35) is that expected in the wings of water-vapor spectral lines (see Van Vleck[28]). All frequencies and linewidths are in
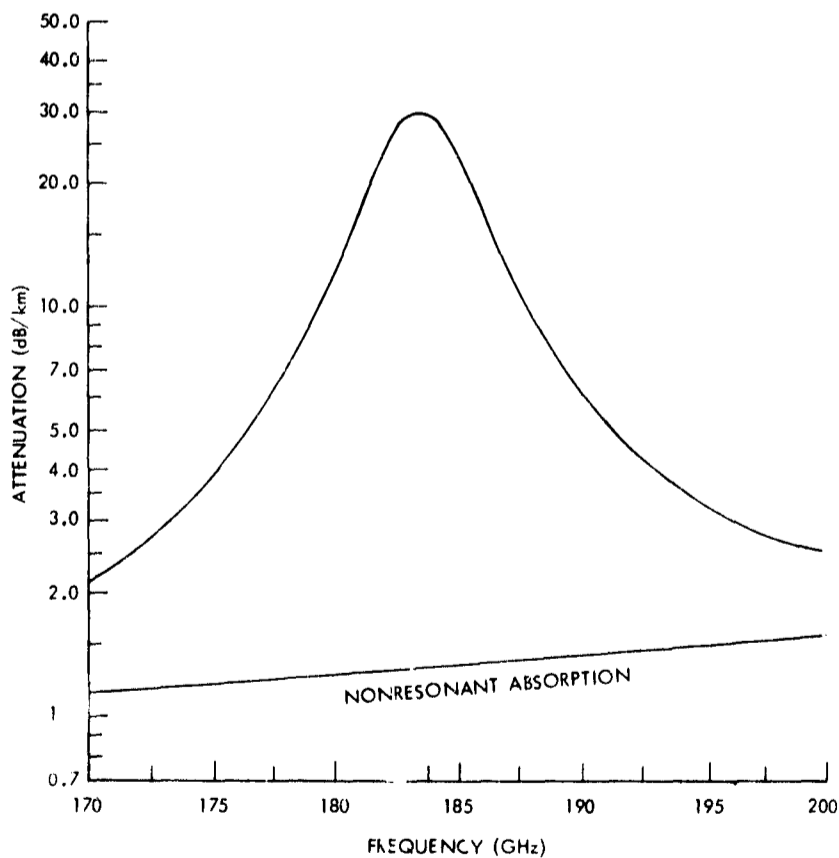

Fig. 6. 183-GHz rotational resonance of water vapor as represented by Eq. 35. Conditions in the gas: 1000 mb dry air; 7.23 g/m³ water vapor (7.5 mm Hg); temperature 300°K.

GHz (denoted by primes) instead of Hz, thereby requiring $S_{0.093}$, $v_{0.093}$, C_3, k^W_{wv}, and k^W_N when used in Eqs. 32-34 to be reduced by a factor of 10^9.

Further simplification of (35) may be accomplished without substantial loss of accuracy, if one confines his observations to a frequency region near to the 183-GHz resonance. The major contribution to $(\gamma_{NON})_{0.164}$ within 50 GHz of 183 GHz is over-whelmingly due to the third term of Eq. 35, the contributions of lines other than the 324-GHz and 183-GHz lines. The ratio of the last to the middle term in Eq. 35 over this region is approximately 200:1. Only as one approaches 300 GHz does the second term begin to contribute a substantial percentage to the absorption. Below 183 GHz, the only contribution at all is the 22-GHz line, which does not make its contribution felt until well below 100 GHz.

Figure 6 illustrates water-vapor broadened by air in the frequency interval 170-200 GHz, with Eq. 35 used.

Although water-vapor absorption will dominate over oxygen in the regions near 22 GHz and 183 GHz, oxygen absorption must be taken into account for the measurements and numerical experiments near the lower frequency line. (It is less than the error expected in Eq. 35 near 183 GHz.) The computational equations for oxygen absorption are presented in Appendix B.

III. RADIATIVE TRANSFER IN THE EARTH'S ATMOSPHERE

The equation of radiative transfer for the atmosphere of the earth is presented now for the special conditions of an absorbing, nonscattering atmosphere in local thermodynamic equilibrium. The question of the existence of local thermodynamic equilibrium in the Earth's atmosphere is also discussed; weighting functions for radiation attenuated or emitted by water vapor in the atmosphere around the two resonant frequencies of interest are derived for several geometries and illustrated by numerical examples; and the quasi-stationary character of the weighting functions over various climatological conditions is investigated.

3.1 FUNDAMENTAL DEFINITIONS

The fundamental equation of radiative transfer for an atmosphere whose index of refraction is unity is given by

$$\frac{dI_\nu}{d\ell} = -\gamma_\nu I_\nu + \eta_\nu, \tag{36}$$

in which I_ν represents the specific intensity at the point of interest in the medium, γ_ν the absorption coefficient, η_ν the volume emissivity, and $d\ell$ an increment of length along the path of the radiation. (For a derivation of Eq. 36 without the assumption of an unchanging index of refraction, see Woolley and Stibbs.[29])

Equation 36 is usually written in a form that takes account of the concept of optical depth, sometimes called optical thickness, or opacity which is defined by

$$\tau_\nu = \int_0^{\tau_\nu} d\tau_\nu = \int_0^\ell - \gamma_\nu \, d\ell = + \int_\ell^0 \gamma_\nu \, d\ell, \tag{37}$$

where $d\ell$ is positive in the direction of energy flow, and $d\tau_\nu$ is positive in the opposite direction. Equation 36 transforms to

$$\frac{dI_\nu}{d\tau} - I_\nu = - \frac{\eta_\nu}{\gamma_\nu} \tag{38}$$

which readily integrates to

$$\left(I_\nu \, e^{-\tau_\nu} \right)_0^{\tau_{max}} = - \int_0^{\tau_{max}} \frac{\eta_\nu}{\gamma_\nu} e^{-\tau_\nu} \, d\tau_\nu \tag{39}$$

in which

$$\tau_{max} = \int_0^{\ell_{max}} - \gamma_\nu \, d\ell. \tag{40}$$

21

To apply (39) to the atmosphere of the Earth, consider the geometry of the horizontally stratified, plane parallel atmosphere depicted in Fig. 7. An antenna on the ground with main beam half-power points ϕ_m degrees apart views an extraterrestrial source
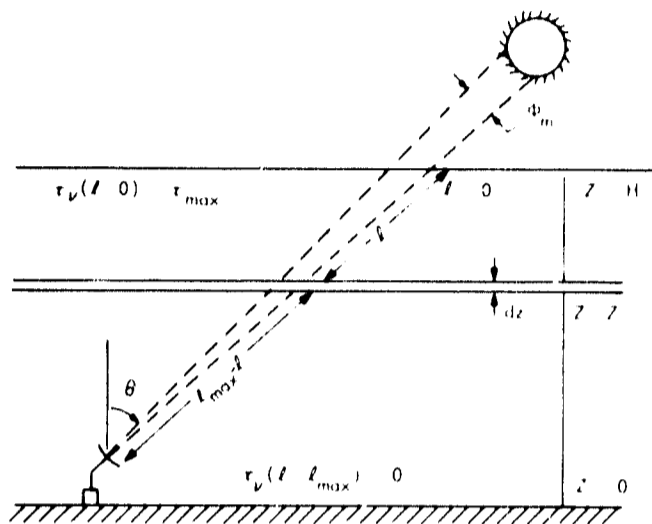

Fig. 7. Geometry for microwave observations in a planar, horizontally stratified atmosphere.

through the atmosphere at an angle of θ degrees away from the zenith. The extraterrestrial source fills the main beam. Because of horizontal stratification and the planar geometry, it is most convenient to redefine τ_ν in terms of z and θ as

$$\tau_\nu(z, \theta) = \int_{\ell=\ell_{max}}^{\ell} \gamma_\nu \, d\ell = \int_0^z \gamma_\nu \sec \theta \, dz. \tag{41}$$

More simply, for zenith angles other than zero, the opacity from z = 0 to z = z is given by $\tau_\nu(z, 0) \sec \theta$. Equation 39 may now be rewritten for the geometry of Fig. 7 and the definition from Eq. 41 as

$$I_\nu(O) = I_\nu(H) \, e^{-\tau_{max} \sec \theta} + \int_0^H \frac{\eta_\nu}{\gamma_\nu} e^{-\tau_\nu(z, 0) \sec \theta} \gamma_\nu \sec \theta \, dz \tag{42}$$

where now

$$\tau_{max} = \int_0^H \gamma_\nu \, dz. \tag{43}$$

The intensity reaching the antenna at z = 0 is $I_\nu(O)$. It is composed of two components, the first of which is the intensity at z = H, a level above all significant attenuating gases, diminished by its passage through the atmosphere $\left(e^{-\tau_{max} \sec \theta} \right)$. The second component originates in the atmosphere and is represented by the integral on the right-hand side of (42). The atmospheric contribution to $I_\nu(O)$ represents the

radiation from thin slabs of atmosphere of effective thickness dz sec θ. The strength of the radiation received at the antenna from any slab is equal to the volume emissivity of that slab times the effective volume of a unit cylinder along the propagation path diminished by the absorption of all of the intervening layers. The absorption factor is represented by $e^{-\tau_\nu(z,0)\sec\theta}$, where $\tau_\nu(z,0) = \int_0^z \gamma_\nu\, dz$.

Rather than simply cancelling the γ_ν that appear in the integral of (42) and deal with the volume emissivity, it is more convenient to define a new quantity

$$J_\nu = \frac{\eta_\nu}{\gamma_\nu} \tag{44}$$

called the <u>source</u> <u>function</u>. From Kirchhoff's law for an atmosphere in local thermodynamic equilibrium it can be shown that

$$J_\nu = I_\nu \tag{45}$$

and Eq. 44 can be written

$$I_\nu(O) = I_\nu(H)\, e^{-\tau_{max}\sec\theta} + \int_0^H I_\nu \gamma_\nu\, e^{-\tau_\nu \sec\theta} \sec\theta\, dz, \tag{46}$$

This is the fundamental equation of transfer for radiation in a planar, horizontally stratified, nonscattering atmosphere in local thermodynamic equilibrium.

For microwave radiation, the Rayleigh-Jeans approximation may be used and Eq. 46 can be finally written

$$T_B(O) = T_B(H)\, e^{-\tau_{max}\sec\theta} + \int_0^H T_{AT}\gamma_\nu\, e^{-\tau_\nu \sec\theta} \sec\theta\, dz, \tag{47}$$

where T_B represents an equivalent black-body temperature which, in the frequency interval of interest, produces an intensity I_ν.

3.2 THERMODYNAMIC EQUILIBRIUM IN THE ATMOSPHERE

In the light of Eq. 47, it is necessary to evaluate the assumption that the atmosphere is in thermodynamic equilibrium, and, for that matter, what thermodynamic equilibrium means in terms of rotational spectra.

Thermodynamic equilibrium, in general, refers to a state for an assemblage of particles in which the total energy of the assemblage is distributed over the particles in the most probable statistical manner; that is, a state identified by the maximum value of the entropy that is possible for the conditions of the gas (see Planck[30]). When thermodynamic equilibrium exists the distribution of energy is given by Boltzmann's equation

$$\frac{N_i}{N} = \frac{g_i e^{-E_i/kT}}{\sum_j g_j e^{-E_j/kT}}, \tag{48}$$

in which N_i is the number of particles of energy E_i, N is the total number of particles, g_i is the statistical weight of the energy level E_i, k is Boltzmann's constant, and T is temperature. For discrete energy levels that exist for rotation, vibration, and electronic excitation, the summation is appropriate in the denominator. In the limit of a continuous energy distribution as for energy of translation, the summation should be replaced by an integral. The denominator of the right-hand side is called the partition function for the energy mode it describes. A similar expression was evaluated in Section II for the distribution of energy over rotational states in an assemblage of water molecules.

For molecules, several semi-independent domains of energy exist: kinetic energy of translation, rotational energy, vibrational energy, and electronic excitation energy. The last three energy modes are quantized and can interact with the radiation field. Energy can be redistributed between the modes when collisions occur. It is possible for the various energy modes to separately approach thermodynamic equilibrium. Goody[31] has analyzed the conditions in the atmosphere which allow the translational, vibrational, and rotational energy distributions to maintain thermodynamic equilibrium against naturally occurring perturbations. He has concluded that thermodynamic equilibrium exists for translational motion up to the region where collisions are no longer likely. This is in the highest regions of the ionosphere, hundreds of kilometers above the region where water vapor is important.

Vibrational energy is also maintained in thermodynamic equilibrium by collisions and, from Goody's estimate, equilibrium exists at least up to 74 km.

Rotational energy is more easily distributed by collisions than vibrational energy. Natural lifetimes for rotational-energy levels of water vapor are of the order of 0.1 sec to, perhaps, 10 sec, values that may be computed from the dipole matrix elements. The relaxation time for collisional redistribution of energy is proportional to $1/P$, and at standard temperature and pressure has a value approximately equal to 10^{-10} sec. This estimate is based upon Anderson's theory,[10] in which the relaxation time is shown to be related to the linewidth. From these estimates Goody concludes that rotational-energy levels should be distributed according to Boltzmann's law at least down to pressures of 10^{-6} mb, a height of approximately 150 km in the Standard Atmosphere. From other considerations, notably the fact that photodissociation of water-vapor molecules probably becomes important at less than half of this altitude, it is reasonable to expect that wherever water vapor occurs it will be in rotational thermodynamic equilibrium.

The rotational temperature and kinetic temperature defined by separate statements of Eq. 48 will, under all natural conditions, be the same, since the energy of the system

will be equally available to translational as well as rotational degrees of freedom at the pressures and temperatures found in the atmospheric regions where water-vapor absorption will be important.

Finally, a remark should be made about electronic transitions for water vapor. At the ground, the ratio of the lifetime for collision-induced transitions to the lifetime of spontaneous transitions is very large; thermodynamic equilibrium cannot exist. But the energy required to cause electrons to transition to excited states is so great that this is a rare and unimportant process in any equation of transfer for the atmosphere at any frequency below the visible.

3.3 MICROWAVE MEASUREMENTS AND ATMOSPHERIC WATER-VAPOR WEIGHTING FUNCTIONS NEAR THE 22.2-GHz RESONANCE

Measurements can be made at microwave frequencies which contain information about the water vapor in the beam of the receiving antenna. In effect, various measurements are made to simplify Eq. 47 or to take advantage of some special geometry, such as that afforded by a satellite.

3.3.1 Total Zenith Opacity near 22.2 GHz

One of the microwave properties of the atmosphere is its total (zenith) opacity τ_{max}. It is defined as

$$\tau_{max} = \tau_\nu(H, O) = \int_0^H \gamma_\nu \, dz, \tag{49}$$

where γ_ν is the total absorption from all constituents of the gas at frequency ν. In the atmosphere of the Earth, on clear days, only oxygen and water vapor contribute non-negligible absorption to τ_{max} over the microwave range. Therefore, since $\gamma_\nu = \gamma_{H_2O} + \gamma_{O_2}$, then τ_{max} can be written

$$\tau_{max} = (\tau_{max})_{H_2O} + (\tau_{max})_{O_2} = \int_0^H \gamma_{H_2O} \, dz + \int_0^H \gamma_{O_2} \, dz. \tag{50}$$

If the two contributions to τ_{max} can be separated, then the zenith opacity of atmospheric water vapor may be studied as a function of frequency. γ_{H_2O} and γ_{O_2} are those absorption coefficients derived in Section II and presented in Appendix B. Recall that γ_{H_2O} for the 1.35-cm line is composed of $(\gamma_{RES})_{1.35}$ and $(\gamma_{NON})_{1.35}$ and can be written

$$\gamma_{H_2O} = 1.57^V \times 10^3 \left\{ \frac{\rho_{H_2O} \nu'^2 e^{-642/T}}{T^{5/2}} \right\} \left\{ \frac{\Delta\nu'_{1.35}}{(\nu'_{1.35} - \nu')^2 + \Delta\nu'^2_{1.35}} + \frac{\Delta\nu'_{1.35}}{(\nu'_{1.35} + \nu)^2 + \Delta\nu'^2_{1.35}} \right\}$$

$$+ 1.11 * 10^{-2} \left\{ \frac{\rho_{H_2O} \nu'^2 \Delta\nu'}{T^{3/2}} \right\} \text{ dB/km}$$

$$= \rho_{H_2O} \left\{ g(\nu, P, T, \rho_{H_2O}) \right\}, \tag{51}$$

where the dependence of g on ρ_{H_2O} is quite small. It is clear that the same water-vapor density will show different values for absorption at different levels in the atmosphere. If we know the structure of the atmosphere, then we can compute a weighting function for water-vapor contributions to $(\tau_{max})_{H_2O}$. By definition, therefore,

$$W_\tau(\nu, z) = \frac{\gamma_{H_2O}(\nu, z)}{\rho(z)}, \tag{52}$$

so that

$$[\tau_{max}(\nu)]_{H_2O} \cong \int_0^H W_\tau(\nu, z) \, \rho(z) \, dz. \tag{53}$$

The dependence of the weighting function $W_\tau(\nu, z)$ on P, T, and ρ is shown implicitly through z.

The formulation of a weighting function is important because it shows at what height in a particular atmosphere the attenuation for a given amount of water vapor is greatest, that is, where it is most "sensitive" to water vapor. This sensitivity is a function of frequency.

For the 22.2-GHz water-vapor line, Fig. 8 presents 3 weighting functions computed from Eq. 52 and normalized to unity in each case. They represent typical shapes for weighting functions which one can expect for spectral measurements around this particular resonance. The wings of the line (represented by the 19.00-GHz curve) show an exponential-like decrease with altitude. At resonance (22.237 GHz), the weighting function increases roughly exponentially with height. For frequencies near resonance, there is a maximum sensitivity at some intermediate altitude.

The height of the maximum decreases for frequencies farther from resonance. The frequency dependence of this maximum height is shown in Fig. 9. The width at half-strength of those weighting functions with maxima at intermediate levels is approximately 18 km.

The characteristic shapes of the three representative weighting functions arise from
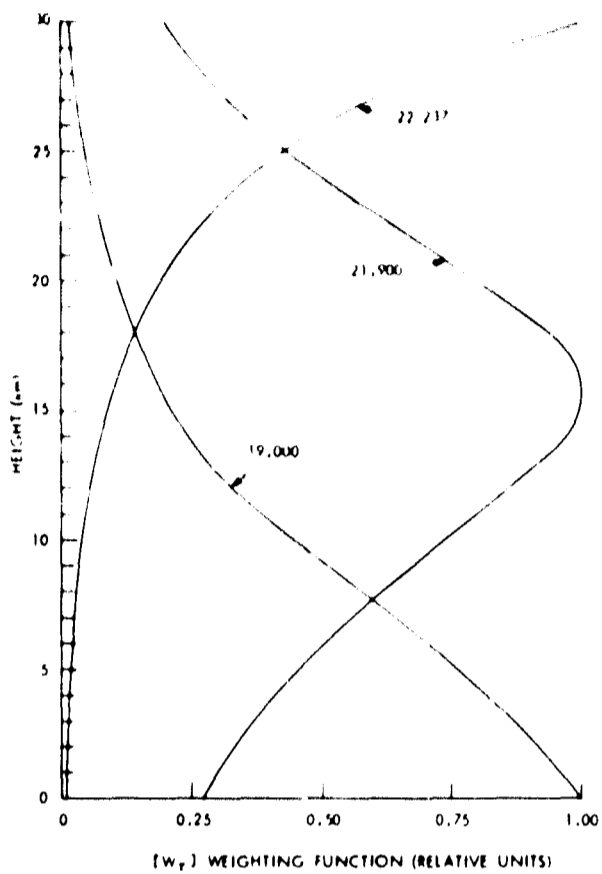
Fig. 8. Normalized zenith opacity weighting functions for atmospheric water vapor.
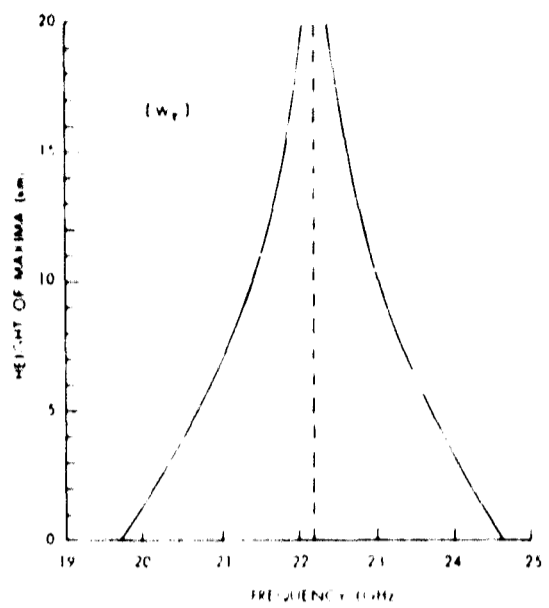

Fig. 9. Frequency dependence of the height of the zenith opacity weighting-function maxima.
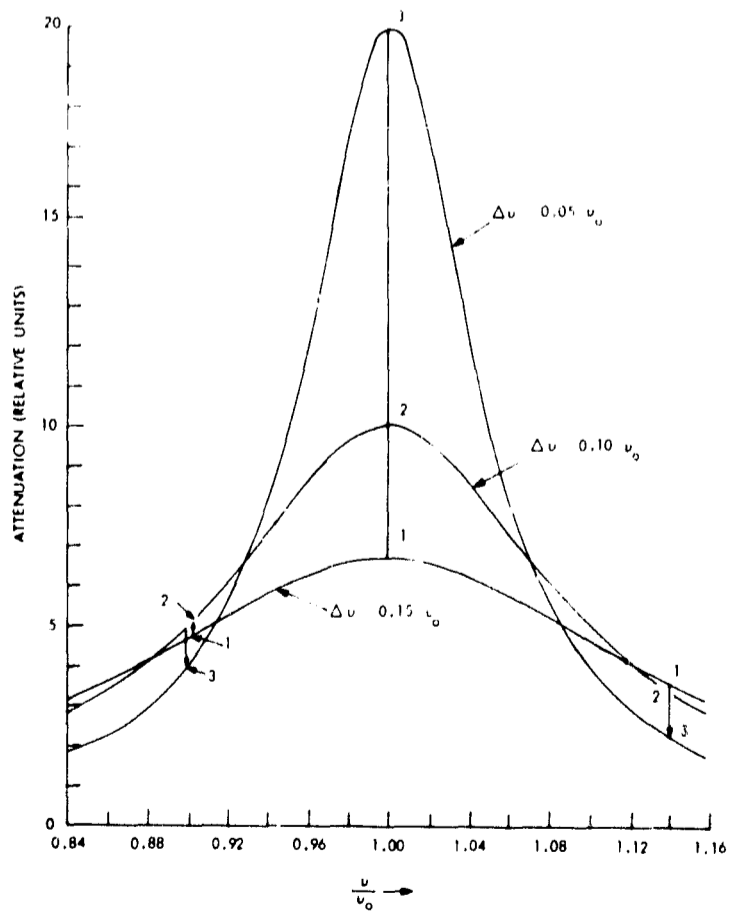

Fig. 10. Origin of atmospheric water-vapor weighting functions.

the effect of decreasing pressure in the linewidth parameter and the effective role of this parameter near and far from resonance. If we examine the line-shape factor of Eq. 13, we find that at resonance the $(v_{ij}-v)^2$ term in one of the denominators is zero and the whole factor is closely proportional to $1/\Delta v$ and thus to $1/P$. Far away from resonance, the $(v_{ij}-v)^2$ term dominates over the Δv^2 term in the denominator, and the line-shape factor is more nearly proportional to Δv and therefore to P. In between, the situation is best illustrated by Fig. 10. In Fig. 10, at 3 frequencies, sequences of numbers are provided to direct the reader's attention to the effects of decreasing pressure, and thus to decreasing linewidth and increasing altitude in the atmosphere. (1) is associated with the highest pressure and widest linewidth. (2) is an intermediate pressure level. (3) is the lowest pressure and narrowest linewidth. At resonance $(v/v_o = 1.0)$ and far enough into the wings $(v/v_o = 1.14)$, the attenuation acts monotonically, as discussed previously. For intermediate frequencies (represented in Fig. 10 by $v/v_o = 0.90$) the attenuation at first increases, then falls monotonically as the line progressively narrows. This causes a maximum attenuation to occur at some pressure, and therefore some height.

To investigate the constancy of zenith opacity weighting functions, Fig. 11 was prepared. Weighting functions at 19.00 GHz were computed for 4 diverse climatological regions: Tropics (15°N); Midlatitude (40°N); Subarctic summer (60°N); and Arctic (75°N). The atmospheres used for the comparisons were the Standard Atmosphere 1962, and the Supplemental Atmosphere thereto, all taken from Valley.[37]

The extreme cold of the Arctic atmosphere plays a dominant role in elevating the surface attenuation in this region. In other than Arctic regions, differences of perhaps 5% occur between weighting-function curves. At frequencies near resonance, the differences between the Arctic and other atmospheres at the surface, for the most part, disappear, as may be seen in Fig. 12; farther from resonance, the differences at the surface increase. The midlatitude curve in Fig. 12 has not been plotted because at all altitudes it falls within the other curves. For the summertime at least, and from the surface to perhaps 10 km, the zenith opacity weighting functions vary little over approximately 80% of the Earth's surface.

As a final investigation of the gross features that one might expect for microwave measurements of total zenith opacity, Fig. 13 is presented. The Tropical, Midlatitude, and Arctic opacities are plotted as a function of frequency. These curves represent water vapor only; oxygen attenuation is not included. This gives some feeling for the range of amplitude which world-wide water-vapor opacity measurements might show. The variation of the line amplitude shown in Fig. 13 can also be obtained on a seasonal basis in midlatitude continental regions, as will be seen in Section IV.

3.3.2 Surface Observations of Atmospheric Brightness Temperature near 22 GHz

Another microwave spectral observation of the atmosphere that we might wish to make is the emission as a function of frequency. Since the emission from space is
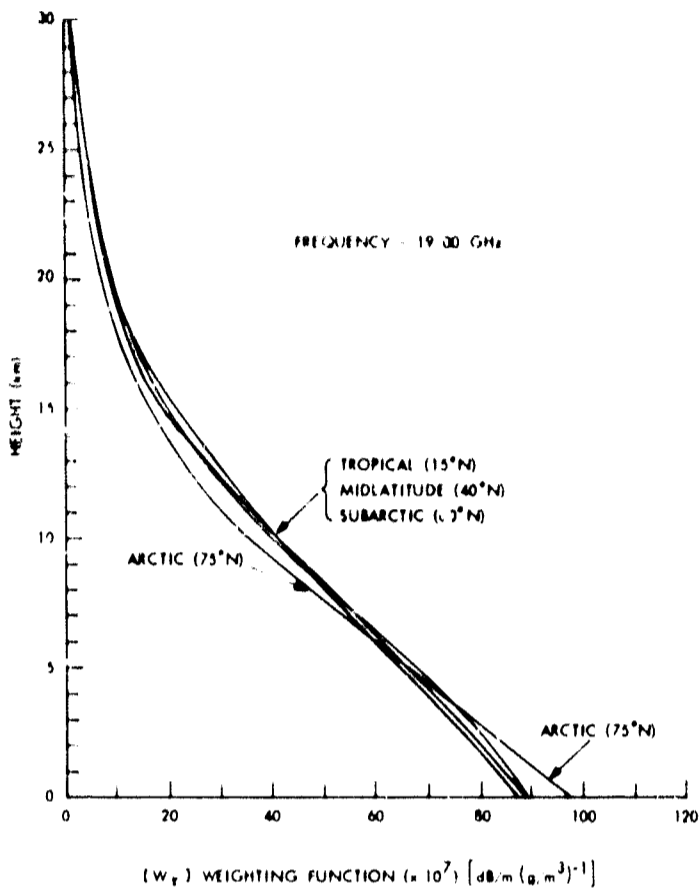
Fig. 11. Stability of the 19-GHz zenith
opacity weighting function for
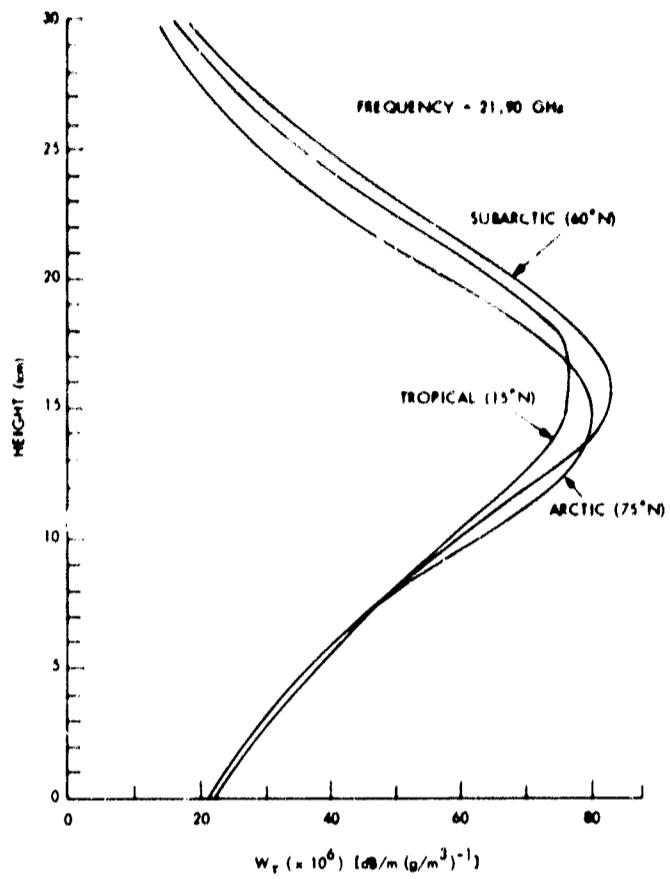differing climatic regions.

Fig. 12. Stability of the 21.9-GHz zenith
opacity weighting function for
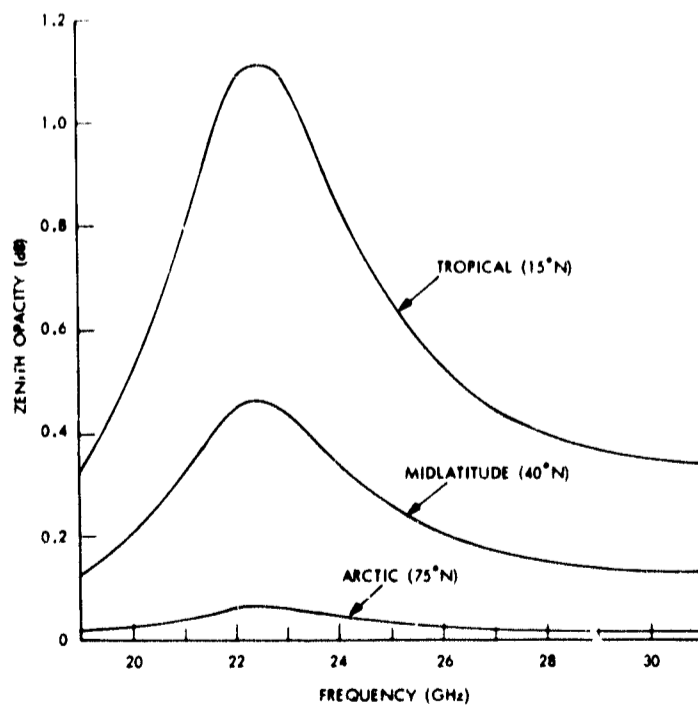differing climatic regions.

Fig. 13. Absorption spectra computed for mean conditions
in several climatic regions.

small and approximately steady, unless one's antenna is viewing the sun or the moon, or some strong radio source with a very narrow beam, the first term on the right-hand side of (47) can be neglected. We have left

$$T_B(\nu) = \int_0^H T_{AT} \, \gamma_\nu \, e^{-\tau_\nu(z, 0) \sec \theta} \sec \theta \, dz. \tag{54}$$

The water-vapor weighting functions that would be appropriate for such a measurement can be defined as

$$[W_T]_{up} = \frac{T_{AT}(z) \, \gamma_{H_2O}(z) \, e^{-\tau_\nu(z, 0) \sec \theta} \sec}{\rho(z)} \tag{55}$$

Equation 55 is a considerably more complicated function than the weighting function for $[\tau_{max}]_{H_2O}$ alone. Despite the complexity and nonlinearity of (55), it is still a useful concept, as may be judged from Fig. 14.
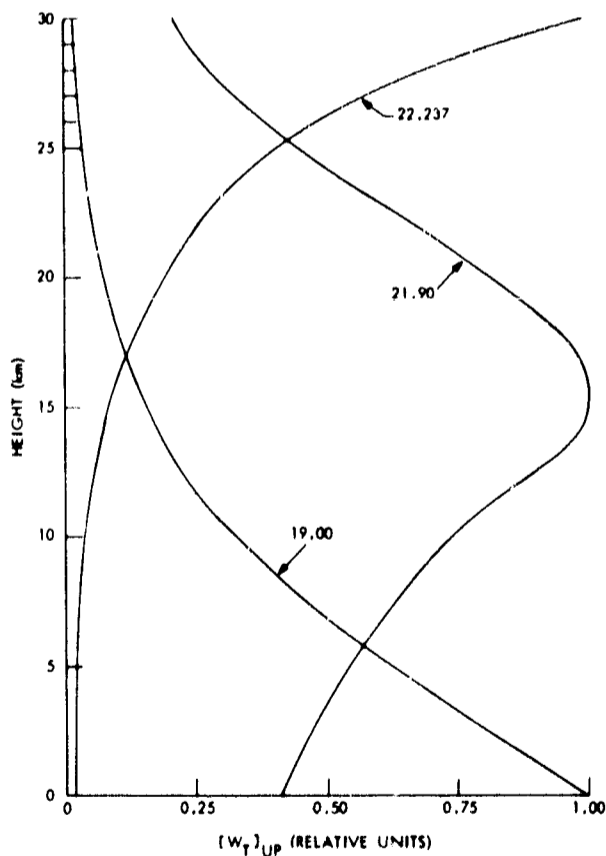
Fig. 14.

Normalized zenith emission weighting functions for atmospheric water vapor.

Weighting functions for the same three frequencies that were analyzed for the zenith opacity weighting functions are presented in Fig. 14. Their shapes are very similar to the opacity shapes. It is apparent that the attenuation factor still dominates the functions; the percentage temperature changes are so small and the exponential factor is so unimportant that together they introduce only the changes in shape seen from
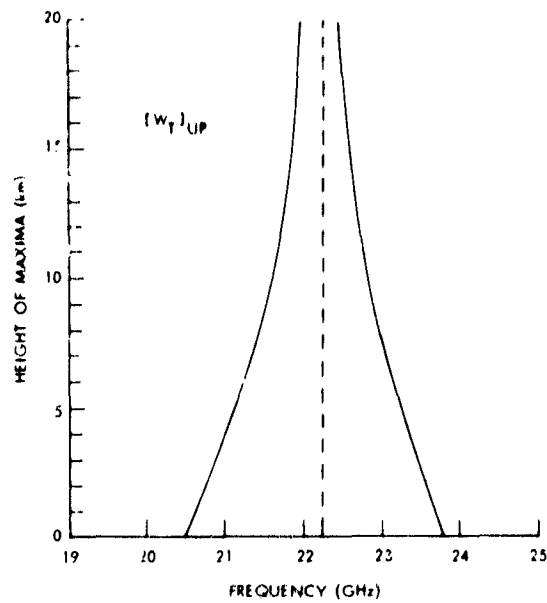
Fig. 15. Frequency dependence of the height at which maxima occur for zenith emission weighting functions.
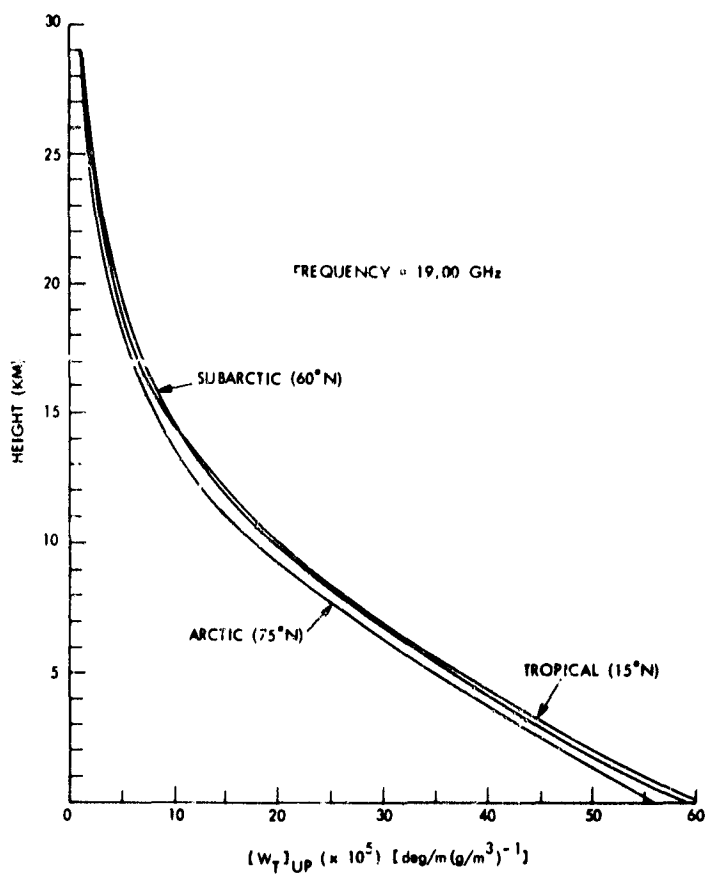
Fig. 16. Climatic variations in the 19-GHz zenith emission weighting function.

Fig. 17. Climatic variations in the 21.9-GHz zenith emission weighting function.

Fig. 18. Zenith emission spectra for mean
conditions in several climatic
regions.

Figs. 8 and 14. The reason that the amplitude of the function between the surface value and the maximum is less than for the opacity is a result of the temperature decrease between these two levels.

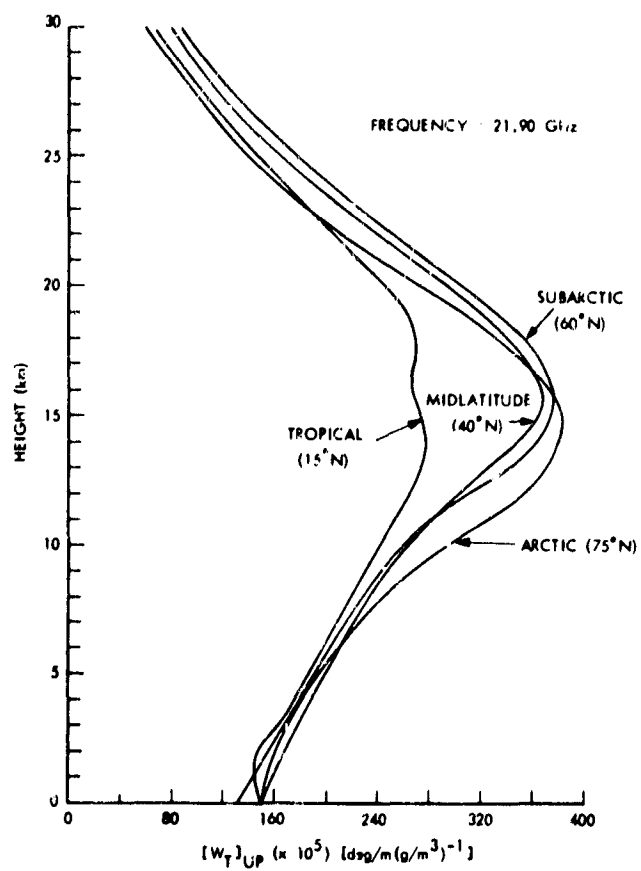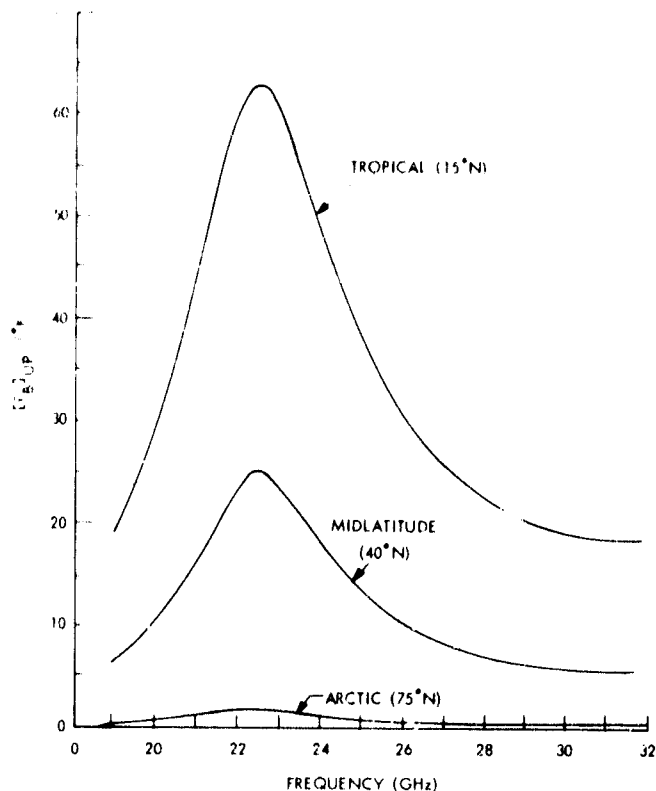The height at which a maximum occurs for a given frequency is plotted in Fig. 15. The curves are considerably narrower than the opacity-maxima curves, again indicating an alteration that is due to changes introduced largely by the temperature profile.

The variation of the weighting functions over world-wide climates may be seen in Figs. 16 and 17. The midlatitude curve is not plotted in Fig. 16 because it fell very close to the tropical and subarctic plots everywhere. The stability of the function at 19.0 GHz, at least away from the Arctic, is greater than the analogous opacity weighting function.

The variation with climate of the 21.9-GHz upward looking brightness temperature weighting function is considerably greater everywhere than its opacity counterpart. The climatic temperature variations show up strongly near the surface. Especially noticeable is the decrease of the tropical weighting function near the surface, because of the prevailing temperature and moisture inversion. But the great divergence of tropopause heights and temperatures causes the largest discrepancies between the weighting functions to appear in the vicinity of the sensitivity maximum. The extreme cold of the tropical tropopause, which occurs at roughly 16 km, even causes a minor minimum to appear in that climatic region's weighting function.

As a last set of characteristic curves for the brightness temperature spectrum that might be measured from the ground, Fig. 18 is presented. It conveys the amplitude variation that might be expected over the world's climates. These curves are means and therefore at each latitude a great deal of variation from the mean curves can be expected.

3.3.3 Observations of the Atmosphere from Space near 22 GHz

If the natural advantages of the satellite-borne radiometer are to be exploited, observations from above the atmosphere must prove to be feasible. For observations from space, we find that the full equation of radiative transfer must be used. Equation 47 must be modified to read

$$T_B(H) = T_B(O) \, e^{-\tau_{max} \sec \theta} + \int_0^H T_{AT} \, \gamma_\nu \, e^{-\int_z^H \gamma_\nu \sec \theta \, dz'} \sec \theta \, dz, \qquad (56)$$

in which the attenuation factor for the atmospheric contribution must be computed from the source level upward to the satellite height H, rather than downward as in Eq. 47; and rather than an extraterrestrial source of radiation attenuated by the full atmosphere, an effective brightness temperature for the Earth's surface must be supplied. $T_B(O)$ is not easy to evaluate. It may be expanded, however, as follows:

$$T_B(O) = (1-R) \, T_g + R \int_0^H T_{AT} \, \gamma_\nu \, e^{-\int_0^z \gamma_\nu \sec \theta \, dz'} \sec \theta \, dz, \qquad (57)$$

where the first term on the right-hand side of (57) represents the temperature of the Earth, T_g, diminished by its emissivity equal to $(1-R)$, where R is the power reflection coefficient at the frequency of interest. The second term is the radiation from the atmosphere reflected by the Earth's surface.

A weighting function may be derived for satellite observations. Rewrite (56), using (57).

$$T_B(H) = \int_0^H T_{AT}\left(\gamma_{H_2O} + \gamma_{O_2}\right) e^{-\int \gamma_\nu \sec \theta \, dz'} \sec \theta \, dz$$

$$+ \left\{ R \int_0^H T_{AT}\left(\gamma_{H_2O} + \gamma_{O_2}\right) e^{-\int_0^z \gamma_z \sec \theta \, dz'} \sec \theta \, dz \right.$$
$$\qquad \qquad \qquad \qquad \qquad \qquad \qquad \qquad \qquad (58)$$

$$\left. + (1-R) \, T_g \right\} e^{-\tau_{max} \sec \theta}$$

Recall that $\gamma_\nu = \gamma_{H_2O} + \gamma_{O_2}$, and separate the oxygen and water-vapor terms.

$$T_B(H) = T'_{H_2O} + T'_{O_2} + (1-R) \, T_g \, e^{-\tau_{max} \sec \theta}, \qquad (59)$$

where

$$T'_{H_2O} = \int_0^H T_{AT} \, \gamma_{H_2O} \, e^{-\int_z^H \gamma_\nu \sec \theta \, dz'} \sec \theta \, dz$$

$$+ R \int_0^H T_{AT} \, \gamma_{H_2O} \, e^{\left(-2\tau_{max} \sec \theta + \int_z^H \gamma_\nu \sec \theta \, dz'\right)} \sec \theta \, dz \qquad (60)$$

and

$$T'_{O_2} = \int_0^H T_{AT} \, \gamma_{O_2} \, e^{-\int_z^H \gamma_\nu \sec\theta \, dz} \sec\theta \, dz$$

$$+ R \int_0^H T_{AT} \, \gamma_{O_2} \, e^{(-2\tau_{max} \sec\theta + \int_z^H \gamma_\nu \sec\theta \, dz')} \sec\theta \, dz. \tag{61}$$

Regrouping (60) and (61) leads to

$$T'_{H_2O} = \int_0^H T_{AT} \, \gamma_{H_2O} \left[e^{-\int_z^H \gamma_\nu \sec\theta \, dz} + R \, e^{-2\tau_{max} \sec\theta + \int_z^H \gamma_\nu \sec\theta \, dz'} \right] \sec\theta \, dz \tag{62}$$

and

$$T'_{O_2} = \int_0^H T_{AT} \, \gamma_{O_2} \left[e^{-\int_z^H \gamma_\nu \sec\theta \, dz} + R \, e^{-(\tau_{max} \sec\theta - \int \gamma_\nu \sec\theta \, dz')} \right] \sec\theta \, dz. \tag{63}$$

The last term from Eq. 58, representing emission from the Earth, can be expanded, if $\tau_{max} \sec\theta$ is small, as

$$(1-R) \, T_g \, e^{-\tau_{max} \sec\theta} = (1-R) \, T_g \left\{ 1 - \tau_{max} \sec\theta + \dots \right\}. \tag{64}$$

For total attenuation of 1.5 dB, the error introduced into the bracketed term of (62) by neglecting the terms higher than first-order amount to approximately 9.4%; that is, the value of the bracketed term would be low by 9.4%. For total attenuation of 1 dB, the error drops to approximately 3.5%, and for 0.5 dB the error is 0.8%. The effect on $T_B(H)$, if one uses the approximation, is to flatten the peak of the brightness-temperature curve. In (64) τ_{max} may be separated into the water-vapor and oxygen components

$$\tau_{max} = (\tau_{max})_{H_2O} + (\tau_{max})_{O_2}, \tag{65}$$

and the new resultant terms may be redistributed with the water-vapor and oxygen components of (59). The oxygen component can be written in final form as

$$T_{O_2} = T'_{O_2} - (1-R) \, T_g \int_0^H \gamma_{O_2} \sec\theta \, dz$$

$$= \int_0^H T_{AT} \left\{ e^{(-\int_z^H \gamma_\nu \sec\theta \, dz')} + R \, e^{-(2\tau_{max} \sec\theta - \int_z^H \gamma_\nu \sec\theta \, dz)} - (1-R) \, T_g \right\} \gamma_{O_2} \sec\theta \, dz. \tag{66}$$

34

The water-vapor component in final form is

$$T_{H_2O} = T'_{H_2O} - (1-R)\, T_g \int_0^H \gamma_{H_2O}\, \sec\theta\, dz$$

$$= \int_0^H T_{AT} \left\{ e^{-\int_z^H \gamma_\nu \sec\theta\, dz} + R\, e^{-(2\tau_{max} \sec\theta - \int_z^H \gamma_\nu \sec\theta\, dz)} \right.$$

$$\left. - (1-R)\, T_g \right\} \gamma_{H_2O}\, \sec\theta\, dz. \tag{67}$$

The brightness temperature at the satellite is

$$T_B(H) = T_{H_2O} + T_{O_2} + (1-R)\, T_g + \epsilon(\tau_{max}), \tag{68}$$

where $\epsilon(\tau_{max})$ is a correction for the approximation made in Eq. 64. It should be pointed out that T_{H_2O} and T_{O_2} are not independent of γ_{O_2} and γ_{H_2O}, respectively, since both contain $\gamma_\nu = \gamma_{H_2O} + \gamma_{O_2}$ in exponentials.

A weighting function for atmospheric water vapor may now be easily extracted from Eq. 67. It is

$$[W_T]_{down} = T_{AT} \left\{ e^{-\int_z^H \gamma_\nu \sec\theta\, dz} + R\, e^{-(\tau_{max} \sec\theta - \int_z^H \gamma_\nu \sec\theta\, dz)} \right.$$

$$\left. - (1-R)\, T_g \right\} \frac{\gamma_{H_2O}}{\rho}\, \sec\theta, \tag{69}$$

evaluated at some height z in the atmosphere. The derivation of this weighting function is due to Staelin.[33] Equation 68 can be written, with the aid of (69) as

$$T_B(H) = \int_0^H [W_T]_{down}\, \rho(z)\, dz + T_{O_2} + (1-R)\, T_g + \epsilon(\tau_{max}). \tag{70}$$

More must be said about the quantity R, the power reflection coefficient of the Earth. In general, this is a very complicated function. For a surface that is smooth within approximately one-eighth of a wavelength, and is electrically homogeneous, it can be computed from Fresnel's equations. The results depend upon the complex dielectric constant for the material, the angle from which the surface is viewed, and the polarization of the antenna. Furthermore, buried in the complex dielectric constant are more dependencies: frequency, temperature, salinity for sea water, and the nature of the surface for solid materials (that is, compactness of the material, sizes of the grains making up the surface, and so forth).

Finally, the real surface of the Earth presents no smooth surfaces or large areas composed of electrically homogeneous materials. The closest approximation to electrical homogeneity is afforded by sea water which does not have the same saline content in all regions, but the difference is only slight. And, even though the surface of the sea is seldom smooth, the emissivity of sea water offers the best hope, at present, of yielding to analytical treatment.

For want of better information, we have assumed a reflectivity value and computed weighting functions according to Eq. 69. The same four diverse atmospheres that were used in examining the other weighting functions have been used in Fig. 19.
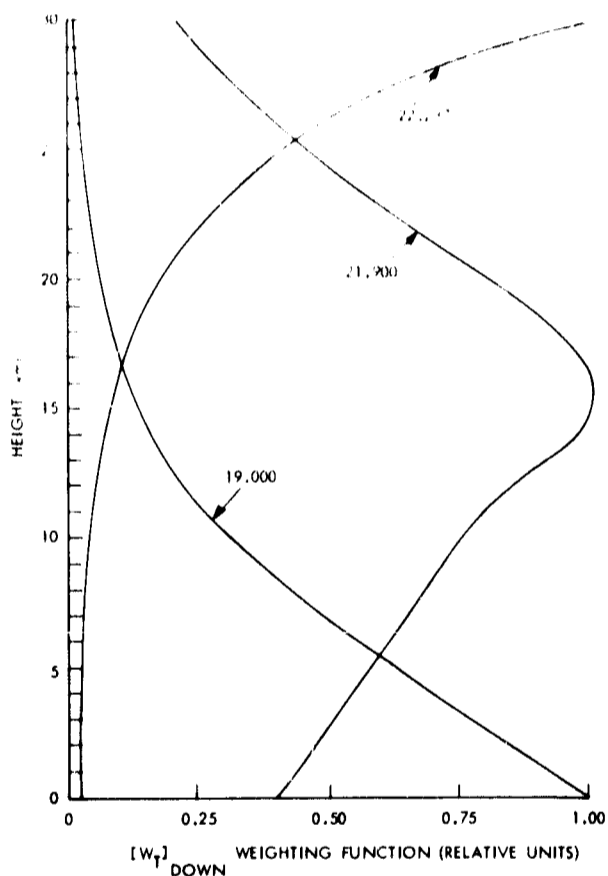
Fig. 19.

Normalized atmospheric water vapor emission weighting functions for observations from space.
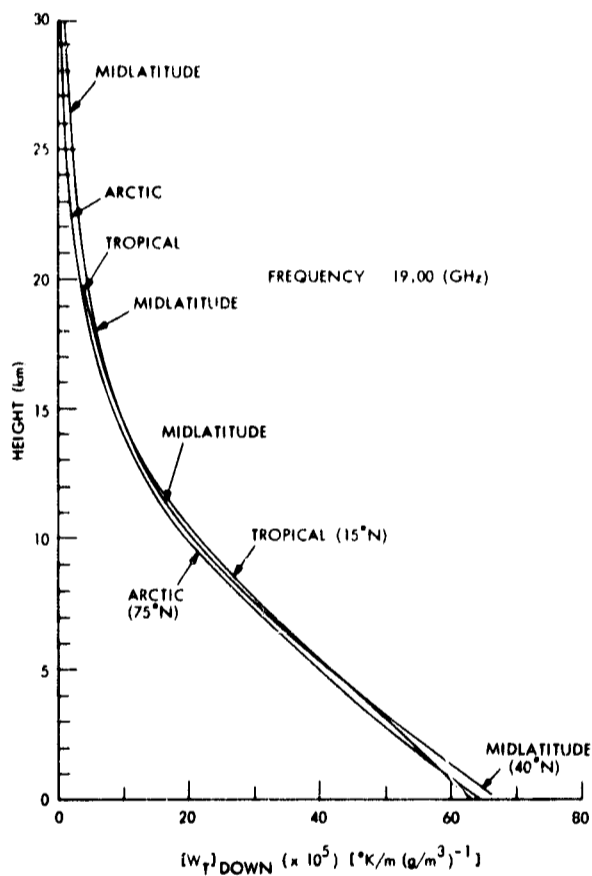
Fig. 20.

Climatic variations in the 19-GHz emission weighting function for observations from space.

The value of R for all weighting functions has been taken as 0.6, a reasonable value for sea water near 1 cm. The ground (or water) temperature T_g has been taken in each case as the ground-level atmospheric temperature. It must be borne in mind that these weighting functions are quite dependent upon R, T_g, and ϵ near resonance, and therefore those functions depicted in Fig. 19 should be construed as being only illustrative of the most general properties of the downward brightness-temperature weighting functions.
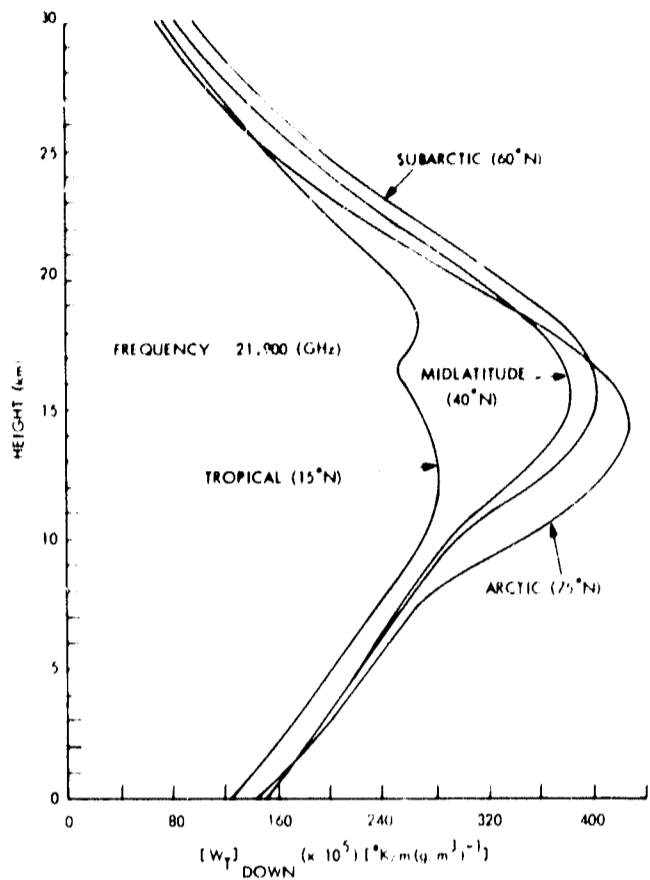
Fig. 21. Climatic variations in the 21.9-GHz emission weighting function for observations from space.
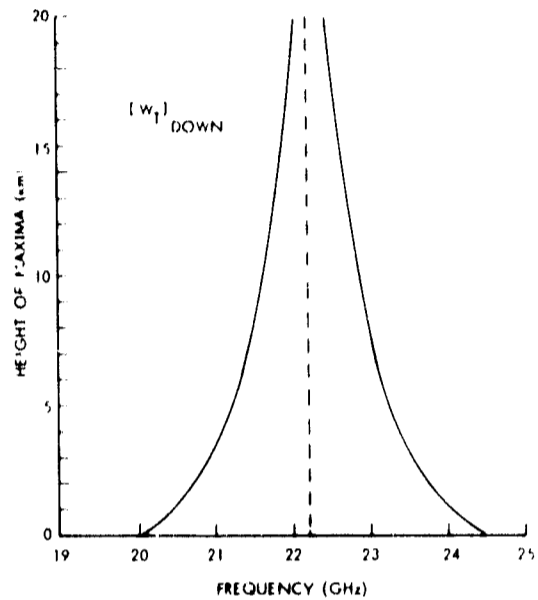
Fig. 22. Frequency dependence of the height at which maxima occur for nadir emission weighting functions.
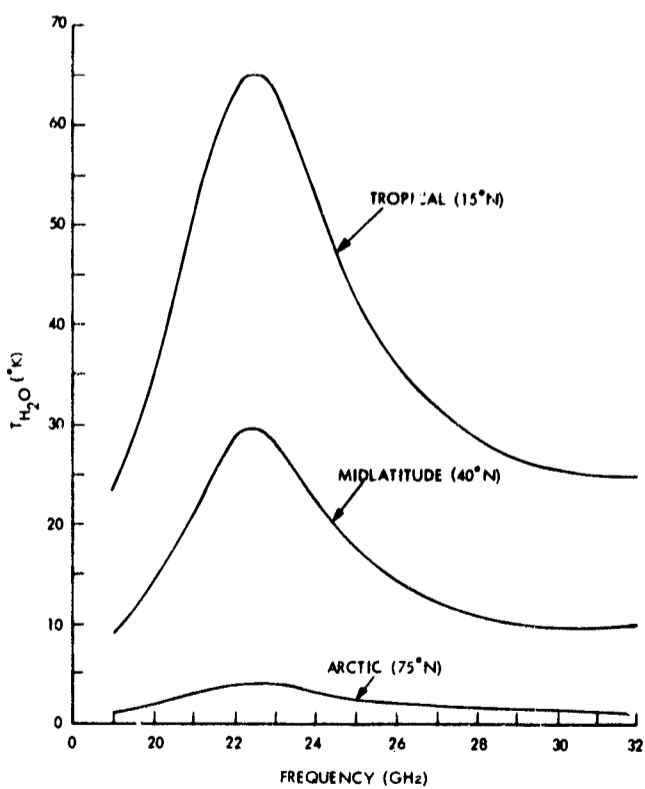
Fig. 23. Atmospheric emission spectra for observations from space for several climatic regions.
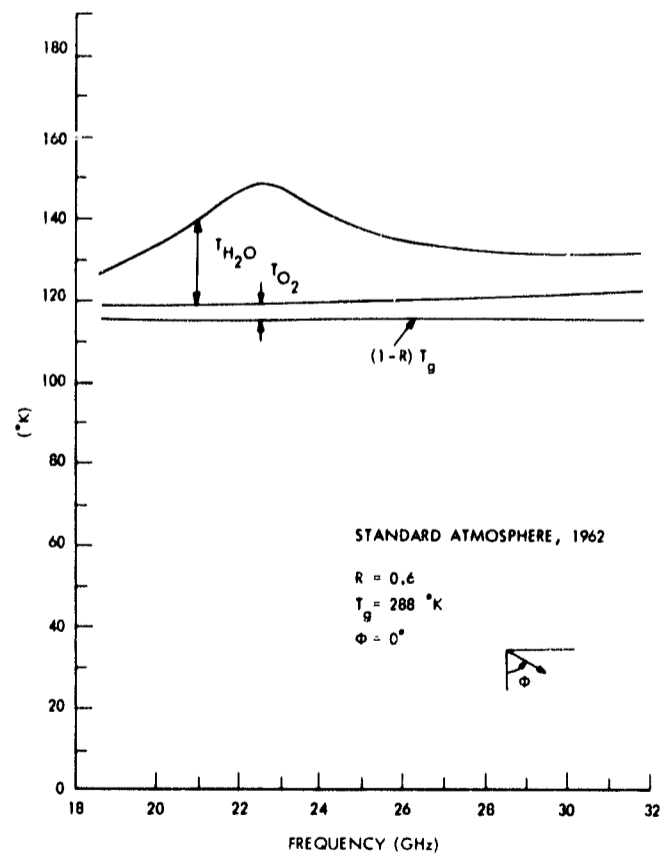
Fig. 24. Contributions to the total emission seen from space by water vapor, oxygen, and the surface of the Earth.

37

The shapes of the weighting functions for the water vapor part only of the emission received at a satellite conform closely to the upward-looking weighting functions, as might be expected. The differences, in fact, between the upward and downward brightness-temperature weighting functions are not as great as those caused by climatic variations within either group. The stability of the 19.0-GHz weighting function shown in Fig. 20 is somewhat greater than its upward-looking counterpart. The 21.0-GHz functions plotted for various climates in Fig. 21 are quite divergent above 8 km, but they have the redeeming feature that below 8 km the midlatitude, subarctic, and Arctic curves are closely similar. Only the tropical curve deviates substanti .iy from the others. Most of the discrepancy is caused, however, by ignoring ϵ, since the attenuation for this atmosphere is approximately 1.1 dB at 21.9 GHz.

The height at which the maximum sensitivity occurs at a given frequency is plotted in Fig. 22. The separation of the curves is slightly greater than for the upward-looking curves but slightly less than for the similar opacity curves.

The amplitude of T_{H_2O} for the Tropical, Midlatitude, and Arctic atmospheres is shown in Fig. 23. The amplitudes are similar to those computed for ground-emission measurements.

Finally, the total brightness temperature that might be observed by a satellite in midlatitudes is depicted in Fig. 24. The bulk of the radiation originates from the ground-emission term of Eq. 68, a small contribution increasing with frequency comes from the oxygen term, and the rest from the water-vapor term. The effect of clouds would tilt the high-frequency side of the curve upward an amount that depends, for the most part, upon the liquid water content of the clouds in the beam. The curves in Fig. 25 and Fig. 26 have been calculated with the aid of (56) and, therefore, have no approximations in them.

3.4 THE 183.3-GHz RESONANCE OBSERVED FROM GROUND LEVEL, BALLOON, AND SPACE

The water-vapor spectral line at 22.2 GHz is a relatively weak line, seldom reaching a total atmospheric attenuation of 1.5 dB at resonance. In contrast, the 183.3-GHz resonance is a very strong spectral line. How strong may be deduced from Fig. 25. In the moist tropical regions, the peak one-way attenuation through the atmosphere reaches more than 200 dB. In dry Arctic regions the peak attenuation falls below 20 dB, still, however, optically thick. In midlatitudes, at frequencies as low as 150 GHz, the zenith attenuation falls to approximately 2 dB, a value that is greater than the attenuation expected anywhere over the Earth for the 22.2-CHz line.

For surface measurements, such a strong line effectively screens off all radiation originating very far from the receiving antenna. The attenuation factor in the integral on the right-hand side of (47) is only small enough to allow radiation to reach the
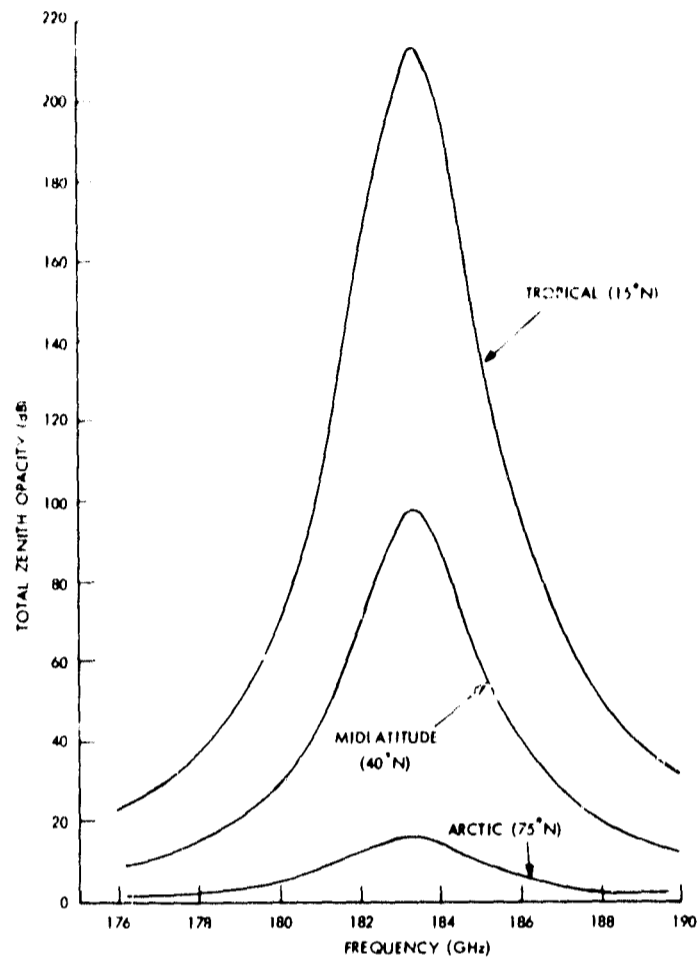
Fig. 25. Total zenith opacity for a spectral region near 183.3 GHz for several mean climatic conditions.
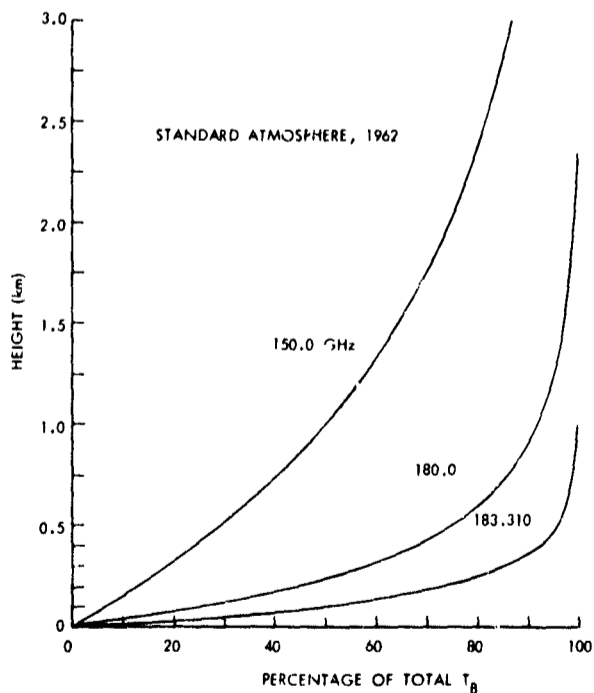
Fig. 26.

Percentage of the total energy received from layers of increasing thickness at several frequencies.
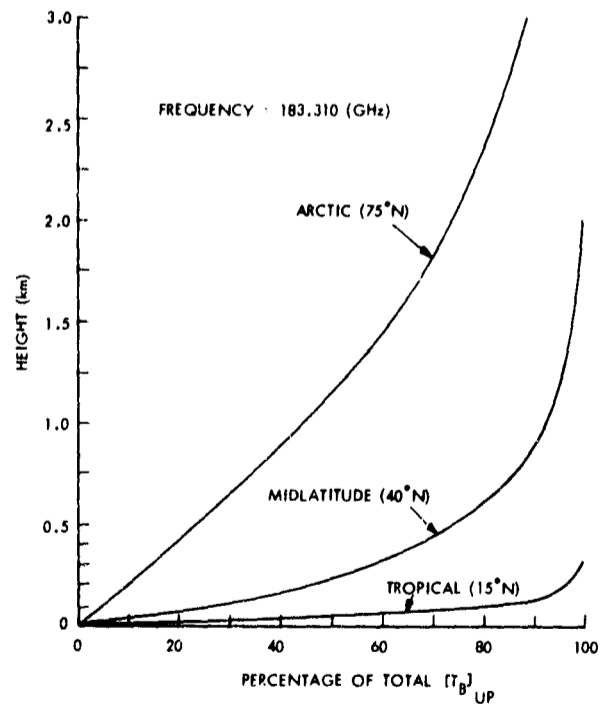
Fig. 27.

Percentage of the total energy received from layers of increasing thickness at 183.31 GHz in several mean climates.

antenna from distances very close to the receiver. The first term of the same equation, of course, is totally lost. For surface measurements, one would expect a uniform temperature over a wide band of frequencies centered on resonance. This is exactly what occurs.

The cumulative percentage of the radiation that makes up the signal measured by a ground-based radiometer is plotted against height in Fig. 26 for a midlatitude Standard Atmosphere. Three frequencies are shown: resonance (183.310 GHz), a frequency at which the attenuation is reduced approximately two-thirds (180 GHz), and another frequency far below resonance (150 GHz). The heights below which 90% of the radiation originates for each of the frequencies are 480 m, 875 m, and 3500 m, respectively.

In Fig. 27, the variation of this cumulative percentage vs height for several climates is shown for one frequency, in this case, resonance. The 90% heights vary from 125 m in the Tropical atmosphere to 3250 m in the Arctic atmosphere.

The curves for satellite observations with the 183-GHz line show that the meteorological information to be gained is confined to the stratosphere. Since Section V is devoted to the stratosphere, we shall defer discussion of relevant curves for 183-GHz observations from space.

IV. OBSERVED AND COMPUTED ATMOSPHERIC ATTENUATION
OF SOLAR RADIATION

During the summer of 1965 and the winter of 1966, an extended program was conducted to obtain high-quality atmospheric opacity measurements near the 22-GHz rotational resonance of water vapor. The measurements were taken at Lincoln Laboratory of the Massachusetts Institute of Technology. Radiosondes were launched nearby to monitor atmospheric conditions during the periods of radiometer observations. The data that they returned were used as a basis to compute the expected absorption for that day. The purpose of this section is to compare the absorption computed from the radiosonde data with the actual radiometric observations.

4.1 MEASUREMENT OF ATMOSPHERIC ATTENUATION OF
SOLAR RADIATION NEAR 1 cm

A microwave radiometer measures energy over a given bandwidth centered at some frequency in the microwave range of frequencies. The antenna temperature is the quantity actually recorded and is related to the brightness temperature distribution surrounding the antenna as follows:

$$T_A(\theta', \phi') = \frac{1}{4\pi} \int_{4\pi} G(\theta - \theta', \phi - \phi') \, T_B(\theta, \phi) \, d\Omega. \tag{71}$$

Here, $T_A(\theta', \phi')$ is the temperature that a black body would have to produce the same average intensity over the spectral interval that is being monitored, $G(\theta - \theta', \phi - \phi')$ is the power gain function of the antenna whose axis is pointed at an elevation angle of θ' and an azimuth angle of ϕ' measured with respect to an arbitrarily chosen reference system, and $T_B(\theta, \phi)$ is the brightness temperature distribution that the antenna is monitoring. The integral is taken over all solid angles. T_A may be more clearly related to T_B in the following manner. By using the power gain function as a weighting factor, an average brightness temperature may be computed as

$$\overline{T}_B = \frac{\frac{1}{4\pi} \int_{4\pi} G(\theta - \theta', \phi - \phi') \, T_B(\theta, \phi) \, d\Omega}{\frac{1}{4\pi} \int_{4\pi} G(\theta - \theta', \phi - \phi') \, d\Omega}. \tag{72}$$

However,

$$\frac{1}{4\pi} \int_{4\pi} G(\theta - \theta', \phi - \phi') \, d\Omega = \eta_R, \tag{73}$$

where η_R is the radiation efficiency of the antenna at the wavelength and for the conditions of the measurements. Therefore it follows that

$$T_A = \eta_R \overline{T}_B. \tag{74}$$

For antennas of highly precise surface contours and large apertures, the pow   gain function is so distributed that the brightness temperature in a region only a small angular distance around the antenna axis contributes significantly (typically 60%) to $\overline{T}_B$.

The equation governing the brightness temperature at a surface-based antenna pointing up into a planar, horizontally stratified atmosphere has been shown (see Sec. III) to be

$$T_B(\nu) = T_E \, e^{-\int_0^H \gamma(\nu,z)\sec\theta\, dz} + \int_0^H \gamma(\nu,z)\, T_{AT}(z)\, e^{-\int_0^Z \gamma(\nu,z)\sec\theta\, dz'} \sec\theta\, dz, \tag{75}$$

in which T_E is the brightness temperature of any source outside the atmosphere, but filling the antenna beam.

The second term of Eq. 75 was effectively eliminated by a carefully chosen observational procedure.

1. Observations of the sun were made. T_E is, therefore, T_s, the brightness temperature of the sun at the frequency of observation.

2. An antenna was used whose main beam was considerably smaller than the angular size of the sun's disk at all observed frequencies.

3. Drift scans were taken of the solar disk by placing the antenna axis ahead of the apparent path of the sun across the sky, recording the brightness temperature of the sun plus atmosphere, and, after the sun had moved through the beam, recording the atmospheric contribution alone.

4. Finally, the atmospheric contribution was subtracted from the combined total of sun plus atmosphere.

This procedure leaves one with

$$T_B(\nu) = T_s \, e^{-\int_0^\infty \gamma(\nu,z)\sec\theta\, dz} = T_s \, e^{-\tau_{max}\sec\theta}. \tag{76}$$

The contribution of the atmosphere in (76) is now confined to the integral exponent of e; however, the direct use of (76) is associated with many practical difficulties.

Even though T_s may be constant in time, the exact value may be imperfectly known. Furthermore, the absolute measurement of T_B introduces difficulties to the measurement; the absolute gain of the antenna must be known and careful calibrations must be performed. Since the absolute value of neither T_s nor T_B contains information about the atmosphere, the necessity for measuring them absolutely is eliminated by manipulating Eq. 76. First, restate (76) as

$$C_1 T_B'(\nu) = C_2 T_s' \, e^{-\tau_{max}\sec\theta}, \tag{77}$$

where the real brightness temperature that is being measured is $T_B = C_1 T_B'$, and the actual solar brightness temperature is $T_s = C_2 T_s'$, with C_1 and C_2 constants. If (77) is rearranged and the natural logarithm of both sides is taken, we have

$$\ln\left\{\frac{T_B'}{T_s'}\right\} = \ln\frac{C_2}{C_1} - \tau_{max}(\nu)\ \sec\ \theta. \tag{78}$$

Finally, by making several drift scans at different values of sec θ, one may compute τ_{max} from the following finite-difference equation:

$$\tau_{max}(\nu) = -\frac{\Delta\ln\left\{\dfrac{T_B'(\nu)}{T_s'(\nu)}\right\}}{\Delta(\sec\ \theta)}. \tag{79}$$

It is clear from Eq. 79 that in order to measure $\tau_{max}(\nu)$ it is only necessary to measure quantities that are proportional to T_B and T_s, or to their ratio as a function of zenith angle. This simplifies the experimental procedure and divorces the results from any absolutely calibrated measurements. This method was first used, in 1946, by Dicke, Beringer, Kyhl, and Vane.[34] The equipment that was used to measure the T_B' of Eq. 77 consisted of a five-channel radiometer constructed and operated by M.I.T. staff and personnel.[35]

While the sun scans were being taken, observations were made visually on the general weather conditions, and the conditions that the antenna saw (via a bore-sighted television camera). Both were recorded. Furthermore, the hourly weather observations taken at L. G. Hanscom Field, at Bedford, Massachusetts (U.S. Air Force Base approximately 1 1/2 miles away), were also recorded.

A typical summer day's data comprised approximately 20 scans. The maximum number of scans for any day was 36. In winter, the average number was closer to 10 scans per experiment.

4.4.1 Reduction of the Data

Considerable attention was given to the reduction of the data in order to extract from it the most accurate values of atmospheric attenuation that could be obtained by the available equipment. Filtering included a numerical investigation to see at what elevation angles the planar approximation of the atmosphere was no longer valid. It was determined that in sun scans whose values of secant θ were no more than 9, errors of less than 2% would be introduced by the sphericity of the Earth. Therefore, data were used whose zenith angles were less than 82° 49' (elevation angles greater than 7° 11'). At these angles, refraction was negligible.

4.2 COMPUTED ATMOSPHERIC ABSORPTION DERIVED FROM RADIOSONDES

Thirty-two days of radiosonde information were gathered, together with solar extinction data. The original plan intended for these radiosonde runs was to monitor

conditions that the antenna beam was viewing, and use the computed spectra therefrom as a standard of comparison. This, of course, was under the assumption that the distance separating the sondes and antenna beams and the time differences between sonde launches and radiometer experiments would introduce errors that would not invalidate the expected correlations. From the comparison of computed-to-observed spectra these assumptions proved to be poor in many cases. The conditions under which they break down have been analyzed in several cases and they have been documented.

To investigate the error introduced by using finite bandwidths, calculations were performed simulating the effect of the bandwidth and sidebands for the equipment used in the experiments. The bandwidths of the radiometers were 8 MHz centered ±30 MHz from the local-oscillator frequency.

The results of the computations showed that for the most extreme atmospheric conditions that were investigated, the largest deviation between the average attenuation of the two sidebands and the attenuation at the local-oscillator frequency was 0.0012 dB, a negligible difference when other errors are considered. Of the average attenuation over a sideband, only one of the values differed by as much as 1 unit in the fifth decimal place from the absorption calculated at the center of the band.

4.3 COMPARISON BETWEEN MEASURED ATTENUATION AND COMPUTED ABSORPTION

The radiometer attenuation as computed from Eq. 79 at 5 frequencies and the absorption as computed from the radiosonde data for selected experiment days is plotted in Figs. 28-30.

4.3.1 Presentation of Comparable Spectra

The data presented in each figure include: (i) date of the experiment followed by the time over which radiometer data were taken; (ii) observed weather conditions recorded under these dates and times; (iii) radiometer results recorded as single dots in the middle of probable error bars (the errors represent one standard deviation as computed from Eq. B.12 in Appendix B); (iv) a solid spectral curve computed from the data returned by the radiosonde flown on the day of the experiment; and (v) a dashed spectral curve that may be called "matched spectra." This spectral curve is derived by taking one of the observed spectral data points (21.9 GHz in the summer data, and 22.235 GHz in the winter data) and multiplying the radiosonde moisture profile by a factor that causes the computed absorption to match the observed attenuation (difference <0.001 dB) at this one frequency. Its uses will be apparent as we proceed.

Four general criteria were employed in classifying the weather groups: (i) stable conditions, most days clear; (ii) days on which moisture-laden air approached the antenna site from the West; (iii) days on which dry air was approaching the antenna site from the West; and (iv) very unstable conditions manifested by considerable cumulus clouds, towering cumulus clouds, and/or thunderstorms.
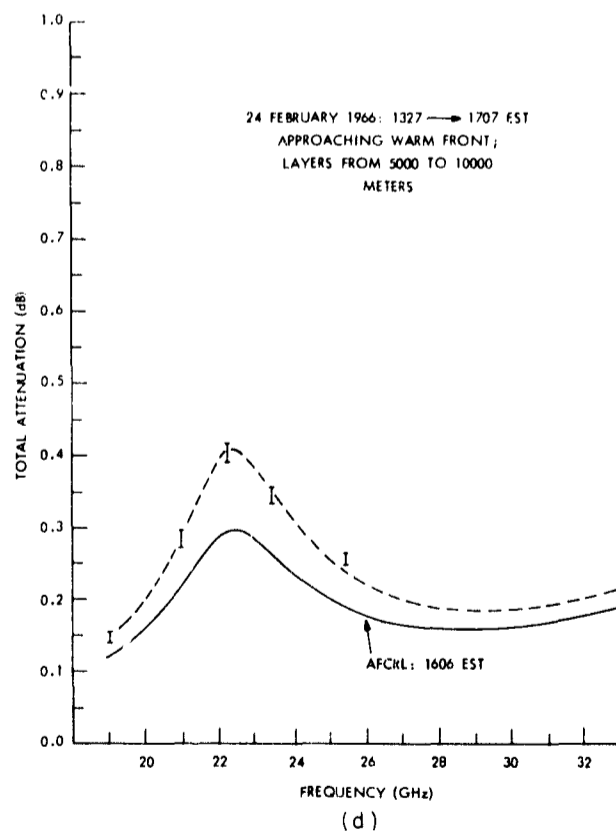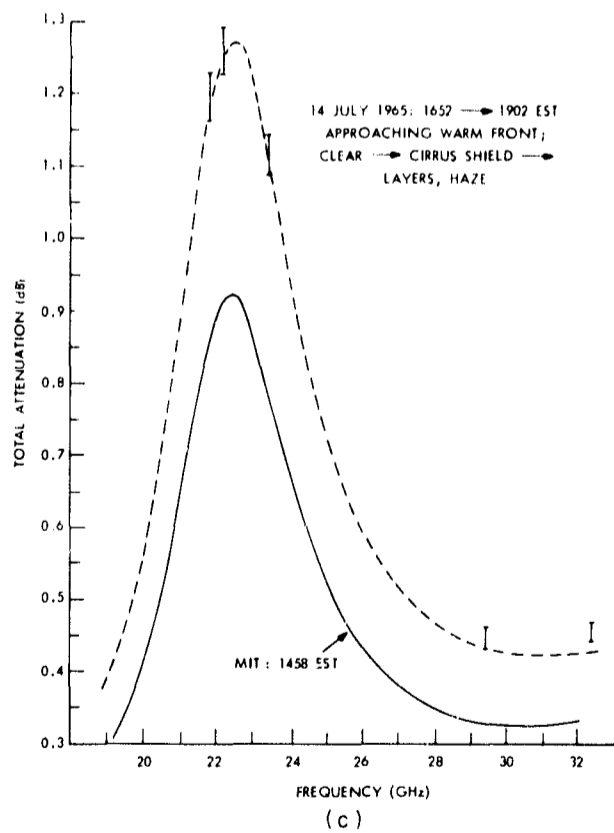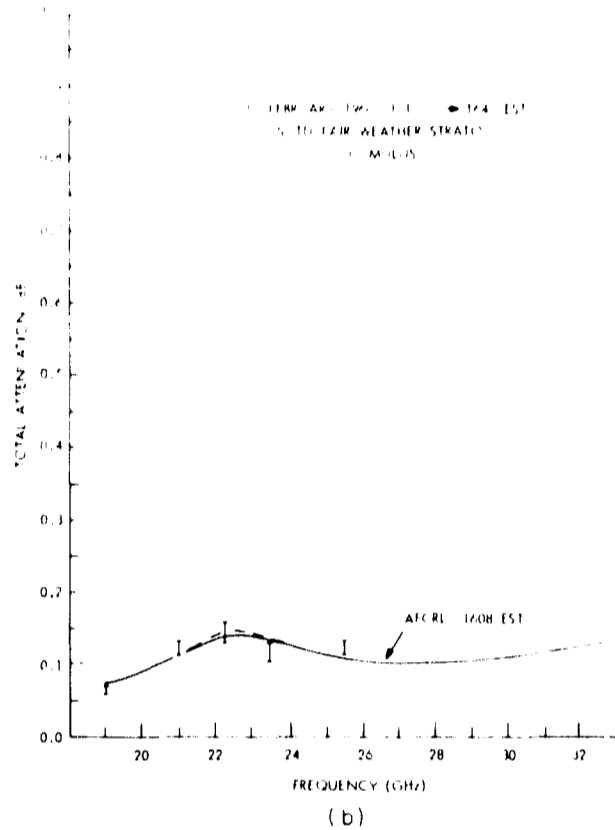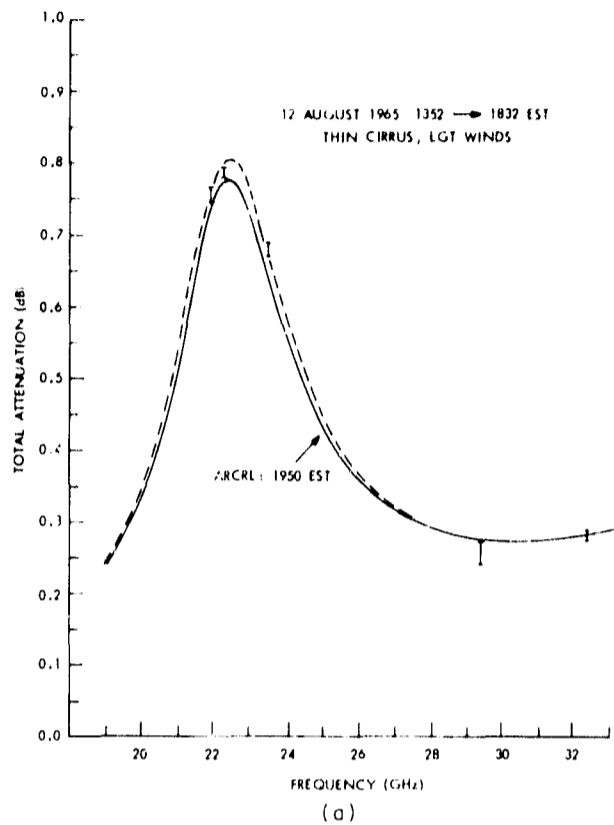
Fig. 28. Comparison of radiometer and radiosonde data.

4. 3. 2 Similarities among Spectral Pairs within Weather Groups

Figures 28 and 29 are broken down into the groups defined above as follows.

Date	Group		Conditions
12 August 65		Fig. 28a	Summer: stable, clear or clear weather for the most part
	1		
17 February 66		Fig. 28b	Winter: stable, clear or clear weather for the most part
14 July 65		Fig. 28c	Summer: approaching moist air mass
	2		
24 February 66		Fig. 28d	Winter: approaching moist air mass
15 July 65	3	Fig. 29a	Summer: approaching dry air mass
10 August 65	4	Fig. 29b	Summer: unstable, very moist conditions

Each figure best represents its spectral class. In every case several examples of each set of conditions were obtained during the many days of experiment.

Figure 28a probably represents the closest correspondence that can be expected from radiometer and radiosonde data. Since it is typical of the spectra taken on stable days, it represents, too, the best data in this experiment for comparing theoretical with true line shape. In this regard, the most that can be said is that the theoretical line shape that was used is certainly adequate within experimental error. Figure 28b represents spectra taken on a dry, stable winter day. Its over-all low amplitude is in contrast with that of Fig. 28a. There appears to be little or no bias in the observations on the basis of total water-vapor content.

The second group of spectra (Fig. 28c and 28d) represents conditions in which the radiometer is viewing air streaming toward the antenna which contains increasing amounts of moisture. Data for this type of spectra have been taken early in the afternoon and show a drier atmosphere than that measured by the radiometer later in the day. In most instances, the approaching moist air mass accompanies warm frontal activity. Invariably, the radiosonde is swept in a direction which the dry air takes, which heightens the moisture contrast between the radiosonde and radiometer beam.

Figure 29a represents a day on which a dry air mass is replacing a more moist one. The radiosondes were launched before the radiometer observations were completed and therefore the radiosondes measured a considerably more moist atmosphere than did the radiometer.

The final figure (Fig. 29b) represents days on which very unstable atmospheric conditions were encountered. Cumulus development was marked, and thunderstorm activity was observed. Three radiosondes were launched to monitor conditions. Gross
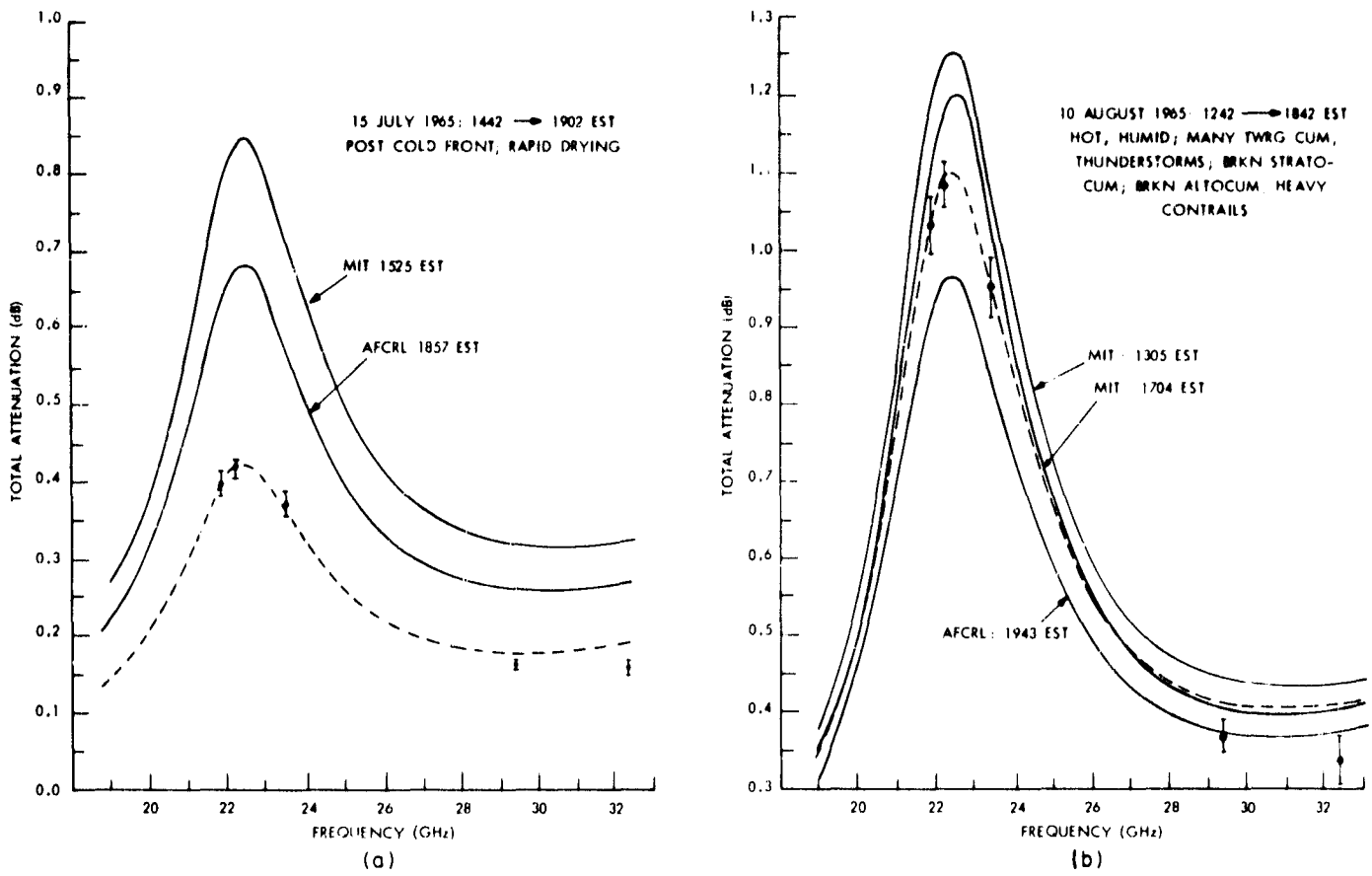
Fig. 29. Comparison of radiometer and radiosonde data.
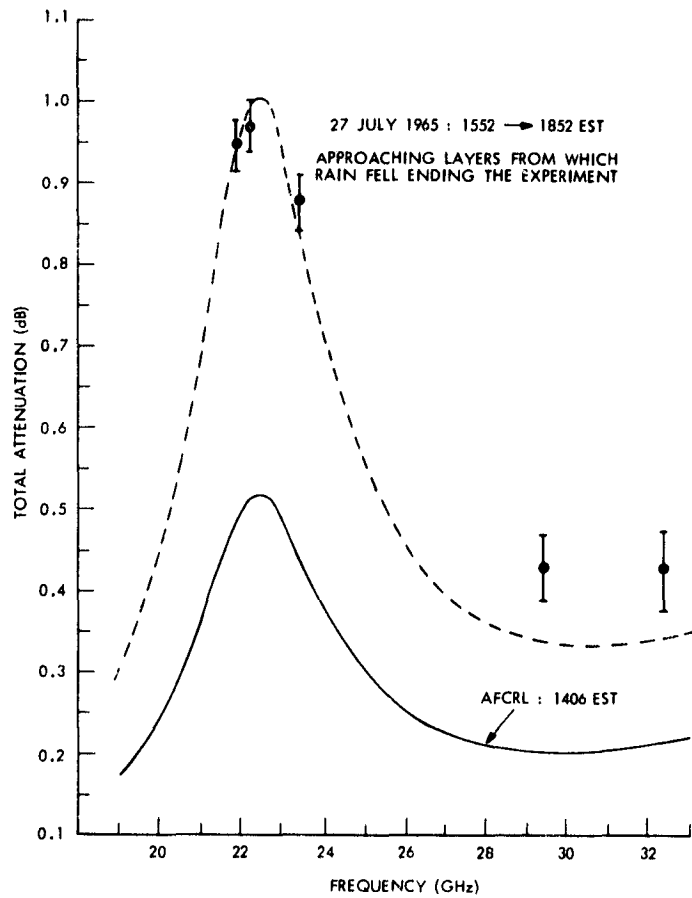
Fig. 30. Effect of cloud-droplet absorption on the observed spectral shape.

differences in the observed and computed spectra are apparent; radiometer measurements show large probable errors; the amplitude of the observed spectra falls between the computed amplitude for the various radiosonde moisture profiles.

A final figure is included which illustrates what must be a strong effect of absorption by cloud droplets. Figure 30 shows how the spectral dependence of cloud-droplet absorption has considerably distorted the observed spectral shape. The higher frequency data points are well above the matching spectral amplitude. And since moist air was streaming in aloft, any distortion of the matched spectra which was due to the use of the vertical shape of the moisture curve derived from the radiosonde should have been in the direction of a more broadened line. The absorption discrepancy in the high-frequency wing could be even more pronounced than is shown. The fact that the clouds were rain-bearing indicates how well microwaves penetrate even dense cloud formations.

It is quite clear from Figs. 28-30 that it is not possible, except perhaps on days with the most stable conditions, to routinely compute absorption in the microwave region from radiosonde data and expect it to reliably reflect what might be observed by a radiometer. Spatial and temporal gradients of moisture preclude the use of the radiosonde information as a useful areal or temporal average profile. Indeed, when proper calibration of a radiometer is taken, there are strong reasons to believe that, at least for integrated water vapor, the average radiometer is able to measure this quantity more accurately than the average radiosonde.

V. DETECTION OF STRATOSPHERIC WATER VAPOR BY MEANS OF MICROWAVE MEASUREMENTS

On the basis of high-altitude balloon measurements of uncondensed water vapor,[36-38] Barrett and Chung[39] predicted, in 1962, that an anomalous emission "spike" should be apparent in ground-based microwave observations of the atmosphere at frequencies very near the 22.237-GHz water-vapor rotational resonance. This would be the result of excess water vapor in the stratosphere, excess being determined to be an increase in the water-vapor mixing ratio, with height somewhere in the region above ~30 km.

Since publication of Barrett and Chung's paper, at least one attempt has been made to detect the spike,[40] besides the effort reported here. That effort showed negative results.

5.1 STRATOSPHERIC WATER VAPOR AND ITS RELATIONSHIP TO MICROWAVE MEASUREMENTS

The earliest authoritative measurements of water vapor in the lower stratosphere were made in Britain, soon after World War II. (For a review of the measurements of stratospheric water vapor before 1961 see Gutnick.[41]) These measurements from aircraft showed a sharp decrease in moisture as the tropopause was penetrated. On the basis of these measurements, a stratospheric water-vapor model was predicted which showed that the entire stratosphere was quite dry.

Other investigations of stratospheric water vapor were conducted with the use of balloons and humidity sensors. The results from many of these flights contradicted the British model, by showing that, even though a dry region existed just above the tropopause, the absolute density of water vapor at altitudes above approximately 20 km did not decline many times, and on some occasions even increased with height. The resonant spike predicted by Barrett and Chung was based on such measurements.

One of the major problems that had to be overcome for balloon measurements was outgassing of water vapor from the measuring apparatus. As apparatus and techniques have become more sophisticated, especially with respect to the contamination problem, the very wet stratospheres measured in the 1950's and early 1960's did not occur. Measurements below 30 km at low, middle, and high latitudes, in 1964 and 1965, by Mastenbrook,[42] and at midlatitudes by Sissenwine and his co-workers,[43] tend to confirm a generally dry stratosphere. Some of the runs do, however, show trends near the peak altitudes which have interesting implications for the region above 30 km.

5.1.1 Model Atmospheres for the Simulation of Stratospheric Microwave Absorption and Emission

In order to better understand the origin and nature of the stratospheric water-vapor spike, some model atmospheres have been constructed and investigated. They are presented in Figs. 31, 32, and 33. Their temperature profiles are the Standard
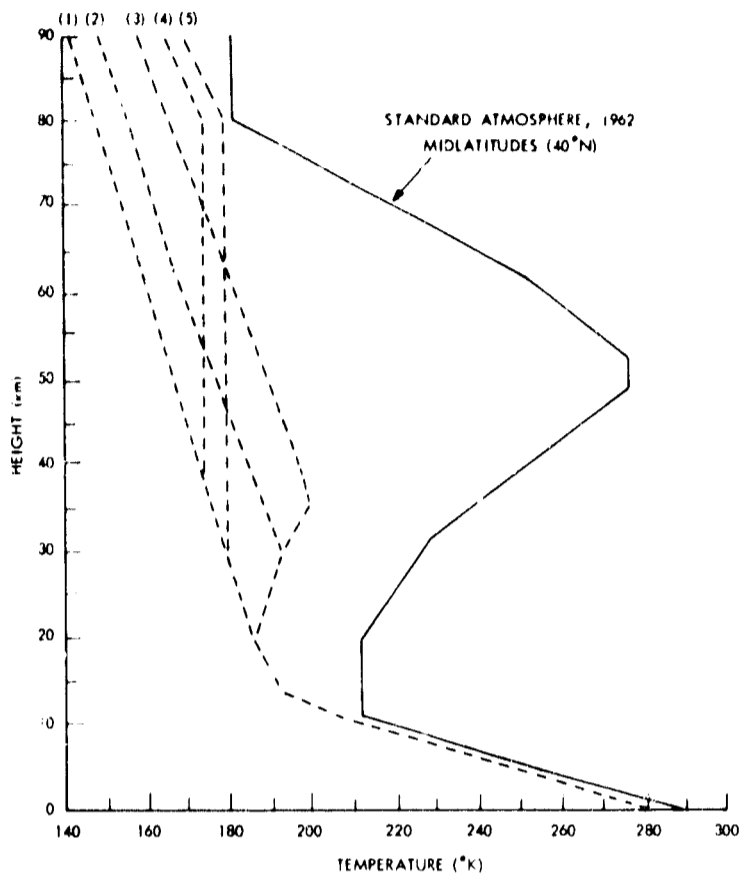
Fig. 31. Standard atmosphere (midlatitude), 1962, with 5 hypothetical moisture distributions.
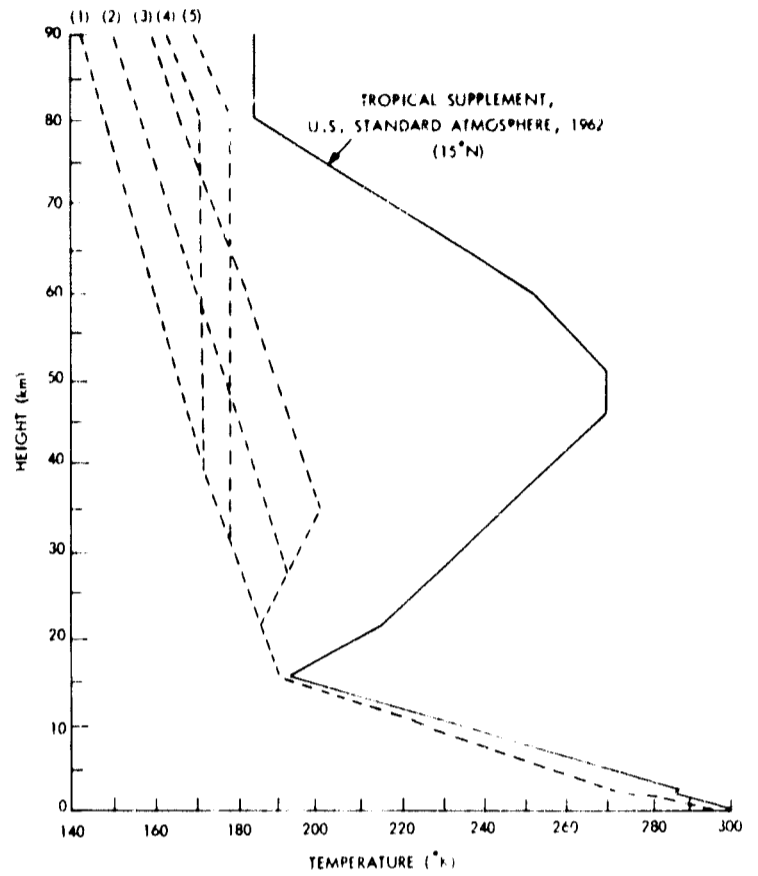

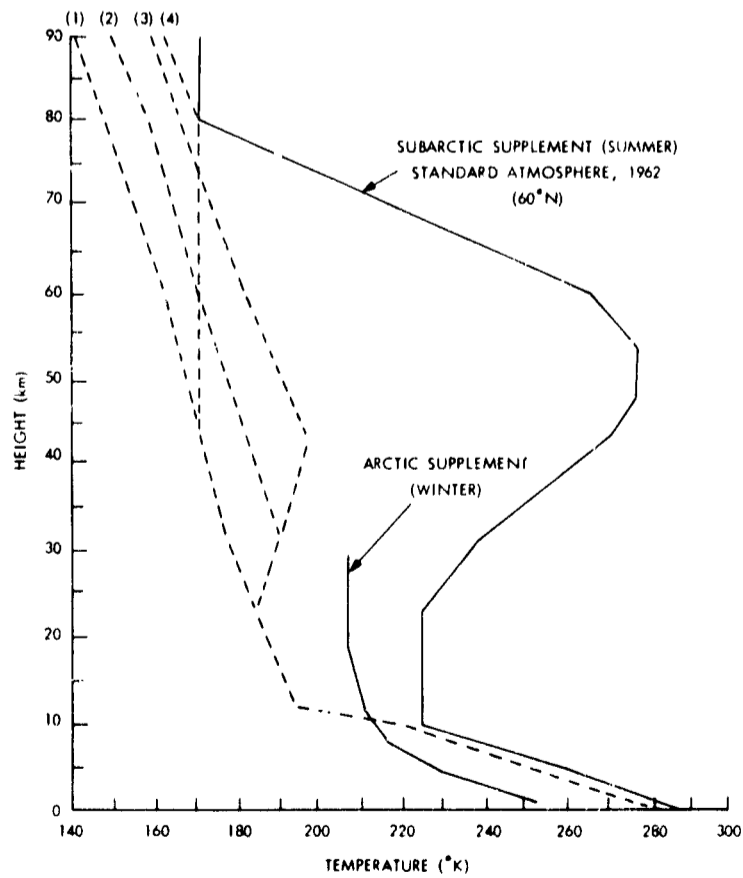Fig. 32. Tropical supplemental standard atmosphere with 5 hypothetical moisture distributions.

Fig. 33. Subarctic (summer) supplemental standard atmosphere with 4 hypothetical moisture distributions.

Atmosphere, 1962 (midlatitude), and the Tropical and Subarctic (summer) supplements thereto, as presented in the Handbook of Geophysics and Space Environments.[32] (An Arctic supplemental atmosphere appears with the Subarctic atmosphere, but extends only to 30 km. The distribution of temperature above this level was not available. The profile is included because it was used for the analyses in Section III.) The moisture curves for the atmospheres (represented as dew point-frost point curves) up to the 10-km level are means for the latitudes represented. They are also reported in the Handbook of Geophysics and Space Environments.

Above 10 km, distributions of moisture have been extended to 28 km, based on the profiles reported in either Mastenbrook or Sissenwine. Five hypothetical distributions of water vapor above the 29-km level have been suggested for the Tropical and Midlatitude atmospheres, and four for the Subarctic.

The moisture distribution in each case can be smoothly extended to 90 km. The possibility that photochemical reactions above the 70-km level may deplete the available water vapor supply is neglected, as suggested by Hunt.[44] The effects of excess water vapor above the 70-km level will show up, however, in our calculations as a very narrow extension of the spike that we are investigating. Its presence will alter the results that are most interesting to us very little, that is, the results in which the finite bandwidth of the radiometer is taken into consideration. And the question of whether saturation does occur in the region of 80 km, where noctilucent clouds have been observed, is left open. The particles making up the clouds may be meteoric dust with coatings of ice.[45] The Subarctic Supplemental Atmosphere, which has the lowest temperature at the mesopause of all of the model atmospheres, and is representative of the latitudes and season for noctilucent clouds, has one hypothetical moisture distribution which is saturated at the 80-km level.

All of the moisture profiles below 30 km for the atmospheres presented do not exceed in absolute water-vapor density the wettest atmospheres reported by Mastenbrook. The water-vapor profiles above 30 km attempt to follow some of the trends that were evident in the observed data near the top of their ascents. The exact profiles are necessarily subjectively determined.

In the Tropical and Midlatitude Atmospheres the profiles are constructed with the approximate scheme of having constant mixing ratios of 2×10^{-6} gm of water vapor per gram of dry air for profile (1), 2×10^{-5} g/g for profile (2), 2×10^{-4} g/g for profile (3), and two profiles, (4) and (5), which have constant water-vapor densities above a certain level. The constant mixing-ratio profiles, when these ratios are greater than the mixing ratios in the lower stratosphere, have been achieved by increasing the water vapor just above the 30-km level.

The Subarctic atmosphere is similar, except that there is only one constant vapor density case. This case, however, provides for saturation at the mesopause. Whether or not saturation occurs at the mesopause during the occurrence of noctilucent clouds

the atmospheres in Fig. 34. The slight upturn at 75-80 km is due to the relatively increasing importance of Doppler broadening at these levels. It depends only upon the square root of the temperature and therefore fluctuates less than one order of magnitude over the entire lower 100 km of the atmosphere. It should be noted that at approximately 72 km, the line half-width has narrowed to 100 kHz, and by 90 km is roughly 25 kHz.

5.1.3 Stratospheric Water-Vapor Spike Produced by Model Atmospheres

If the absorption is computed for the Midlatitude Standard Atmosphere of Fig. 31, we would obtain the spectrum plotted in Fig. 35. The middle spectrum is that which a
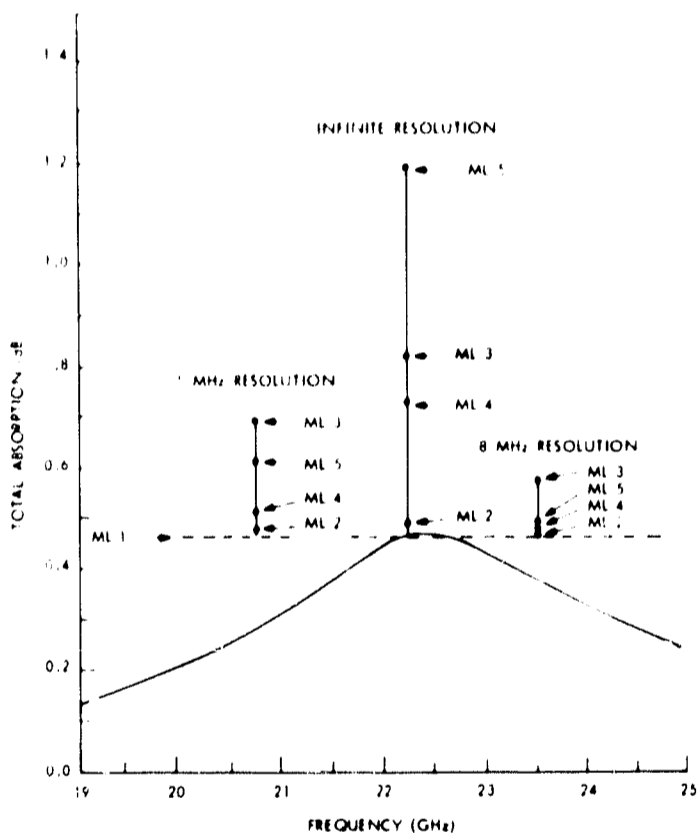
Fig. 35. Comparison among opacity spikes seen by radiometers with zero, 1-MHz, and 8-MHz bandwidths.

radiometer of infinitely small bandwidth would see. The designations ML1, ML2, etc. are indicators of the height of the spike for each of the stratospheric vapor variations numbered in Fig. 31. The constant mixing ratio case for the driest atmosphere (w = 2×10^{-6} g/g) shows no spike at all. The most pronounced spike is produced by the atmosphere which shows a constant frost point (and therefore a constant water-vapor density) above 30 km. This is quite expected after considering that this model places the greatest amount of water vapor at the highest levels.

It is conceivable that technology might produce acceptable radiometers of bandwidths near 1 MHz sometime in the future. If so, the spikes will be altered by the intrinsic averaging that such a finite bandwidth imposes, as shown by the spike drawn on the left in Fig. 35. The relative heights of the spike produced by the various model stratospheric moisture distributions are now altered toward those atmospheres with the

greatest total moisture above 30 km.

If the bandwidth is 8 MHz, as it was in each sideband of the radiometer used for the measurements reported in Section IV, then the spike would be further reduced to that shown on the right in Fig. 35.

Finally, if the radiometer has a double sideband, then all of the spike heights must be reduced by one-half again. In the case of the 8-MHz bandwidth spikes, the chances for detecting any but the most moist stratospheric conditions, when errors of 0.01 dB are expected, appear to be very slim.

5.2 RESULTS OF OPACITY MEASUREMENTS AT 22.237 GHz

One of the purposes of the summer observations reported in Section IV was to search for the stratospheric water-vapor spike. Accordingly, one of the five radiometers was tuned so that one of its two sidebands covered the frequency region at and near 22.237 GHz. From the discussion in section 5.1.2 about double-sideband 8-MHz resolution radiometers, it would not be unexpected that results were negative. The one fact that was established was that on only one day ('4 July 1965) did the absorption at 22.237 GHz exceed the value that might have been expected from water vapor in the troposphere alone. The matched spectra always equalled or exceeded the absorption observed at 22.237 GHz, when at 21.9 GHz the observed attenuation and computed absorption were numerically equal

Besides those shortcomings of the experimental design which have been brought out, other experimental problems reduced the chances of detecting a spike, if it had existed: (i) the local oscillator for the resonant frequency radiometer drifted in frequency, how much during any one experiment is uncertain; and (ii) atmospheric inhomogeneities and variability increased the noise levels on many days well above 0.01 dB.

5.2.1 Ground-Based Brightness Temperature Measurements near 22.237 GHz

Figure 36 shows the spikes one would measure if he were monitoring atmospheric emission in the model midlatitude atmospheres. The relative amplitudes of the spikes are not changed substantially from the opacity cases. Linewidths of the various spikes are similar to those in the opacity computations, and, therefore, the effect that a finite-bandwidth radiometer produces is similar to those documented in Fig. 35 for opacity measurements.

5.2.2 Opacity and Brightness-Temperature Measurements
from a Balloon

Calculations were carried out on the various stratospheric water-vapor distributions to simulate the measurements that a ... on-borne radiometer would collect at 28 km. They can be visualized for the opacity measurements simply by removing the broad tropospheric absorption base upon which all spikes analyzed thus far have been perched. The only perceivable change occurs in the amplitudes of the brightness-temperature
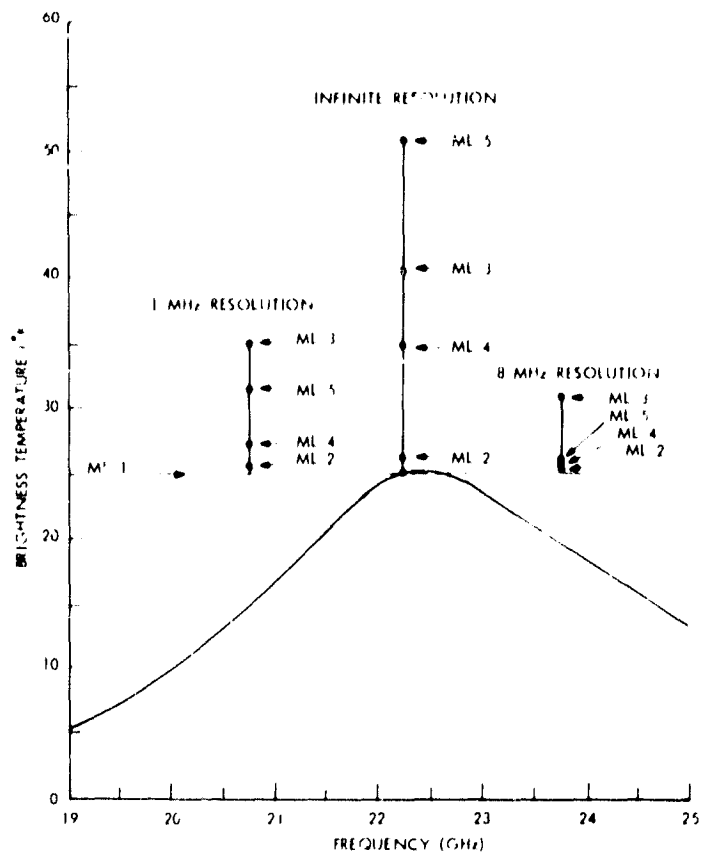
Fig. 36. Emission spikes seen from the ground in the midlatitude atmospheres.
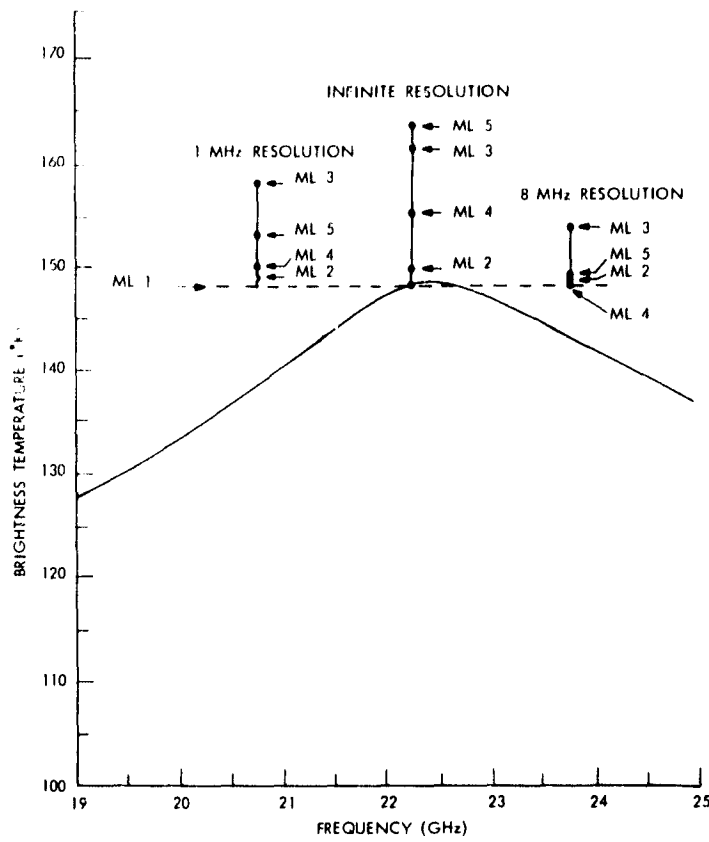
Fig. 37. Emission spikes seen from space in the midlatitude atmospheres.

spikes. They have been raised by a factor of approximately 15%, because of the decreased attenuation between the region in which the spike emission originates and the level of the antenna.

5.2.3 Brightness Temperature Measurements from Space near 22.237 GHz

When a radiometer looks down at the Earth, it sees the background emission attenuated by the atmosphere plus the reflected and direct atmospheric contributions. When the atmosphere is more opaque, the atmospheric contribution increases, but the background radiation is diminished; this compensation reduces the amplitude at resonance from that seen for measurements from the ground at the same frequencies.

Such compensation significantly reduces the spike amplitude as seen from space over a background whose temperature is 288°K and has a power reflection coefficient of 0.6. This is illustrated in Fig. 37. The comparable upward-looking amplitude was plotted in Fig. 36.

The amount of compensation and therefore the amplitude of the spike will vary greatly as the background temperature and emissivity change. For lower reflection coefficients (higher emissivities), the background compensation is greater and the amplitude of the spike is reduced further. Qualitatively similar results were reported by May and Kahle[45] and by Croom.[46]

5.3 MEASUREMENTS OF STRATOSPHERIC ATTENUATION AND EMISSION NEAR THE 183-GHz WATER-VAPOR ROTATIONAL RESONANCE

The 183-GHz water-vapor resonance is nearly two hundred times stronger for similar conditions than the 22.237-GHz rotational resonance. As a result, the sensitivity for monitoring very small amounts of water vapor, such as are found in the stratosphere, is greatly increased for measurements near the higher frequency line.

We shall investigate the results that might be expected from atmospheric measurements near 183.310 GHz.

5.3.1 Stratospheric Absorption and Emission near 183.310 GHz as Measured from a Balloon at an Altitude of 28 km

The 183-GHz line is so intense that measurements from low levels in the troposphere produce brightness temperatures equal to the kinetic temperature of the nearby atmosphere. At 28 km, however, a convenient level for a balloon-borne radiometer to attain, well over 99% of the total water vapor in an atmospheric column is below the balloon. The 22.2-GHz resonance is not capable of measuring emission from the small water vapor above 28 km, except in those stratospheres postulated to be very moist. On the other hand, the 183.3-GHz line is sensitive to the water vapor, even in the driest of the proposed model stratospheres.

In Fig. 38, the zenith absorption near resonance is plotted for the five midlatitude

atmospheric models (Fig. 31) which a radiometer would measure from a height of 28 km. For the stratosphere which contained the maximum integrated water vapor of the five models (ML3), and for the atmosphere with considerable moisture near the mesopause (ML5), the absorption on resonance attains values near 70 dB! Even the driest stratosphere that has been proposed (ML1) has a peak absorption of 0.79 dB. This is often more than the total zenith absorption measured on the ground at 22.237 GHz.
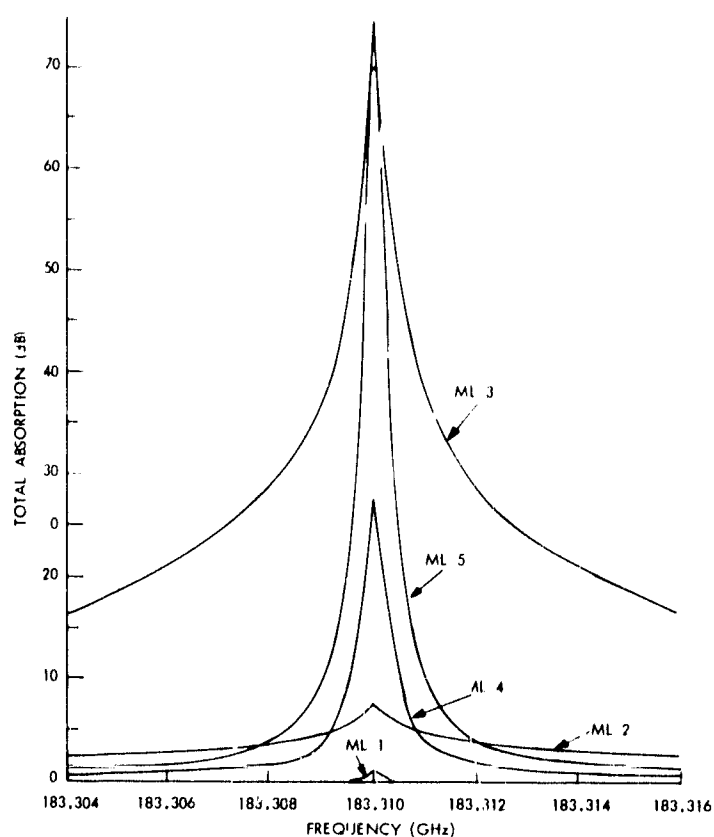
Fig. 38. Possible total zenith opacity in midlatitudes, above 28 km, near the water-vapor resonance centered at 183.310 GHz.
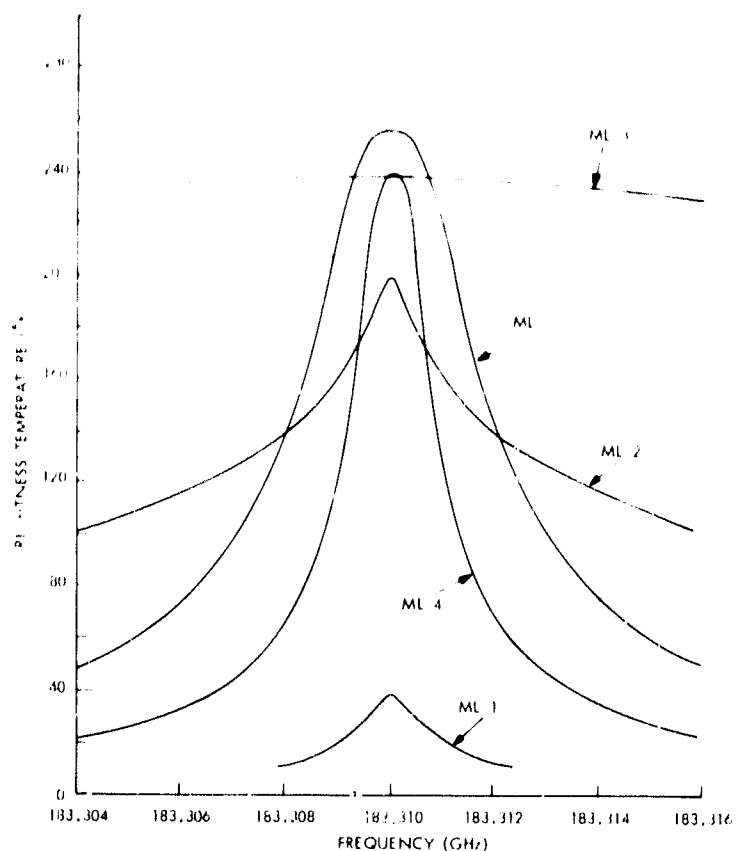
Fig. 39. Emission spectra in midlatitudes, near 183.310 GHz, looking up from a height of 28 km.

If emission measurements were made in the same atmospheres, the spectra plotted in Fig. 39 would be obtained. The sharp peaks of the absorption spectra are now blunted because the coldest temperatures of significance are near the radiometer; higher opacity brings the effective origin of the radiation that is being measured closer to the radiometer and, therefore, into colder source temperatures. The result is to effectively broaden the lines.

A suitable bandwidth for the detection of the 183.3-GHz spike from a balloon would be considerably greater (by approximately 8 to 10) than the bandwidth necessary at 22.2 GHz. This is offset, of course, by the difficulties in building narrow-band radiometers at such frequencies.

5.3.2 Spectra near 183.3 GHz Obtained from Simulated Measurements
Made from Space

Looking down at the Tropical and Midlatitude atmospheres near 183 GHz, one would see spectra for the direct stratospheric cases as plotted in Fig. 40. The level of the
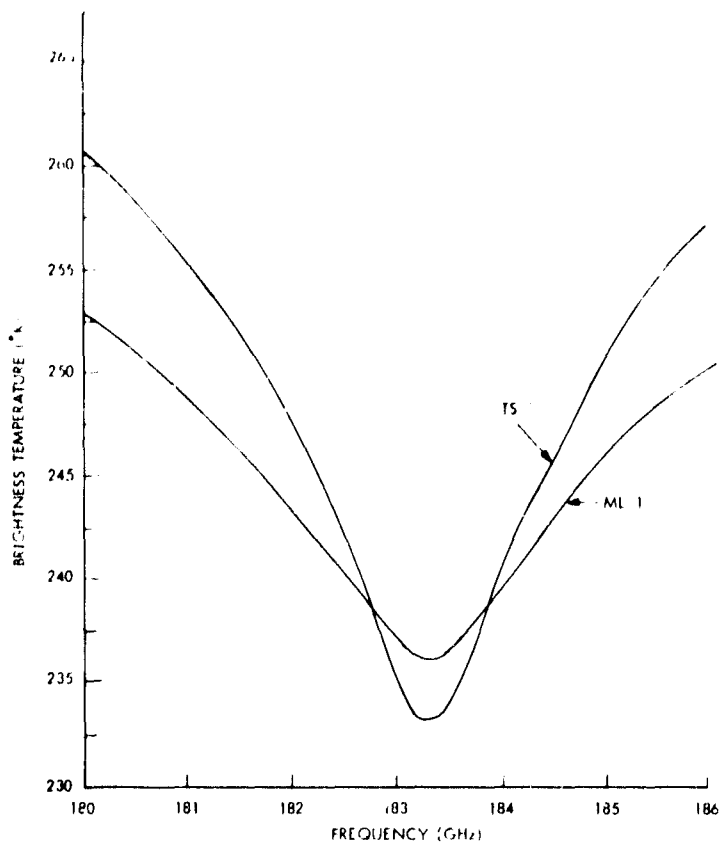
Fig. 40. Emission spectra from space near 183 GHz above a tropical and midlatitude atmosphere.

effective origin of the radiation rises as resonance is approached. For atmosphere ML1, on resonance, 90% of the radiation arises between the 4000-11,000-m levels; off-resonant frequencies see further into the atmosphere and therefore warmer effective temperatures. The Tropical atmosphere contains more moisture than the Midlatitude model; therefore, the effective origin of radiation is at higher and colder levels near resonance, which explains the deeper minimum.

The level of the effective origin of radiation at resonance continues to rise as the moisture concentration in the stratosphere increases. Eventually, with enough water vapor, the effective origin of radiation measured at a satellite moves above the tropopause and the atmospheric temperature, and, therefore, the brightness temperature measured at the satellite begins to increase. Superimposed on the minima of Fig. 40, near resonance, would be a secondary maximum. And even if more moisture is added to the stratosphere, the level of the effective origin of radiation that is being measured can move above the stratopause and into declining temperatures again in the mesosphere. Superimposed on the secondary maximum would now appear a spike pointing toward lower temperatures. Such a situation is shown in Fig. 41. The secondary maxima a few MHz off resonance are almost equal to the temperatures at the stratopause. The resonant

minima have begun to plunge toward the very low mesopause temperatures.

The obvious conclusion to be drawn is that measurements near the 183-GHz line offer a potentially powerful tool for exploring the amount and distribution of stratospheric
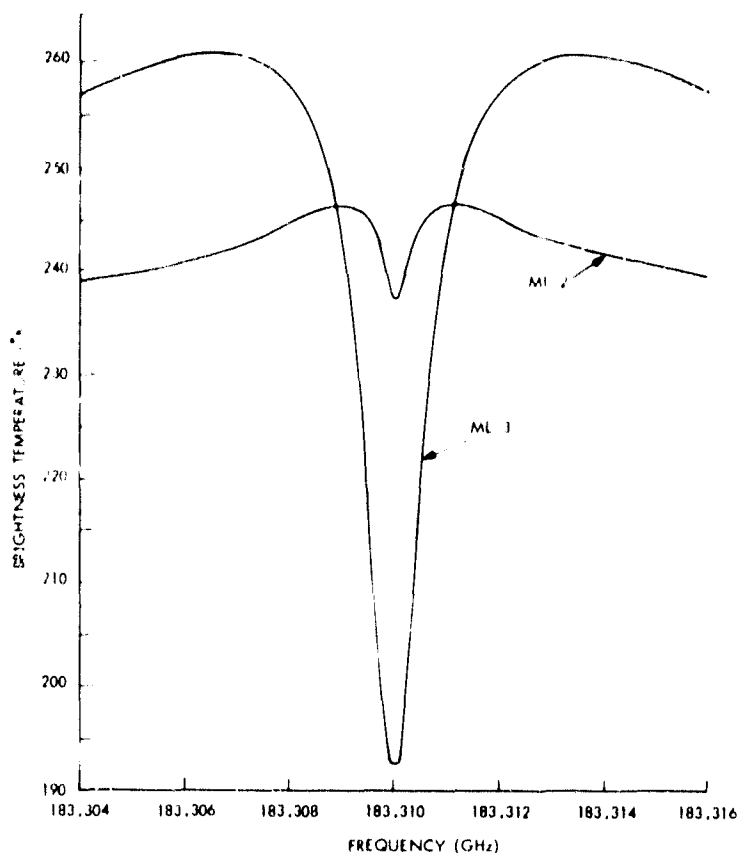
Fig. 41. Possible emission spectra seen from space near 183.310 GHz over moist stratospheres.

water vapor, given an approximate knowledge of the temperature distribution as a function of height. When radiometers are built with suitable bandwidths and noise factors, and with physical dimensions and weight that are adequate for satellites, they undoubtedly can be coupled with radiometers that monitor the spectrum in and near the complex of oxygen lines near 5 mm, and from which one can determine the temperature distribution in the stratosphere. Such a combination will be a very effective means of mapping, on a synoptic basis, the amount and distribution of stratospheric water vapor.

VI. INTEGRATED ATMOSPHERIC WATER VAPOR

As was shown in Section IV, solar attenuation measurements reveal significant day-to-day variations in the shape and intensity of the 1.35-cm water-vapor spectral line. Furthermore, these variations have been shown to arise from changes in the total amount and the vertical distribution of water vapor. A question naturally arising is: Given the spectral data, what important meteorological information for daily forecasting may be extracted from it? We shall explore the possibility that spectral measurements can give information about the vertically integrated atmospheric water-vapor content.

The problem can be approached from any of the sets of spectral measurements that were presented in Section III. Because there are existing data for total zenith opacity, however, the problem will be analyzed from the standpoint of such measurements.

6.1 STATEMENT OF THE PROBLEM

For any given set of atmospheric conditions, the total zenith opacity has been defined in Eq. 43 as

$$\tau_{max}(\nu) = \int_0^H \gamma_T(\nu, z) \, dz. \tag{80}$$

In Eq. 80, $\tau_{max}(\nu)$ is the attenuation that would be measured at the zenith, $\gamma_T(\nu, z)$ represents all of the mechanisms of attenuation and will depend upon the frequency and where the observer is located in the atmosphere. H, as before, is a height above the levels of significant attenuation.

If we restrict ourselves to a frequency region sufficiently close to the 1.35-cm rotational resonance of water vapor, γ_T may be conveniently broken down into several parts, each of which represents separate physical mechanisms of attenuation. This separation can be symbolically written

$$\gamma_T = \gamma_{RES} + \gamma_{NON} + \gamma_{O_2} + \gamma_R, \tag{81}$$

where γ_{RES} represents the attenuation that is due to the 1.35-cm resonance alone, γ_{NON} represents the attenuation from the wings of all higher frequency water-vapor lines, γ_{O_2} is the attenuation coefficient for oxygen (Appendix B), and γ_R represents the attenuation from all sources not specified above. In the analysis, it will be assumed that γ_R is negligible. On clear days, this is a safe assumption; on days with heavy clouds, however, γ_R can contribute significantly to γ_T.

Similarly to the breakdown of γ_T, τ_{max} may be thought of as consisting of separate contributions from each part of γ_T, so that we may write

$$\tau_{RES}(\nu) = \int_0^H \gamma_{RES}(\nu, z) \, dz, \tag{82}$$

60

where τ_{RES} is the zenith opacity arising from the 1.35-cm resonance alone. For the moment, let us assume that τ_{RES} can be determined from measurements of τ_{MAX}; our problem then becomes one of understanding how τ_{RES} is related to the integrated atmospheric water vapor.

The full equation of γ_{RES} is represented by Eq. 3. It may be conveniently expressed as

$$\gamma_{RES}(\nu, P, T, \rho) = C\rho\nu^2 f_1(T)\, S,\qquad(83)$$

where C is an appropriate constant, ρ is the density of water vapor, ν is the frequency of observation, $f_1(T)$ is given by

$$f_1(T) = \exp\left\{-\frac{644}{T}\right\} T^{-5/2},\qquad(84)$$

and S is a derivative from the line-shape factor. S is not perfectly known, but can be adequately approximated for our purposes from the van Vleck-Weisskopf expression (Eq. 14). When fully written out S is given by

$$S = \Delta\nu\left[\frac{1}{(\nu-\nu_o)^2 + \Delta\nu^2} + \frac{1}{(\nu+\nu_o)^2 + \Delta\nu^2}\right],\qquad(85)$$

in which ν_o is the resonant frequency for the transition (22.237 GHz) and $\Delta\nu$ is the half-width at half-maximum for the spectral line.

For pressures between approximately 1 atm (~1000 mb), and perhaps 1.5×10^{-3} mb, $\Delta\nu$ has been shown to be quite accurately approximated for the 1.35-cm line by

$$\Delta\nu_{1.35} = B\frac{P}{T^{0.625}}\left(1+\alpha_{1.35}\frac{\rho T}{P}\right),\qquad(86)$$

where B is an appropriate constant, P represents total atmospheric pressure in mb, T the kinetic temperature in degrees Kelvin, and ρ the water-vapor density in g/m^3. If we neglect the small contribution of ρ to $\Delta\nu$, it is apparent from the equations above and the discussion accompanying Fig. 10 that for homogeneous conditions, the line becomes narrower and more intense as the pressure is reduced. In the atmosphere, the pressure diminishes logarithmically with height and therefore the spectrum of τ_{H_2O} is composed of a complex combination of many different line shapes.

To overcome the problem of changing line shapes, it is desirable to formulate a solution that either does not depend upon $\Delta\nu$ at all or, at the very least, restricts its importance. One method, which is the one that will be investigated now, takes advantage of the properties of the zenith opacity-weighting functions.

6.2 TOTAL INTEGRATED ATMOSPHERIC WATER VAPOR BY THE METHOD OF COMPOSITE WEIGHTING FUNCTIONS

The discussion of water vapor weighting functions for various microwave measurements, in Section III, pointed out and illustrated the property of "sensitivity." That is, at a given frequency there exists a height at which a unit density of water vapor contributes most effectively toward increasing the value of the parameter that is being measured. From Fig. 8, the maximum sensitivity for 19.0 GHz occurred at the ground, for 21.9 GHz the maximum was near 16 km, and for 22.237 GHz the sensitivity was greatest at the top of the atmosphere.

For the purpose of measuring the total integrated water vapor, the ideal weighting function would be a constant with height. For such a weighting function, a given amount of water vapor at any altitude would produce an exactly similar effect on measuring apparatus at the ground; the parameter that is being measured would be directly proportional to the integrated water vapor.

An approximation to such an ideal weighting function may be constructed from a combination of real weighting functions by considering the following analysis.

Using the weighting-function notation, the total zenith opacity for a given set of atmospheric conditions is

$$\tau_{H_2O}(\nu) = \int_0^H \rho(z) \, W_\tau(\nu, z) \, dz. \tag{87}$$

We define a new function L which is given by

$$L(z) \equiv \int_0^\infty a(\nu) \, W_\tau(\nu, z) \, d\nu. \tag{88}$$

Furthermore, we choose the $a(\nu)$ such that

$$L(z) = \text{constant}. \tag{89}$$

Equation 87 can be rewritten, as a consequence, as

$$\int_0^\infty a(\nu) \, \tau(\nu) \, d\nu = \int_0^H \rho(z) \int_0^\infty a(\nu) \, W_\tau(\nu, z) \, d\nu dz$$

$$= L \int_0^H \rho(z) \, dz. \tag{90}$$

The integrated water vapor v can be separated out and written

$$v = \frac{\int_0^\infty a(\nu) \, \tau(\nu) \, d\nu}{L}. \tag{91}$$

Detailed consideration of the form of γ_{RES} shows that $a(\nu)$ and L exist and have the following proportionalities:

$$a(\nu) \sim \frac{1}{\nu^2} \tag{92}$$

$$L \sim f_1(\overline{T}) = \frac{\int_0^H \rho \exp\{-644/T\} \, T^{-5/2} \, dz}{\int_0^H \rho \, dz} \, . \tag{93}$$

The solution for v, by using (91), has introduced the possibility of approximating the integrated water vapor without becoming involved with the complexities introduced by changing line shapes with altitude.

This may be seen more clearly by restating the problem in terms of a set of discrete measurements of total zenith water-vapor opacity. Now, let $L(z)$ be written

$$L(z) = \sum_i a(\nu_i) \, W_\tau(\nu_i, z) \, \delta\nu_i, \tag{94}$$

where the $\delta\nu_i$ are small frequency intervals in which the average value of the weighting function is W_τ. Choose the a_i such that

$$\int_0^H \{L(z) - \overline{L}\}^2 \, dz \tag{95}$$

is a minimum, where

$$\overline{L} = \frac{\int_0^H L(z) \, dz}{H} \, . \tag{96}$$

Then the best approximation possible for the integrated water vapor, with only the set of i opacity measurements used, is given by

$$v = \frac{\sum_i a(\nu_i) \, \tau(\nu_i) \, \delta\nu_i}{L} \, . \tag{97}$$

The value of using Eq. 97 is that since the W_i are nearly constant over widely occurring atmospheric conditions, then the a_i and L will also be nearly constant. And also, a very important consideration is that the weighting functions include γ_{NON}; that is, the only separation that must be made after measuring τ_{max} is that between the oxygen and water-vapor contributions. The only task remaining is to find frequencies which best satisfy (95).

Several composite weighting functions $L(z)$ are presented in Fig. 42. They are constructed from combinations of weighting functions whose frequencies were those monitored for the observations reported in Section IV. Two of the curves in Fig. 42 (labeled

63

21.9 and 29.45) are for combinations of 21.9 GHz and 29.45 GHz weighting functions. The third curve (labeled 22.237, 23.5, and 29.45) was derived from the weighting functions at 22.237 GHz, 23.5 GHz, and 29.45 GHz. The first two composite weighting functions show considerable deviations from L in the critical first two kilometers of the atmosphere. Undoubtedly these can be improved by optimizing the two frequencies used in the synthesis.

The two-frequency curve which shows a deviation from L of approximately 5% in the first 4 to 5 kilometers was arrived at by using an exponential weighting function to emphasize the region of the atmosphere near the surface of the Earth where water vapor predominates. Expression (95) was modified in that case, so that

$$\int_0^H \{L(z) - \bar{L}\}\, e^{-z/H}\, dz \tag{98}$$

was minimized, where H_s is some adjustable scale height that can be used to determine the emphasis placed on the layers near the surface. In the examples of Fig. 42, H_s was 5 km. When (98) is used, then (96) must also be modified to read

$$\bar{L} = \frac{\int_0^H L(z)\, e^{-z/H_s}\, dz}{\int_0^H e^{-z/H_s}\, dz}. \tag{99}$$

The three-frequency curve in Fig. 42 deviates from $\bar{L}$ no more than 2% at any level. It represents a remarkably constant $L(z)$. It was also derived by emphasizing the lower regions of the atmosphere, but it is apparent that this was probably unnecessary.

The $a(\nu_i)$ from the weighted two-frequency curve in Fig. 42 and the $a(\nu_i)$ from the three-frequency curve were used on radiosonde absorption computations to determine
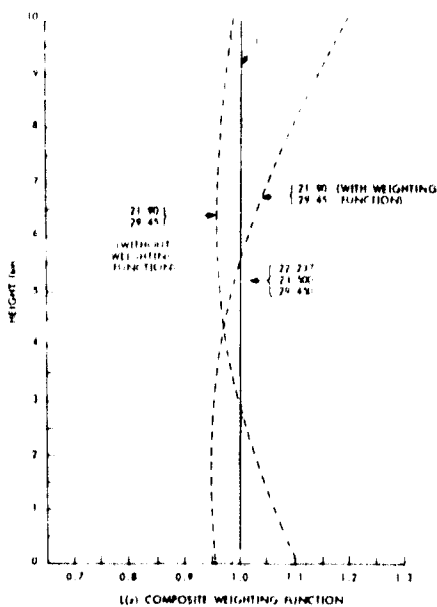
Fig. 42. Several composite weighting functions L(z).

Table 6. Comparison between the integrated water vapor as computed from Eq. 100, and the integrated water vapor actually observed by radiosondes. The bias when all observations are considered as one set is -0.039 g/cm^2, and the RMSE is 0.029 g/cm^2.

Date of Experiment	Integrated H$_2$O Radiosondes (g/cm^2)	Integrated H$_2$O 2-Frequency (g/cm^2)	
		Summer	
15 June 1965	1.564	1.563	
16	1.565	1.559	2-Frequency Case
21	2.771	2.688	
22	1.227	1.187	
1 July 1965	1.950	1.913	
8	2.881	2.799	
13	2.067	2.011	
14	3.016	2.892	RMSE = 0.036 g/cm^2
(M. I. T.) 15	2.775	2.706	
(AFCRL) 15	2.158	2.106	BIAS = -0.058 g/cm^2
19	1.644	1.607	
21	2.004	1.976	
22	2.107	2.071	
27	1.525	1.495	
28	2.344	2.291	
29	1.869	1.832	
3 August 1965	2.758	2.701	
5	1.886	1.834	
(1405) 10	4.241	4.118	
(1804) 10	3.908	3.804	
(2043) 10	3.280	3.200	
11	3.299	3.216	
12	2.405	2.333	
AVERAGES:	2.402	2.344	
		Winter	
10 Feb. 1966	1.752	1.743	
14	1.102	1.117	
17	0.318	0.321	
18	0.815	0.838	
23	0.631	0.652	RMSE = 0.016 g/cm^2
29	1.159	1.186	
3 March 1966	0.691	0.694	BIAS = $+0.001$ g/cm^2
4	3.540	3.539	
7	1.134	1.110	
10	0.845	0.816	
14	0.643	0.626	
AVERAGES:	1.148	1.149	

Table 7. Comparison between the integrated water vapor computed from Eq. 101, and the integrated water vapor actually observed by radiosondes. The bias when all observations are combined is +0.035 g/cm^2, and the RMSE is 0.020 g/cm^2.

	Date of Experiment	Integrated H_2O Radiosondes (g/cm^2)	Integrated H_2O 3-Frequency (g/cm^2)	
		Summer		
	15 June 1965	1.564	1.617	
	16	1.565	1.625	3-Frequency Case
	21	2.771	2.794	
	22	1.227	1.223	
	1 July 1965	1.950	1.984	
	8	2.881	2.908	
	13	2.067	2.078	
	14	3.016	3.013	
(M.I.T.)	15	2.775	2.798	
(AFCRL)	15	2.158	2.181	BIAS = +0.027 g/cm^2
	19	1.644	1.666	
	21	2.004	2.045	RMSE = 0.014
	22	2.107	2.135	
	27	1.525	1.547	
	28	2.344	2.378	
	29	1.869	1.904	
	3 August 1965	2.758	2.804	
	5	1.886	1.909	
(1405)	10	4.241	4.271	
(1804)	10	3.908	3.941	
(2043)	10	3.280	3.306	
	11	3.299	3.330	
	12	2.405	2.415	
	AVERAGES:	2.402	2.429	
		Winter		
	10 Feb. 1966	1.752	1.813	
	14	1.102	1.160	
	17	0.318	0.340	
	18	0.815	0.864	
	23	0.631	0.671	BIAS = +0.051
	29	1.159	1.219	
	3 March 1966	0.691	0.714	RMSE = 0.028 g/cm^2
	4	3.540	3.660	
	7	1.134	1.193	
	10	0.845	0.882	
	14	0.643	0.673	
	AVERAGES:	1.148	1.199	

how accurately integrated water vapor could be estimated if the spectral data were perfect. The results are listed in Tables 6 and 7.

The first table shows the results of using two frequencies only. The $a(\nu_i)$ for these two frequencies were found empirically and have the values

$$a(21.9) = 1.672 \text{ g/cm}^2 \text{ dB}^{-1}$$

$$a(29.45) = 6.015.$$

The equation giving the integrated water vapor, therefore, is

$$= 1.672 \cdot \tau(21.9) + 6.015 \cdot \tau(29.45) \text{ g/cm}^2, \tag{100}$$

where the τ's are in dB and the a's have been so adjusted that $\overline{L} = 16\nu$.

It will be noticed that all of the errors for the estimated summer integrated water vapor are low by an average of -2.3%, which is to be expected, since $L(z)$ for this case is less than $\overline{L}$ in the lowest 5 km. $L(z)$ is, however, low by approximately 5% in this region where most of the water vapor is and one must therefore draw the conclusion that the weighting functions that were used to construct $L(z)$ were proba'ly a few per cent lower than the average weighting functions of the summer atmospheres examined in Table 6 to explain some of the difference between -5% and -2.3%. This will be shown to be more likely when we investigate the three-frequency case. If all of the estimated integrated water-vapor values are increased by the magnitude of the bias, that is, 0.058 g/cm^2, then only three days' estimations would show errors greater than 1.0%. The same cannot be said of the winter two-frequency estimations. The error spread is from -3.4% to plus 3.3%, thereby reflecting the effect of colder temperatures on the weighting functions. For the entire set of data, including both winter and summer, the bias is seen to be -0.039 g/cm^2 and the rms error (RMSE) is 0.029 g/cm^2, approximately 1.5% of the average value for the integrated water vapor.

From these results, it is reasonable to expect that for two optimized frequencies and no adjustments of the $a(\nu_i)$ for temperature, accuracies within ±5% of the true value are obtainable year round in a climate such as Massachusetts exhibits. By using $a(\nu_i)$ adjusted for temperature, the accuracy can probably be increased to ±2%, with the average error approaching zero in each season.

The results for the three-frequency estimation are listed in Table 7. The $a(\nu_i)$ for this composite weighting function are

$$a(22.237) = 0.385 \text{ g/cm}^2 \text{ dB}^{-1}$$

$$a(23.5) = 2.161$$

$$a(29.45) = 4.322.$$

As in the case of the a's for the two-frequency $L(z)$, the constants above are adjusted

67

so that $\overline{L} = 16\nu$ and, therefore,

$$\nu = 0.385 \cdot \tau(22.235) + 2.161 \cdot \tau(23.5) + 4.322 \cdot \tau(29.45). \tag{101}$$

Surprisingly enough, despite the considerable improvement in the constancy of $L(z)$ for the three-frequency case, the summer estimates are not substantially better than the two-frequency estimates. If the bias of $+0.027$ g/cm^2 is removed, there are actually more days for which the error is greater than 1.0% than in the two-frequency summer results. The spread of the winter data, however, is considerably smaller than in the two-frequency winter results, even though a much stronger bias is evident. Without seasonal or temperature adjustments of the $a(\nu_i)$, there is no reason to expect better results over several seasons than with two frequencies. With seasonal adjustments only, some slight advantage probably lies with the three-frequency method. More statistics are necessary to properly decide how much better three-frequency observations are than two-frequency.

These results were quoted for perfect data, and errors reflect deviations of $L(z)$ from $\overline{L}$ and fluctuations in the weighting functions with varying atmospheric conditions. More error must be expected from imperfect spectral data.

Some general remarks are in order about the errors introduced by observational data. If obtaining optimum integrated water-vapor estimates is the only criterion upon which frequencies for observation are chosen, then they should be chosen to be as low in frequency as possible for two reasons: (i) the effects of clouds are diminished; and (ii) equipment is more reliable. For instance, the 19.0-GHz weighting function is very similar to the 29.45-GHz weighting function used in our experiments and would be a much wiser choice. This is especially true when one realizes that the same absolute errors in measuring τ_{max} are multiplied by some factor at the off-resonance frequencies, that is,

$$\frac{a(29.45 \text{ GHz})}{a(21.9 \text{ GHz})} \cong 4.$$

Three frequencies do help to alleviate the problem of having noisy data at one frequency. This redundancy will probably be the most important reason to have three rather than two frequencies for observations.

No attempt has been made to evaluate the integrated water vapor from the observations in Section IV, mainly because no standard of comparison exists for the results. But an error analysis can be done by using the quoted errors on observations to estimate the uncertainty of the integrated water-vapor estimates. If the integrated water vapor is given by

$$\nu = \sum a_i \tau_i, \tag{102}$$

then the error in ν can be approximated as

$$e(v) \cong \sum a_i e(\tau_i), \tag{103}$$

which gives the mean-square error for uncorrelated errors in the τ_i as

$$E[e^2(v)] = E\left[\left\{\sum a_i e(\tau_i)\right\}\left\{\sum_j a_j e(\tau_j)\right\}\right]$$

$$= E\left[\sum a_i^2 e^2(\tau_i)\right]$$

$$= \left\{\sum a_i^2 E\left[e^2(\tau_i)\right]\right\}, \tag{104}$$

where $E[\ ]$ is the expectation. This assumes no error in the a_i. For a day of good observing $e(\tau_i)$ can be expected to be near 0.01 dB on all channels. Therefore, for the two-frequency case, approximately

$$E\left[e^2(v_2)\right] = (1.67 \ 0.01)^2 + (6.015 \ 0.01)^2$$

$$= 0.00384$$

or the rms error can be expected to be near

$$\text{RMSE}(v_2) = 0.062 \ g/cm^2.$$

For a typical day, one might expect 2 g/cm^2 of integrated water vapor, so that the RMSE would be equivalent to approximately a 3% error.

For the three-frequency case

$$E\left[e^2(v_3)\right] = (0.385 \ 0.01)^2 + (2.161 \ 0.01)^2 + (4.322 \ 0.01)^2$$

$$= 23.498 \times 10^{-4}$$

or

$$\text{RMSE}(v_3) = 0.048 \ g/cm^2.$$

The three-frequency RMSE is equivalent to approximately 2.5% error on the basis of 2 g/cm^2 of integrated moisture. Both errors computed above are greater than those expected from variations in $L(z)$ and therefore constitute the limiting factor in the accuracy of this technique.

6.3 OXYGEN CONTRIBUTION TO τ_{max}

There still remains the separation of τ_{H_2O} from τ_{max} in order to evaluate v.

Following the example of Eq. 81, for any given set of atmospheric conditions, τ_{max}

69

may be broken up as follows:

$$\tau_{max} = \tau_{H_2O} + \tau_{O_2} + \tau_R. \tag{105}$$

As before, τ_R will be considered to be negligible. The contribution from τ_{O_2} is small but never negligible, and in some cases of extremely dry conditions (the Arctic, for instance) will exceed τ_{H_2O}. Similarly to Eq. 82, τ_{O_2} may be expressed as

$$\tau_{O_2} = \int_0^H \gamma_{O_2} \, dz. \tag{106}$$

γ_{O_2} may be conveniently expressed (see Appendix B for the full equation) as

$$\gamma_{O_2} = C_1 P T^{-3} \nu^2 \sum_n S_n e^{-E_n/kT}, \tag{107}$$

where γ_{O_2} is in dB/m if P is the total pressure in mb, T is the kinetic temperature in degrees Kelvin, ν is the frequency of the penetrating radiation in GHz, and C_1 is a constant equal to 2.015×10^{-3}, E_n is the energy in the same units as kT of the lower rotational state of a given transition, each of which is designated by n, and k is Boltzmann's constant. The summation is carried out over all transitions that link significantly populated energy states at atmospheric temperatures.

The meaning of the S_n is given in Appendix B. A common factor to all the terms of the S_n is the half-width (assumed to be the same for all transitions) $\Delta\nu_{O_2}$. Therefore, we can write

$$\sum_n S_n e^{-E_n/kT} = \Delta\nu_{O_2} \sum_n S'_n e^{-E_n/kT}, \tag{108}$$

where

$$\Delta\nu_{O_2} \cong C_2 P T^{-0.85}. \tag{109}$$

$\Delta\nu_{O_2}$ is given in GHz when C_2 is 7.75×10^{-2} GHz/mb, and P and T are in millibars and degrees Kelvin, respectively.

By removing the common factor of $\Delta\nu_{O_2}$, the S'_n in the region of 22 GHz are now almost independent of $\Delta\nu_{O_2}$. This follows from Eq. B.4, and the inequalities $\nu_n \geqslant 2\nu$ and $\nu_n \geqslant 7\Delta\nu_{O_2}$, where the ν_n are the resonant frequencies of the oxygen transitions. The summation remaining is a function of temperature through the Boltzmann term.

Figure 43 is presented to illustrate how the value of the summation from the right-hand side of Eq. 108 behaves as a function of temperature. It is very closely approximated by a linear function of T. Therefore, from Eq. 109 and the discussion above, (107) may be rewritten

$$\gamma'_{O_2}(\nu = constant) = C_3 P^2 T^{-3.85}\{C_4 + C_5 T\}, \tag{110}$$

where, for γ'_{O_2} in dB/m, C_3 is given by

$$C_3 = C_1 C_2 \nu^2 = 1.55 \times 10^{-4} \nu^2, \tag{111}$$

and ν is in GHz. At 19 GHz,

$$C_4 = 0.012$$

$$C_5 = 1.725 \times 10^{-3}.$$

Figure 44 gives a comparison of the computations of total zenith opacity attributable to oxygen by the full equation (107) to that from (110) for a number of radiosonde runs. The small systematic error of 0.0008 dB results from ignoring the pressure dependence of β from Eq. B.8.

Despite the simplifications of Eq. 110, we are in no better position to simply estimate the oxygen zenith opacity of the atmosphere. Certainly, if measurements of the vertical profile of temperature and pressure can be made in order to use (110), the water vapor can be measured also. The only convenient parameters that will be measurable at a radiometer site will be surface pressure and temperature. Therefore it will be necessary to use these as inputs to any scheme that estimates the contribution of τ_{O_2} to τ_{max}.

In order to produce such a scheme, several assumptions are necessary. First, we assume that all of the attenuation attributable to oxygen near 22.2 GHz occurs in the lowest 12 km of the atmosphere. This is reasonable for two reaons: (i) at the height of 12 km in the Standard Atmosphere 1962, the pressure is approximately 20% of the sea-level value. This introduces a factor of 1:5 for attenuation in regions above and below this level; (ii) the effective pressures in the two regions are approximately in the ratio of 1:4, thereby introducing another factor of 1:16 in the strength of γ_{O_2} above and below 12 km, because of its dependence on pressure squared. The two factors taken together represent roughly an effective attenuation in the two regions of approximately 1:80, with temperature effects disregarded.

Second, we assume that pressure decreases exponentially with altitude with a scale height of 8 km, that is,

$$P(z) = P_s e^{-z/H_p}, \tag{112}$$

71
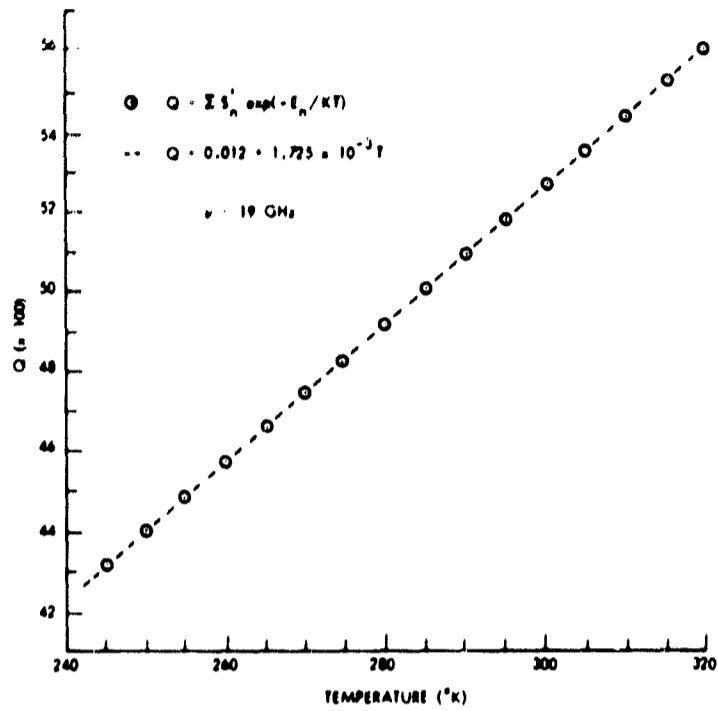
Fig. 43. Summation from γ_{O_2} and its approximation.
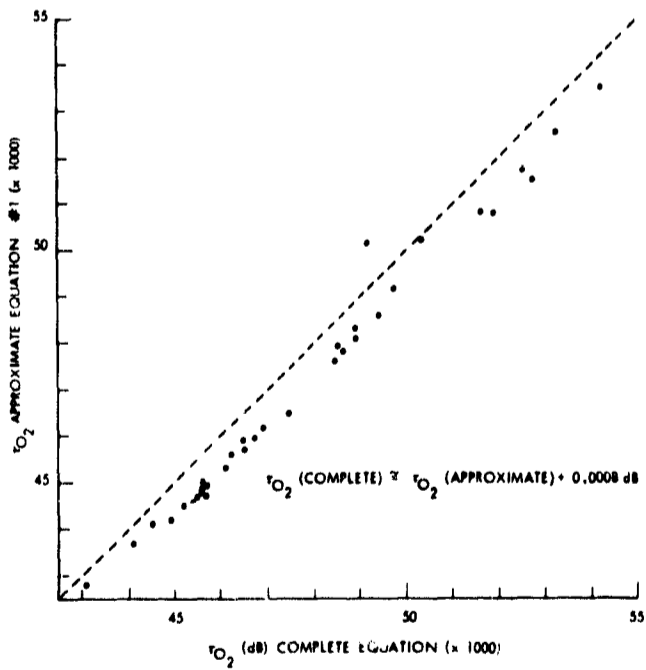
Fig. 44. First approximation to τ_{O_2}.

where $H_p = 8$ km, and P_s is the surface pressure. The average pressure over this region is approximately given by

$$\overline{P} = \frac{\int_0^{12} P_s e^{-z/H_p} dz}{\int_0^{12} dz} = \frac{H_p P_s}{12}\left(1 - e^{-12/H_p}\right)$$

$$\cong P_s/2. \tag{113}$$

The validity of the assumption of an exponential decrease in pressure is investigated in Fig. 45. The two radiosonde curves mark the extreme summer and winter profiles of pressure versus height. For the first four to six kilometers the approximation appears to be a good average of the extremes. At higher levels, the scale height changes, because of decreasing temperature, and the fit is not as good. Nevertheless, we shall retain the approximation at all levels.
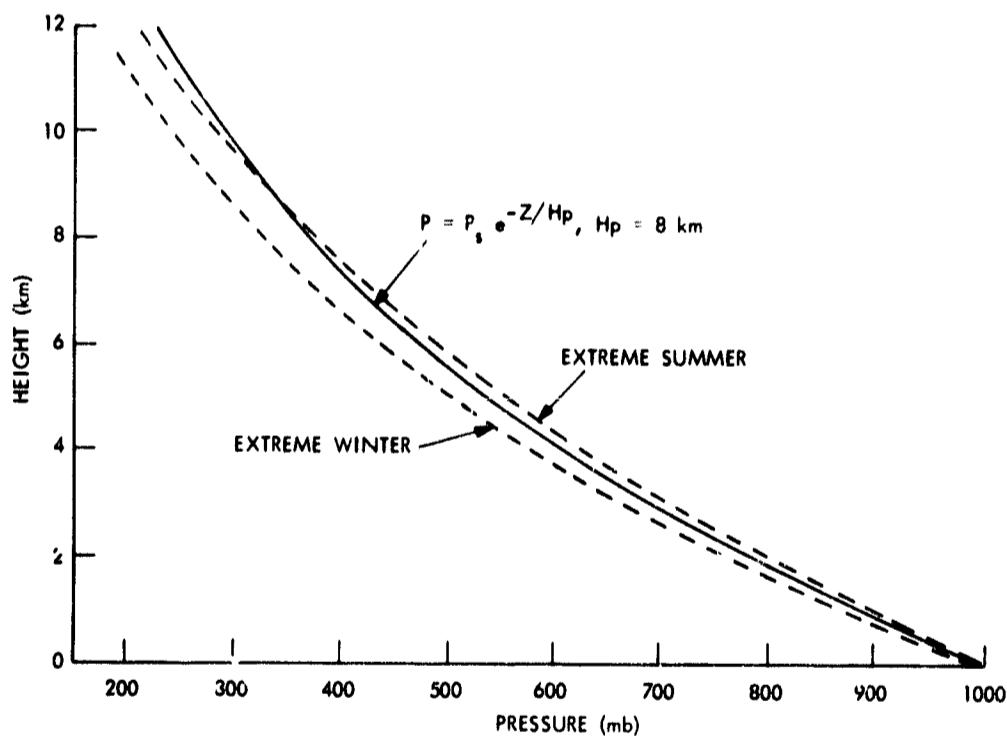
Fig. 45. Exponential approximation to the dependence of pressure with height.

The third approximation will be that the temperature decreases linearly with height at a rate near 6.5°K per km up to the 12-km limit. This is approximately true for mean atmospheric conditions. To establish an average temperature that is meaningful for Eq. 110, we must take into consideration that its importance is associated with the pressure squared.

If

$$T(z) = T_s + \eta z, \tag{114}$$

in which T_s is the surface temperature, η is the vertical gradient of the temperature equal approximately to $-6.5°K/km$, and $T(z)$ is the temperature at the height z, then a pressure squared weighted temperature is given by

$$\overline{T} = \frac{\int_0^{12} P_s^2 \, e^{-2z/H_p} \, (T_s+\eta z) \, dz}{\int_0^{12} P_s^2 \, e^{-2z/H_p} \, dz}$$

$$= T_s - b, \tag{115}$$

where $b = 22°K$ for an atmosphere whose vertical temperature gradient is $-6.5°K/km$.

If we substitute these average quantities for P and T in Eq. 110 and the result into (106), with the full realization that the averages ignore such possibilities as systematic correlations among themselves, deviations from the model, and are, therefore, only rough approximations to the real averages, we have a tentative approximation for the oxygen attenuation. It requires only that we know the pressure and temperature at the observation site. The general expression is

$$\tau_{O_2}(\nu = \text{const.}) = \left\{ \gamma'_{O_2}(\overline{P}, \overline{T}) \right\} \cdot h \tag{116}$$

$$= \left\{ C_3 \frac{P_s^2}{a^2} (T_s - b)^{-f} [C_4 + C_5 (T_s - b)] \right\} \cdot 12 \times 10^3 \text{ dB.} \tag{117}$$

τ_{O_2} at 19 GHz is in dB when $C_3 = 5.60 \times 10^{-2}$, and C_4 and C_5 are the same as before. The constants a, b, and f, from our previous analysis, are approximately equal numerically to 2, 22°K, and 3.85, respectively.

Empirical values of a, b, and f were found that produced the best over-all correlation between the approximate τ_{O_2} calculated from Eq. 117, and the full equation from Appendix B for the 34 radiosonde runs reported in Section IV. The results showed that it was necessary to change the temperature exponent from 3.85 to a lower value. This changed the value of C_3 considerably. The final approximate equation, valid only at a given frequency ν, can be written

$$\tau_{O_2}(\nu = \text{const.}) \cong C_6 P_s^2 (T_s - b)^{-f} [C_4 + C_5 (T_s - b)]. \tag{118}$$

In (118), C_6 incorporates the constants C_3 and a, and the integration height of 12×10^3 meters from (117). For $\nu = 19$ GHz and τ_{O_2} in dB, with pressure given in mb, temperature in degrees Kelvin, the various constants have the following values:

74

$$C_4 = 0.012$$

$$C_5 = 1.725 \times 10^{-3}$$

$$C_6 = 6.7 \times 10^{-2} \qquad \left. \right\} 19 \text{ GHz}$$

$$b = 21°K$$

$$f = 2.40$$

A comparison between τ_{O_2} as calculated from Eq. 118 and the full equations in
Appendix B is shown in Fig. 46. The maximum deviation between the approximated
and nonapproximated values is 2.4×10^{-3} dB for all of the summer and winter radio-
sondes reported in Section IV. The rms error is approximately 1×10^{-3} dB. The mean
value of τ_{O_2} is approximately 50×10^{-3} dB, so that a mean error of approximately 2% can
be expected from using Eq. 118 around the Boston area. For other regions, C_6, b, and
f will no doubt need to be optimized again.
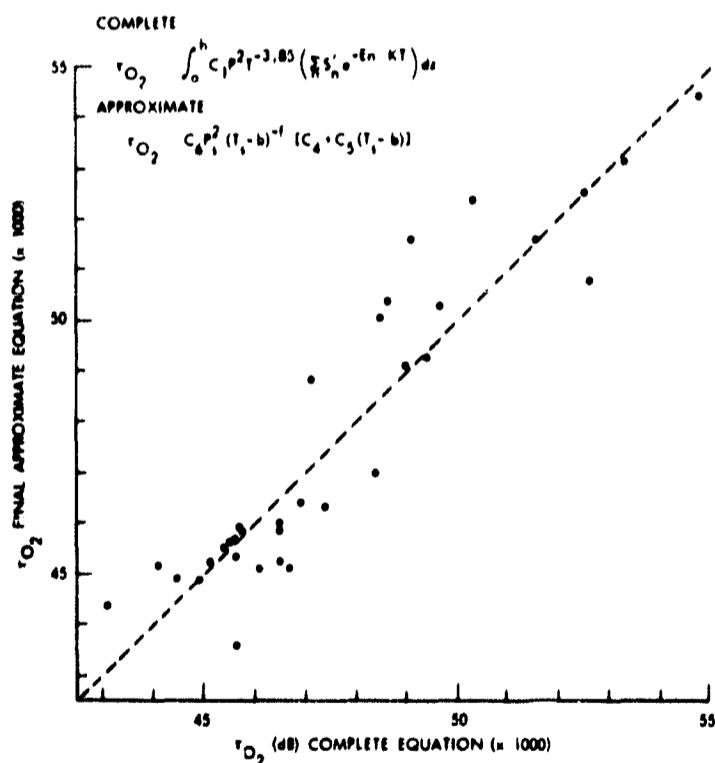
Fig. 46. Comparison of τ_{O_2} as computed from the final approximate
equation and τ_{O_2} computed from the full equation.

The decrease in the temperature exponent f from 3.85 in Eq. 110 to 2.40 in (118)
can be attributed to systematic correlations between surface temperature and (i) the
pressure scale height, (ii) the vertical lapse rate of temperature, and (iii) the optimum

75

surface temperature. (The author's thesis gives details of these correlations.[47])

Equation 118, with the values of the constants quoted, is valid at 19 GHz only. To extend it to values through 32 GHz, the following empirical formula is accurate within 0.001 dB:

$$\tau_{O_2}(\nu) = \tau_{O_2}(\nu = 19 \text{ GHz}) \left\{ 2.229 - 2.715\left(\frac{\nu}{19}\right) + 1.486\left(\frac{\nu}{19}\right)^2 \right\}, \tag{119}$$

where the frequency ν is in GHz.

VII. ABUNDANCE AND VERTICAL DISTRIBUTION OF WATER VAPOR FROM TOTAL ZENITH OPACITY SPECTRAL MEASUREMENTS NEAR 22.2 GHz

Before the full potentialities of satellites in meteorological surveillance can be realized, satisfactory schemes must be perfected to relate the radiation data that a satellite might obtain to the parameters that are of interest to the meteorologist.

A great deal of work on inversion schemes has already been done. Geophysical quantities that appear to be recoverable from radiation data are atmospheric temperature,[48-54] the amount and vertical distribution of ozone,[55] the amount and vertical distribution of water vapor,[39, 56-58] the spatial extent and liquid water content of clouds,[56, 59] surface temperature,[57, 60] sea "state",[61] the thickness of constant pressure difference layers,[51, 62] and the existence of trace gases.[63]

Thus far, information about atmospheric water vapor recovered from satellites has come from work done, for the most part, in the infrared, primarily because for a long time instrumentation has been available which is simple and compact and hence suitable for satellite packaging.

The use of the infrared spectral region for studying atmospheric water vapor is subject to a serious limitation, however, which is imposed by clouds. Even thin clouds are opaque to infrared radiation and restrict the region of the troposphere which is to be explored by infrared sensors. Analysis of hemispheric pictures of the Earth taken from space for percentage of cloud cover has revealed how much of a handicap this is.

The microwave region of the spectrum, on the other hand, has the advantage of spanning a zone of frequencies within which clouds at the lower frequencies are essentially transparent, and at the higher frequencies opaque. Below approximately 30 GHz (1 cm) clouds rapidly lose the ability to absorb and scatter radiation; at higher frequencies they rapidly become opaque. Quite fortuitously, the water-vapor resonance of lowest frequency is centered near 1.35 cm, and therefore is little affected by ordinary cloud cover.

This circumstance has led naturally to the suggestion that microwave radiometry should eventually be the most useful tool for determining information about atmospheric water vapor from satellites. Probably this is true, but a satisfactory inversion scheme must be perfected to relate the measurements to the water-vapor distribution. Several problems, besides those inherent in the mathematical inversion process, must be solved. For instance, there are the problems of background radiation and clouds, both of which must be properly handled if accurate water-vapor information is to be extracted from observations.

The problem of background radiation has been touched upon in Section III. The problem of clouds has been studied by Staelin.[56] He has shown that the weighting functions for certain frequencies above and below the 22.2 GHz resonance are almost identical in the absence of clouds; however, the spectral effect of clouds is proportional to $1/\lambda^2$.

Therefore measurements that would otherwise be similar at the two frequencies are modified in the presence of clouds. The modifications contain information about the clouds which may be used to correct the spectral data.

Of the types of microwave measurements presented in Section III, the satellite measurements, for the reasons just given, will be the most difficult to invert for information about atmospheric water vapor. The surface-based measurements of the brightness temperature spectrum will be the next most difficult to invert. There is not the comp: question of a variable background to contend with, but these measurements are inherently nonlinear, because of the role of temperature in the absorption coefficient and in the source function. The brightness temperature can never exceed the temperature of the atmosphere; therefore, as the water-vapor abundance increases, the brightness temperature near the center of the line at first will increase approximately linearly, then asymptotically approach the kinetic temperature of the atmospheric water vapor. The brightness temperature observed at frequencies in the wings of the line, however, will seldom depart from a linear relationship with water vapor. The result is a nonlinear spectrum.

The simplest of the measurements discussed in Section III to invert must be the zenith opacity measurements; they are very nearly linear in water-vapor density at the concentrations found in the atmosphere. Despite the relative simplicity of making them, they retain many of the difficulties and problems which must be overcome if any set of spectral measurements is to be inverted for the vertical distribution of water vapor. Therefore, the problem of the inversion of opacity measurements has been chosen as the subject of investigation here.

7.1 THE OPTIMUM LINEAR ESTIMATOR

The scheme outlined below was suggested by Rodgers[51] for handling the problem of inverting infrared spectral data to yield a profile of the atmospheric temperature. A similar scheme has been proposed and investigated by Westwater and Strand.[64]

Recall the shape of the zenith opacity weighting functions. Certain frequencies are more sensitive to water vapor at a given height than other frequencies. That is, if the water vapor is increased, say, at 16 km, the opacity measured on the ground at 21.9 GHz will be relatively strongly affected, whereas the opacity measurement at 19.0 GHz will be relatively weakly affected. If, on the basis of measurements at these two frequencies alone, we were forced to choose a water-vapor distribution, the choice at 16 km would naturally depend more heavily on the 21.9-GHz measurement. At levels near the surface, we would be most likely to rely just as heavily on both frequencies. Using the same reasoning and utilizing the quasi-linear nature of γ_{H_2O} with respect to water-vapor density, we can write for any given level z_i in the atmosphere a best estimate of the water vapor at that level based upon measurements of zenith opacity at j frequencies at the ground; that is,

$$\rho_i^* = \sum_j D_{ij} d_j. \tag{120}$$

where ρ_i^* is the estimated mean density in the ith layer in the atmosphere, the d_j are the opacity measurements, and D_{ij} is some linear operator that transforms the spectral data to an estimate of water vapor. The D_{ij} change with height not only because ρ diminishes with height but also because the sensitivity of the various frequencies changes with height. In full matrix form Eq. 120 becomes

$$\underline{\rho}^* = \underline{\underline{D}}\,\underline{d}. \tag{121}$$

Equation 120 as it stands does not provide a unique solution for the ρ_i^* because for every set of d_j opacity measurements there exists an infinite manifold of water-vapor distributions which would produce those measurements. What is needed is a condition on the D_{ij} which defines the optimum estimate of the water-vapor distribution, given a set of spectral measurements d_j. A logical condition that suggests itself is to choose the D_{ij} in such a manner that the most probable water-vapor distribution that will produce a given set of d_j's is estimated. This condition can be written symbolically as the minimization of the statistical mean-square error; that is, the minimization of the expression

$$E[(\underline{\rho}^*-\underline{\rho})^T(\underline{\rho}^*-\underline{\rho})] = E[\underline{\underline{Q}}], \tag{122}$$

where the once underlined quantities are column vectors, the symbol E represents the expected value or statistical average of the square-bracketed quantity, the superscript T stands for a matrix transpose, and ρ_i^* and ρ_i are the estimated and real water-vapor densities in the ith layer in the atmosphere for a given radiosonde.

In order to utilize the condition established in expression (123), rewrite $\underline{\rho}^*$ in terms of the matrix $\underline{\underline{D}}$ (double underlining identifies a matrix) and the data vector $\underline{d}$:

$$\underline{\underline{Q}} = [\underline{d}^T\underline{\underline{D}}^T\underline{\underline{D}}\,\underline{d}-\underline{\rho}^T\underline{\underline{D}}\,\underline{d}-\underline{d}^T\underline{\underline{D}}^T\underline{\rho}+\underline{\rho}^T\underline{\rho}]. \tag{123}$$

The condition for minimization becomes

$$\frac{\partial E[\underline{\underline{Q}}]}{\partial D_{ij}} = 0. \tag{124}$$

The result for any given ij is

$$0 = E\left[d_j\underline{\underline{D}}\,\underline{d}+\underline{d}^T\underline{\underline{D}}^Td_j-\rho_jd_i-d_i\rho_j\right] \tag{125}$$

which can be restored to full matrix notation as

$$\underline{0} = E[\underline{\underline{D}}\,\underline{d}\,\underline{d}^T-\underline{\rho}\,\underline{d}^T]. \tag{126}$$

For the equality to be satisfied (126) requires

$$\underline{\underline{D}}E[\underline{d}\,\underline{d}^T] = E[\underline{\rho}\,\underline{d}^T].$$ (127)

$\underline{\underline{D}}$ is not a random variable and therefore has been placed outside the statistical-average brackets. If we define a data correlation matrix $\underline{\underline{C}}_d$ such that

$$\underline{\underline{C}}_d = E[\underline{d}\,\underline{d}^T],$$ (128)

then a formal solution to the operator $\underline{\underline{D}}$ may be written

$$\underline{\underline{D}} = E[\underline{\rho}\,\underline{d}^T]\,\underline{\underline{C}}_d^{-1}.$$ (129)

A straightforward method of evaluating the right-hand side of (129) would simply be to monitor simultaneously the spectral features of the atmosphere and its water-vapor distribution in some suitable manner to establish the statistical averages of the required correlations. This would not require any theoretical knowledge of the atmosphere-spectral data relationship, but in most cases would be a costly and time-consuming endeavor.

Another method that would eliminate the necessity of the simultaneous radiometer measurements would be to rely on the known relationship between atmospheric conditions and the spectral data to establish the needed correlations in (129). Old radiosonde data would be as usable as new data to establish approximations to the statistical averages. Further simplification ensues if the quasi-stationary nature of the weighting functions is utilized. For that case a noiseless data vector can be written

$$\underline{d}_o = \underline{\underline{W}}\,\underline{\rho},$$ (130)

where $\underline{\underline{W}}$ is composed of elements W_{ij} which are average values of the weighting function at a given frequency, ν_j, over a vertical interval in which the average water-vapor density is ρ_i, multiplied by that vertical interval Δz_i.

The total noisy data vector can be written

$$\underline{d} = \underline{d}_o + \underline{n},$$ (131)

where the n_j are the expected noise levels in each radiometer channel. The data-correlation matrix becomes

$$\underline{\underline{C}}_d = E[\underline{d}\,\underline{d}^t] = E\left[(\underline{d}_o+\underline{n})(\underline{d}_o+\underline{n})^t\right]$$

$$= E\left[\underline{d}_o\underline{d}_o^t + 2\underline{n}\,\underline{d}_o^t + \underline{n}\,\underline{n}\right]$$ (132)

If there is no correlation between noise and data, then (131) reduces to

$$\underline{\underline{C}}_d = E\left[\underline{d}_o\underline{d}_o^t\right] + E[\underline{n}\,\underline{n}^t] = \underline{\underline{C}}_o + \underline{\underline{C}}_n,$$ (133)

in which $\underline{\underline{C}}_o$ and $\underline{\underline{C}}_n$ are the noiseless data-correlation matrix and the noise correlation

80

matrix, respectively. If the noise is uncorrelated from channel to channel, then

$$\underline{\underline{C}}_n = [n_r n_s \delta_{rs}],$$ (134)

where δ_{rs} is the Kronecker delta.

By using Eq. 129, $\underline{\underline{C}}_o$ may be written

$$\underline{\underline{C}}_o = E\left[\underline{d}_o \underline{d}_o^t\right] = E[\underline{\underline{W}} \underline{\rho} \underline{\rho}^T \underline{\underline{W}}]$$

$$= \underline{\underline{W}} E[\underline{\rho} \underline{\rho}^T] \underline{\underline{W}} = \underline{\underline{W}} \underline{\underline{C}}_\rho \underline{\underline{W}},$$ (135)

where a water-vapor correlation matrix $\underline{\underline{C}}_\rho$ has been implicitly defined.

Finally, the statistical average of the water-vapor data correlation required in Eq. 129 may be found from radiosonde data alone by making the substitution

$$E[\underline{\rho} \, \underline{d}^T] = E\left[\underline{\rho}(\underline{d}_o + \underline{n})^T\right]$$

$$= E[\underline{\rho} \underline{\rho}^T \underline{\underline{W}} + \underline{\rho} \underline{n}^T]$$

$$= \underline{\underline{C}}_\rho \underline{\underline{W}}.$$ (136)

The last expression results if there is no correlation between the water-vapor distribution and the noise in the measurements.

If we draw everything together, the solution of $\underline{\underline{D}}$ may be rewritten

$$\underline{\underline{D}}^T = (\underline{\underline{C}}_o + \underline{\underline{C}}_n)^{-1} \underline{\underline{W}} \underline{\underline{C}}_\rho$$ (137)

where $\underline{\underline{C}}_n$, $\underline{\underline{C}}_o$, $\underline{\underline{W}}$, and $\underline{\underline{C}}_\rho$ are defined in Eqs. 134, 135, 130, and 135, respectively.

The form of the estimation equation for water vapor and the solution for the linear operator $\underline{\underline{D}}$ as exemplified by Eqs. 121 and 129 are optimum in the case of noiseless data. By inspection of Eqs. 134 and 137, it is clear, however, that when noise is expected the formulation is not optimum. To see this, consider the following argument.

The matrix that must be inverted in (137) is given by

$$\underline{\underline{A}}^{-1} = [\underline{\underline{C}}_o + \underline{\underline{C}}_n]^{-1}.$$ (138)

$\underline{\underline{A}}^{-1}$ will approach zero as the expected noise approaches infinity. That is, $\underline{\underline{D}}^T$ will be predicted to have no information as the noise overwhelms the measured data. In the face of excessive noise, this requires that $\underline{\rho}^* \rightarrow \underline{0}$, the null vector. But it is quite obvious for this extreme case that the best estimate will be the mean water-vapor profile, $\underline{\rho}_M$.

To correct for this inconsistency, the original prediction equation can be modified to read

$$\Delta \underline{\rho}^* = \underline{\underline{D}}' \underline{\Delta d} \tag{139}$$

$$\underline{\rho}^* = \underline{\Delta \rho}^* + \underline{\rho}_{M'} \tag{140}$$

which then returns no information about the deviation from the mean profile in the case of excessive noise, leaving the best guess for this condition $\underline{\rho}_{M'}$ as it should be. Staelin[65] has shown that an equivalent formulation to the two equations (139) and (140) is

$$\underline{\rho}^* = \underline{\underline{D}} \, \underline{d}, \tag{141}$$

where $\underline{d}$ is now defined as

$$\underline{d} = [1, d_1, d_2, \ldots]^T, \tag{142}$$

and $\underline{n}$ is defined as

$$\underline{n} = [0, n_1, n_2, \ldots]^T. \tag{143}$$

Equations 141, 142, and 143, together with the definition of $\underline{\underline{D}}$ given in Eq. 137 will be known as the Optimum Linear Estimator (OLE).

7.2 EXTENSION OF THE THEORY FOR THE OPTIMUM LINEAR ESTIMATOR

The statistical form of the OLE as expressed in Eqs. 141 and 129 is quite general. Any parameter may be substituted for ρ and any set of data, homogeneous or heterogeneous, may be substituted for $\underline{d}$. In fact, in cases in which the relationship between some predictor and vector p and the measured quantities $\underline{m}$ used in a predictor vector is nonlinear, the general expression of Eq. 120 is still valid. Now, however, it can be written, following Staelin and Waters[67] and Staelin,[66] as

$$p_i^* = \sum_{j=1}^{N} D_{A_{ij}} \phi_j(\underline{d}), \tag{144}$$

where $\underline{p}^*$ remains the parameter of interest to be estimated, and $\underline{\phi}(\underline{d})$ is now a derivative of the original data vector $\underline{d}$. No restrictions are imposed on ϕ. In practice, however, for inversion of spectral data, it is composed of higher order terms, and cross terms from the original data vector $\underline{d}$. $\underline{\underline{D}}_A$ is the augmented linear operator.

If Eq. 144 is employed, then the solution for $\underline{\underline{D}}_A$ is given by

$$\underline{\underline{D}}_A = \underline{\underline{C}}(\underline{p}, \underline{\phi}) \cdot \underline{\underline{C}}^{-1}(\underline{\phi}, \underline{\phi}), \tag{145}$$

where the correlation matrices are defined as

$$C_{ij}(\underline{x}, \underline{y}) = E[x_i y_i]. \tag{146}$$

If one includes noise in the formulation as before, that is, $\underline{d} = \underline{d}_o + \underline{n}$, then the correlations are given in complete form as

$$C_{ij}(\underline{p}, \underline{\phi}) = C_{ij}\{\underline{p}, \underline{\phi}(\underline{d}_o)\} + \sum_{k=1}^{\infty} \frac{1}{k!} E\left[p_i (\underline{n} \cdot \nabla_d)^k \phi_j(\underline{d}_o) \right]_{d=d_o} \tag{147}$$

and

$$C_{ij}(\phi, \phi) = C_{ij}[\underline{\phi}(d_o), \underline{\phi}(d_o)] + \sum_{k=1}^{\infty} \frac{1}{k!} E\left[(\underline{n} \cdot \nabla_d)^k \phi_i(\underline{d}) \phi_j(\underline{d}) \right]_{d=d}, \tag{148}$$

where the ∇_d operator operates in d space.

The problem that the matrix $\underline{\underline{C}}(\phi, \phi)$ is singular can arise. This frequently occurs when many semi-independent data points are combined to form $\underline{d}$, from which the augmented data vector $\underline{\phi}(\underline{d})$ is constructed. When this matrix is singular, it has no inverse and $\underline{\underline{D}}_A$ has no solution. Waters and Staelin[66] have shown that an effective means of circumventing this problem is, first, to diagonalize the matrix $\underline{\underline{C}}(\phi, \phi)$ by choosing a new augmented data vector $\underline{\phi}'$ derivable from the original $\underline{\phi}$ by standard matrix operations. Those elements of $\underline{\phi}'$ having values less than the computational errors are then discarded. Finally, a new equation for the estimation of $\underline{p}^*$ is written which uses the restricted vector $\underline{\phi}'_A$. The final solution is given by

$$\underline{p}^* = \left\{ \underline{\underline{C}}(\underline{p}, \underline{\phi}'_A) \cdot \underline{\underline{C}}^{-1}(\underline{\phi}'_A, \underline{\phi}'_A) \right\} \cdot \underline{\phi}'_A(\underline{d}). \tag{149}$$

Waters and Staelin have successfully used this technique to estimate the vertical temperature profile of the atmosphere using synthetic brightness-temperature data. The problem of using brightness temperature to infer atmospheric temperature is slightly nonlinear. For spectral measurements taken in the 0.5-cm region the proper use of Eq. 149 in place of the analogue to (141) gives superior results.

7.3 IMPLEMENTATION OF THE OPTIMUM LINEAR ESTIMATOR AND RESULTS

Because attenuation data taken near the water vapor resonance near 1.35 cm is highly linear with respect to the total water vapor; that is, if one doubles the water-vapor content in every layer, the measured values of τ_{max} will very nearly double, Eqs. 141 and 137 will be adequate for exploring the properties of the OLE.

Several important features of the OLE are the following. (i) Data need not be only radiometer data; it can be anything that is correlated in some manner with the distribution of water vapor. (ii) No relationship between the number of data points and the

83

number of estimation levels is implied.

The first feature has been utilized for the results that will be presented by using the measured surface water-vapor density as a data point. This would normally be easily measured and is certainly an important piece of information in the estimation of the water-vapor profile.

The second feature is helpful in easily establishing the optimum number of data channels to use.

The proper evaluation of the expected values of the various correlations that constitute part of the solution to $\underline{\underline{D}}$ require an infinite number of atmospheric soundings. For the ensuing analysis only 34 atmospheric soundings were used to establish the statistics for the inversion procedure. It is undoubtedly a sample that is large enough only to portray the broadest characteristics of the OLE.

Most of the atmospheric water vapor is in the lowest two or three kilometers of the troposphere, and therefore we have extended our predicted values of ρ to only 10 km. The water-vapor estimates are the average values over 1-km slabs plus sometimes the surface value. Therefore the index i runs normally from 1 to 10, or 1 to 11.

The number of data channels is varied from one to three. For illustration, if 5 channels are used and 10 layers, then the size of the various matrices would be the following:

$$\underline{d}: \quad 3 \times 1$$

$$\underline{\rho}: \quad 10 \times 1$$

$$\underline{\underline{D}}: \quad 10 \times 5$$

$$\underline{\underline{C}}: \quad 10 \times 11$$

$$\underline{\underline{C}}_o, \underline{\underline{C}}_n: \quad 3 \times 3$$

$$\underline{\underline{W}}: \quad 3 \times 10.$$

The weighting functions used throughout the analysis are averages of the weighting functions for all of the days with radiosonde data in a given season. In Fig. 47, these average values are plotted. For the summer data, information, for the most part, from channels at frequencies of 21.9 GHz, 23.5 GHz, and 29.45 GHz were used. They appear as solid curves in Fig. 47. For the winter data, for the most part, information from channels at frequencies of 19.0 GHz, 22.235 GHz, and 23.5 GHz were used. They appear as dashed lines in Fig. 47. The summer-to-winter variation in the 23.5-GHz weighting function may be noted; also note the close similarity between the 19.0-GHz and 29.45-GHz weighting functions.

Several parameters can be varied in the OLE scheme: amount of expected noise; number of data channels; and atmospheric statistics. We shall investigate the
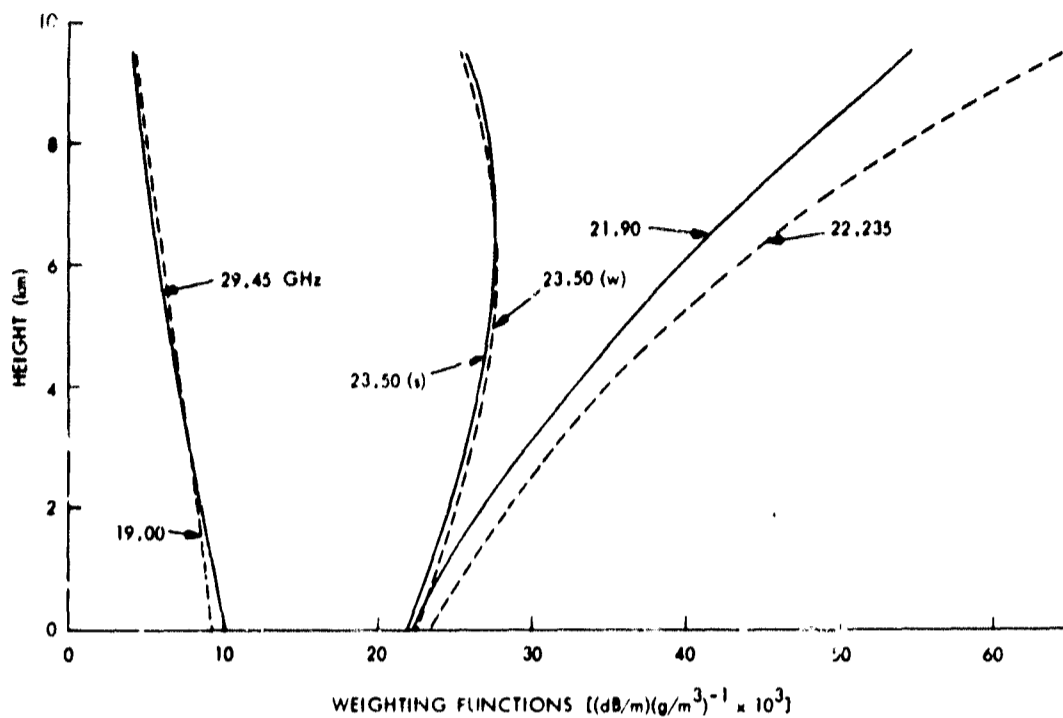
Fig. 47. Average weighting functions computed for use in the
Optimum Linear Estimator.

effects of varying each of these parameters. Finally, several days of real data from
the observations reported in Section IV will be inverted and analyzed.

7.3.1 Effects of Expected Noise on the Results of the
Optimum Linear Estimator

Data recovered from atmospheric spectral observations are never perfect. Even
if the atmosphere were perfectly stratified and unchanging in time, random noise would
still be introduced by the radiometer. Therefore it is of utmost importance to know
how any inversion scheme reacts to the inevitable errors that will be introduced.

The OLE considers noise as a quasi-weighting function for the data received. If
the scheme expects no noise, then the inversion will use the data to produce the most
detailed estimate of the water-vapor distribution of which it is capable. If noise is
expected in the data, the OLE treats the data more skeptically, relying more on the
mean statistics of the atmosphere contained in $\underline{\underline{C}}_\rho$.

To illustrate the effect of expected noise on the $\underline{\underline{D}}$ operator, consider Figs. 48 and
49. Figure 48 is a plot of the $\underline{\underline{D}}$ matrix when no noise is expected. At any level, it
is evident that the differences among values containing large numerical factors will
determine the estimated value of the water vapor. Small errors in any one channel will
cause large variations in these estimates.

In Fig. 49, the $\underline{\underline{D}}$ matrix has been calculated under the assumption that the statisti-
cal average of the random noise in each channel is 0.005 dB. Notice the drastic reduc-
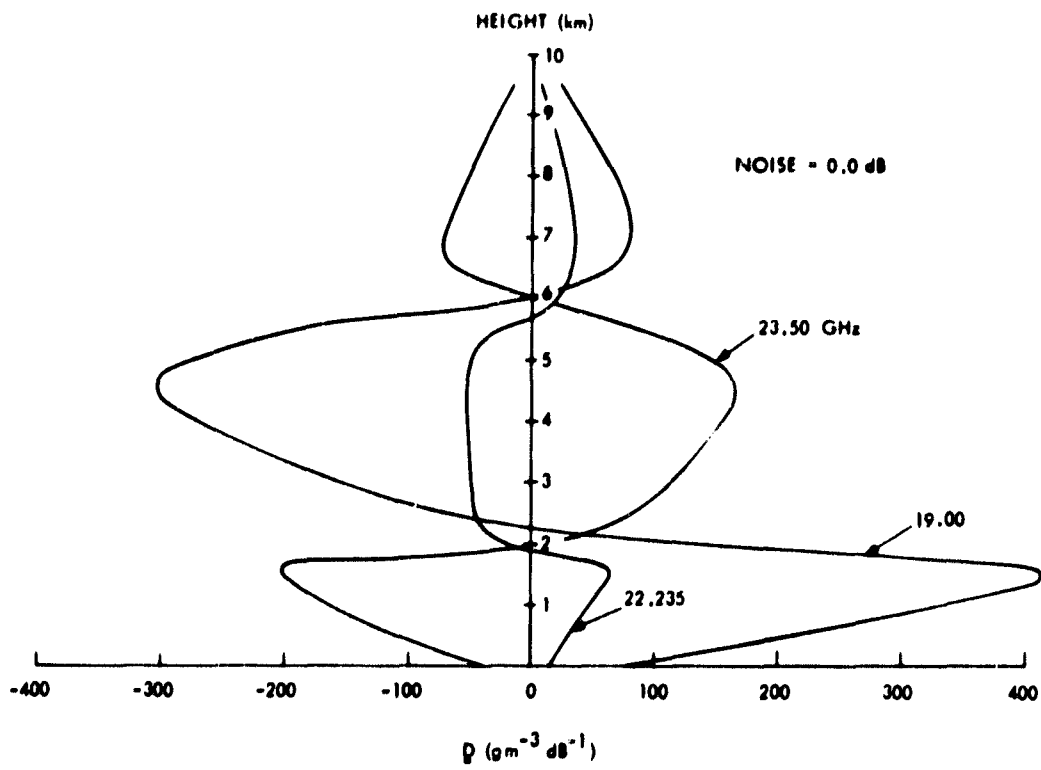tion in the abscissa scale. The expectation of a little noise has stabilized the solution

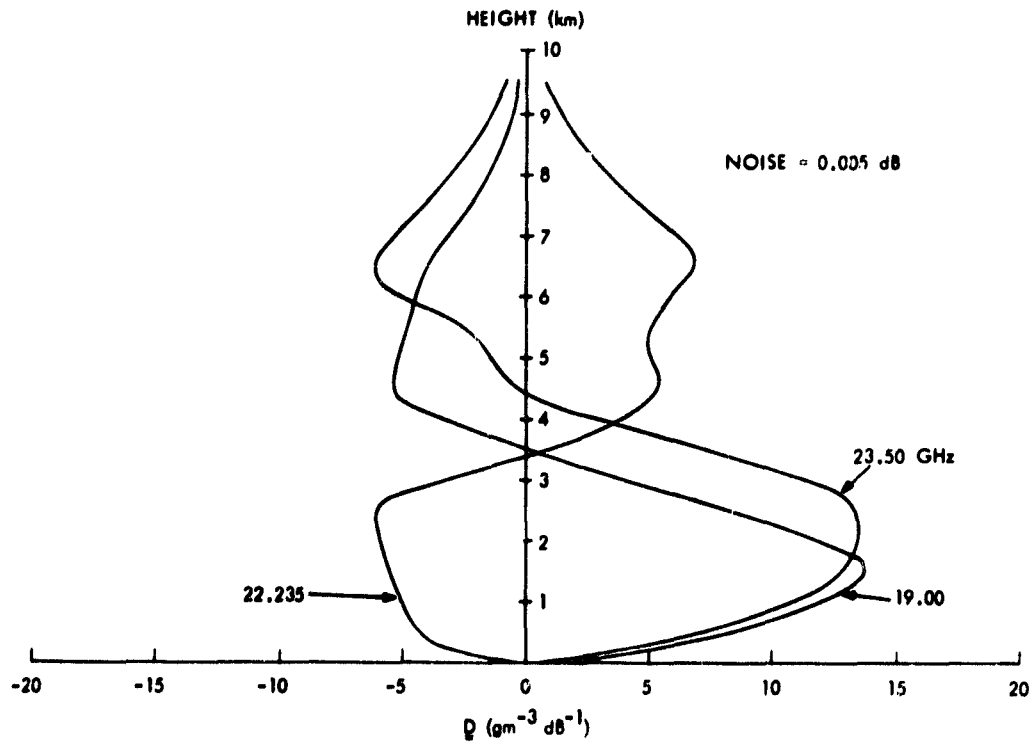Fig. 48. **D** matrix that expects no noise.

Fig. 49. **D** matrix that expects 0.005 dB of noise in each radiometer channel.

substantially. Small errors in any one channel would be much less important if the noise-stabilized $\underline{D}$ operator were to be used.

To illustrate the effect of noise on the water-vapor estimate itself, Fig. 50 has been prepared. The solid curve is the radiosonde profile; the dotted curve is a result of using the $\underline{D}$ operator that expects no noise; and the dashed curve portrays the expected water-vapor profile when noise is expected in the data. The data input was calculated from the radiosonde information; therefore, it represented essentially noiseless data.
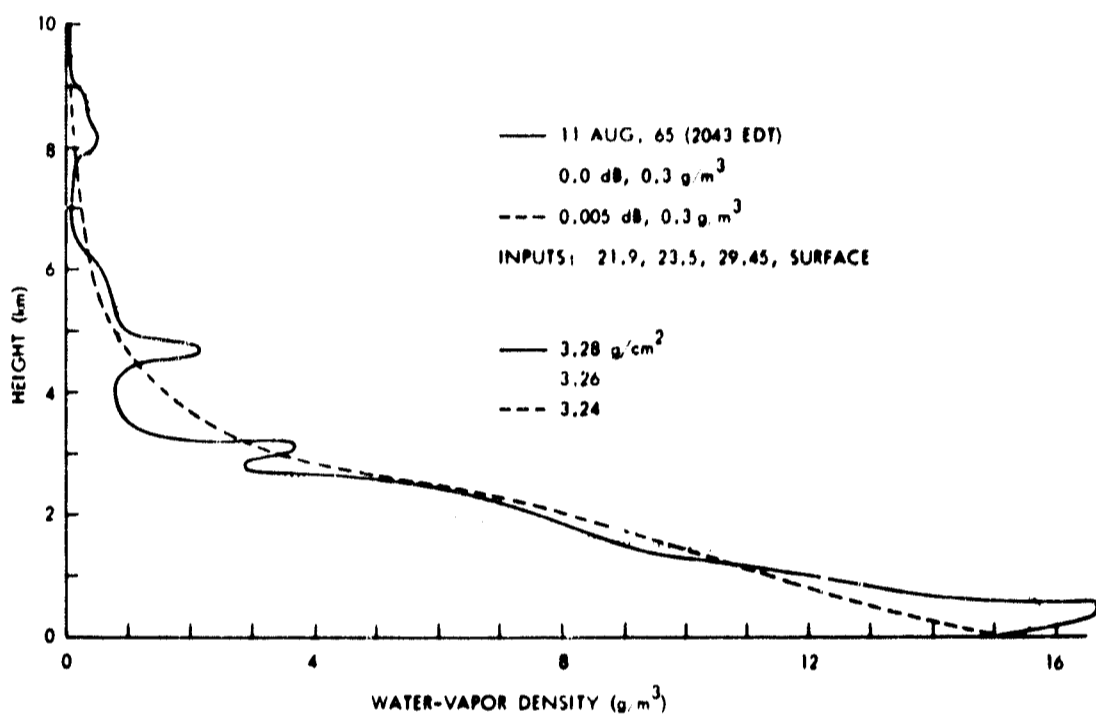
Fig. 50. Effect of expected noise on the inversior ^{f} noiseless spectral data.

The noiseless inversion is particularly good. It picks up the inversion near the surface and faithfully follows the abrupt change in the vertical gradient between 3 km and 4 km in height. It even follows the trend of the ta in the highest 4 km. The noisy inversion is good, but many details are lost: the ... /ersion is gone, and the profile is considerably smoothed.

A general feature is evident in the smooth profile: for small values of noise the noisy inversion always tends toward the shape of the mean profile of water vapor contained in the diagonal terms of $\underline{\underline{C}}_p$. This can be understood by realizing that the noise correlation matrix $\underline{\underline{C}}_n$ contains only diagonal terms, and when added to $\underline{\underline{C}}_o$ tends, for small values of noise, to enhance the diagonal terms of $\underline{\underline{C}}_o$. These contain information about the mean profile. Infinite noise would drive the solution to zero everywhere. This last feature is undesirable and can be remedied by using Eqs. 141-143, as we have pointed out. Then in the case of infinite noise a $\underline{D}$ operator that assumes infinite noise merely returns the mean profile, as it should when no information except a priori statistics is available.

7.3.2 Effects of the Number of Data Channels on Inversion Results

Figure 51 illustrates how an increase in the number of radiometer data channels improves the inversion results. This figure is a plot of the rms error between observed vapor profiles and profiles inferred from the radiometer data. Curve 1 shows the standard deviation in the atmospheric water-vapor statistics over the 34 radiosondes, in order to provide a basis for judging the effectiveness of the inversions. Curve 2 illustrates the inversion results when using a single channel at 21.0 GHz. Reduction from the a priori standard deviation is good up to, perhaps, 4 km, then is somewhat poorer above. The two-channel case (21.0 GHz and 21.9 GHz) offers substantial improvement everywhere except at the surface, between 2 km and 3 km and at very high levels. The three-frequency case shows no improvement over the two-frequency case. The inversion of three frequencies of data was somewhat unstable, and, therefore, some expected noise was introduced to reduce this instability.

The estimation of integrated water vapor was equally good in all configurations of the inversion scheme. This illustrates the strong linearity between integrated water vapor and attenuation at these frequencies.

The effect of introducing the surface measurement of the water-vapor density as a
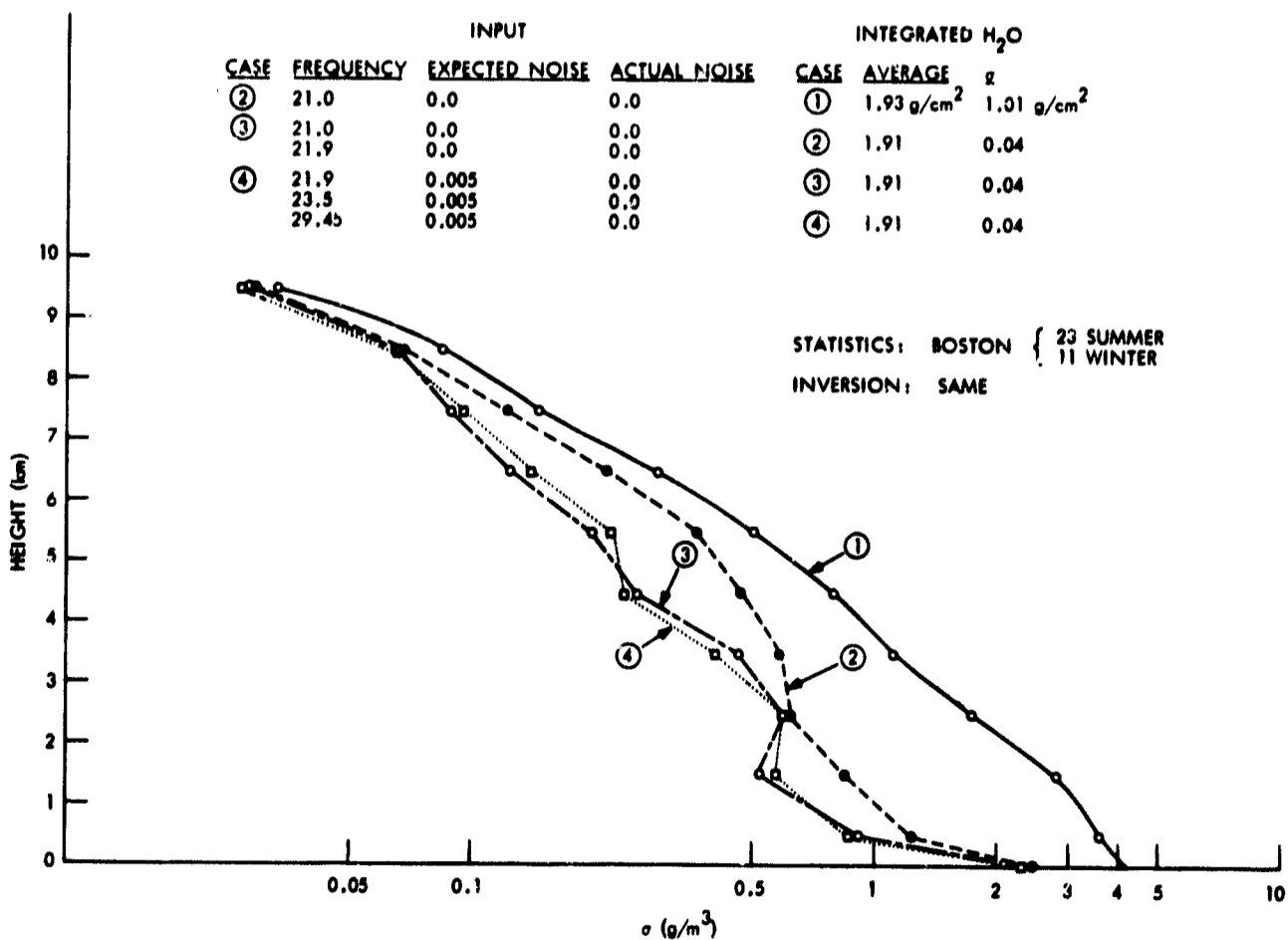

Fig. 51. Effect on the inversion statistics of the number of radiometer data channels.
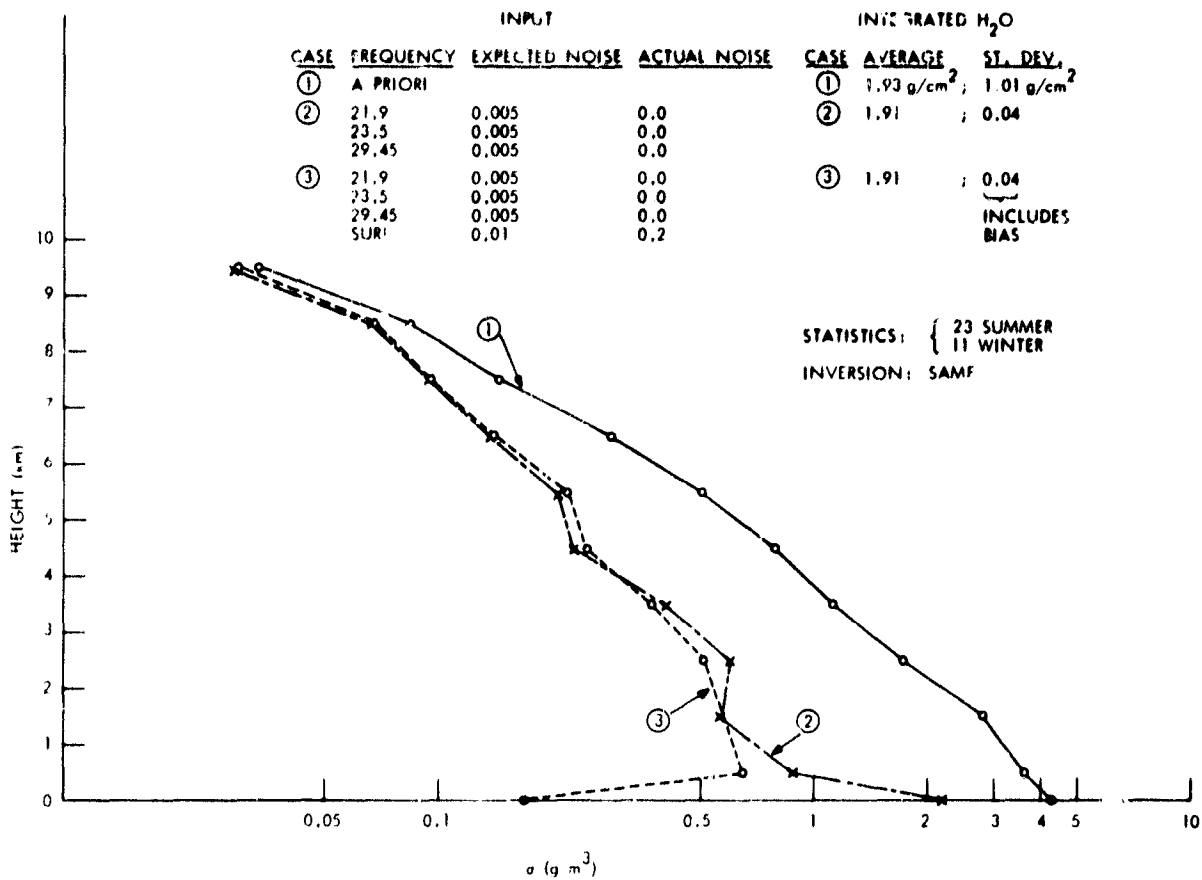
Fig. 52. Effect on the linear inversion process of including a measurement of the surface water-vapor density.
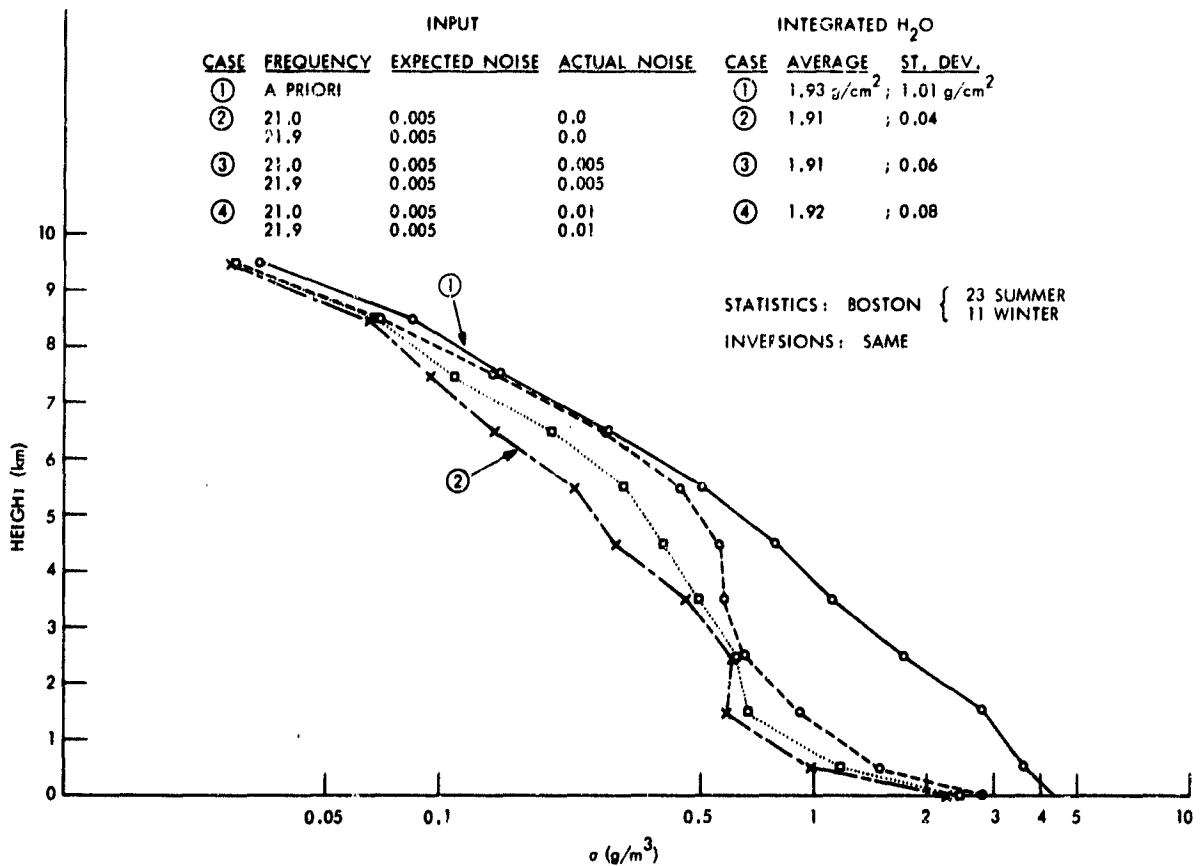
Fig. 53. Effect of noise in the data on the inversion process.

data point is illustrated in Fig. 52. As expected, the rms error at the surface is dramatically reduced. Furthermore, the inversion is improved slightly throughout the lowest layers, because of correlations between the water vapor at the surface and at other levels.

7.3.3 Effect of Noise in the Data on Inversion Results

All observed data are noisy. Therefore one of the important characteristics that an inversion scheme should show is stability in the presence of noise in the data. Figure 53 illustrates the effect of noise on a set of inversions. In each case the linear operator $\underline{D}$ is computed with the expectation that randomly distributed noise will be added to each true value of the water-vapor absorption which is being used in the inversions. The characteristics of the simulated noise are Gaussian with zero mean and various standard deviations: 0.0 dB, 0.005 dB, and 0.01 dB. The expected noise in each case is 0.005 dB for both channels.

Figure 53 shows that inversion accuracy decreases for an increase in the noise, as expected. But even for levels of noise which are double that expected (0.01 dB actual versus 0.005 dB expected), the inversions remain quite stable and return substantial information.

7.3.4 Effect of Incompatible Statistics

In Fig. 54 an example of the effect of highly incompatible statistics on the inversion process is shown. The eleven winter radiosondes were used to derive all statistics for

Fig. 54. Effect of incompatible statistics on the inversion produced by the Optimum Linear Estimator.

Fig. 55. Inversion from observed spectral data taken on a summer day.

Fig. 56. Inversion from observed spectral data taken on a winter day.

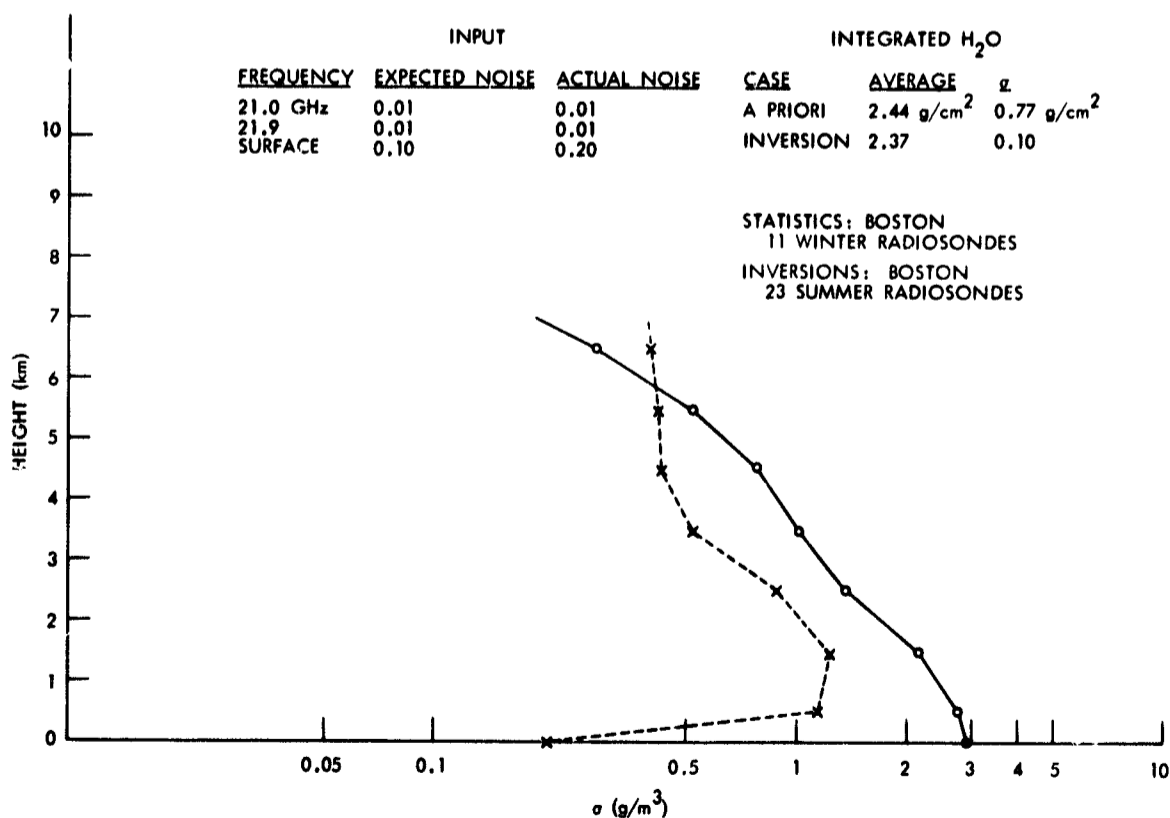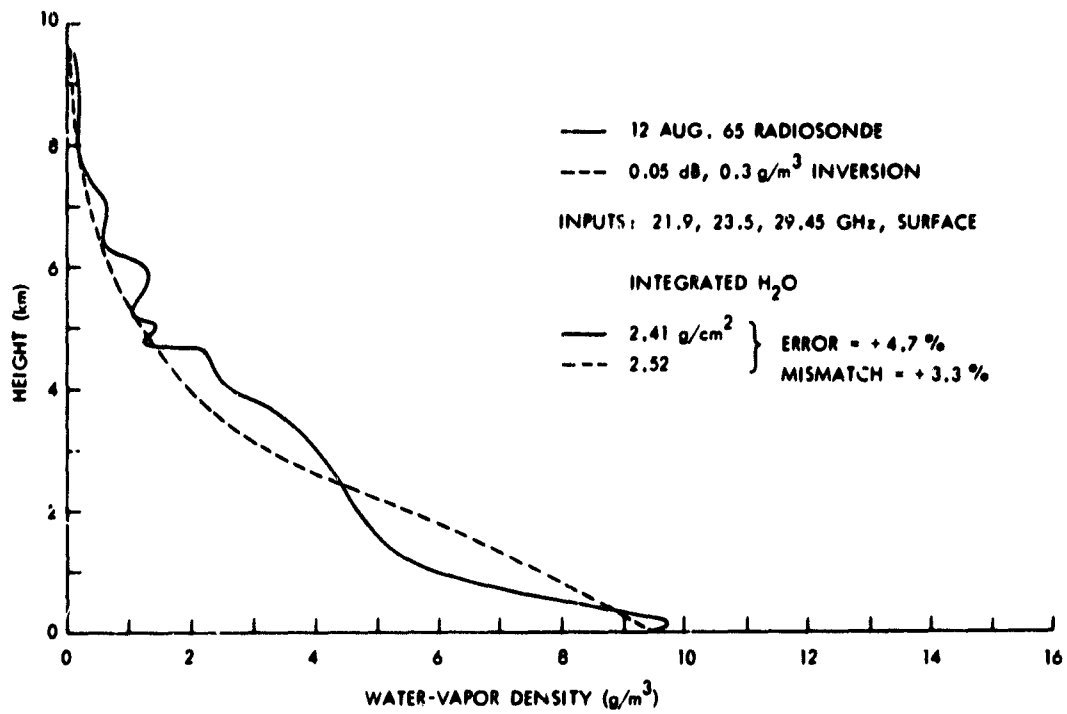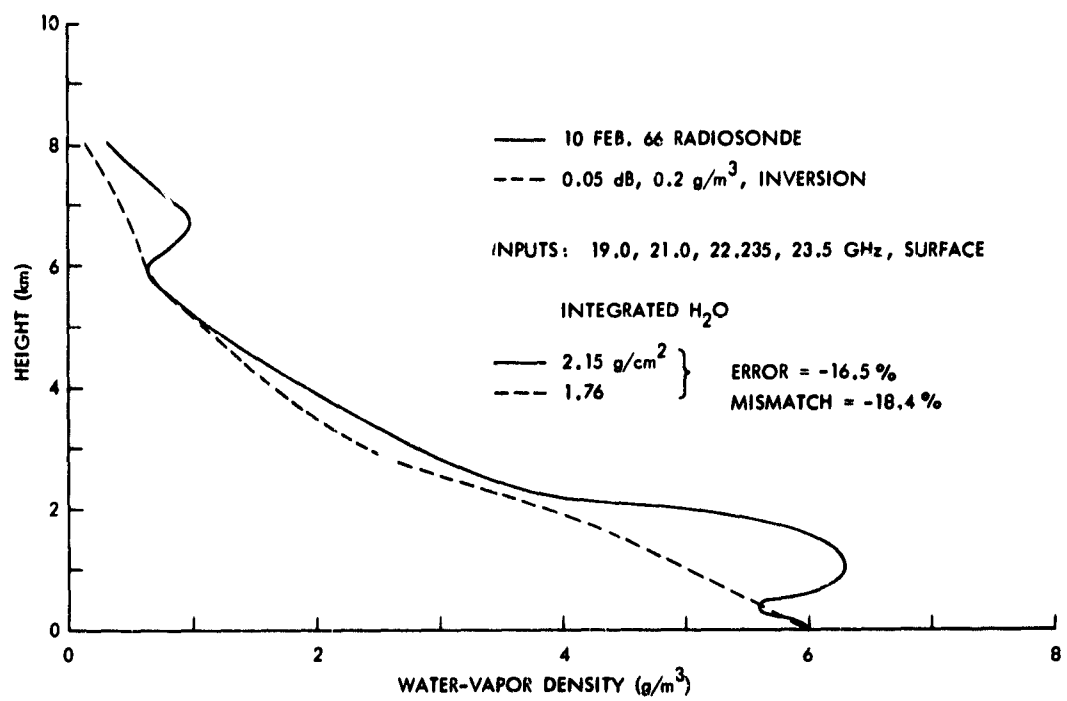the Optimum Linear Estimator. They were predominantly of very low total water vapor (average integrated water vapor: winter = 0.89 g/cm^2; summer = 2.44 g/cm^2). The statistics for the levels above 7 km did not exist and, therefore, these levels were ignored. Even with these crude statistics, the inversions showed considerable improvement over the climatology of the summer radiosondes (totally unknown to the estimation technique) in the lowest 6 km. Above this level, the statistical information was too poor to provide information over the summer climatology.

7.3.5 Inversion of Real Radiometer Data

If one were to simply invert the spectral data collected and reported in Section IV, it would be difficult to evaluate the results because, as we have shown, the radiosonde data do not furnish a good standard of comparison. Therefore 2 days of spectral data having reasonably closely matched radiosonde absorption spectra have been chosen to illustrate the inversion of real data. One day is in summer, the other in winter.

Figure 55 shows the inversion of real radiometer data for the summer day. The inversion profile is derived from a $\underline{\underline{D}}$ matrix that expected 0.05 dB of noise per channel and an error in the ground measurement of water-vapor density of 0.3 g/m^3. Because of the high level of noise expected, the inversion shape approximates the mean profile and, therefore, misses most of the secondary variations in the curve of the real profile. The integrated water-vapor estimate is high by 4.7%. The radiosonde absorption, however, was approximately 3.3% below the observed attenuation. This could mean that the integrated water-vapor estimation error might have been less than 4.7%.

The winter inversion is shown in Fig. 56. Two substantial increases of water vapor with height are not detected. Again the shape of the inversion curve is constrained by the expected noise to a profile similar to the mean. The integrated water vapor is low by 16.5%. The mismatch, however, between observed attenuation and radiosonde absorption amounted to approximately 18.4%, so that it is difficult to assess the true significance of this poor estimation.

It is clear that the fine structure in the atmospheric water-vapor profiles will not be recoverable from radiometer data. And, it is clear that with noisy data, most of the major variations from the mean profile will also be difficult to detect. The integrated water vapor and general profile, even with noisy data, however, should be generally accurate and, for most meteorological purposes, quite useful.

APPENDIX A

Water-Vapor Rotational Spectral-Line Parameters

In Table 7, all of the constants that are needed to compute the absorption for the 54 lowest frequency rotational spectral lines of water vapor are listed. An asterisk indicates that the frequencies have been experimentally determined; otherwise, they are taken from Ghosh and Edwards.[68] Term values are taken from Dennison.[27] Line strengths are those computed by King, Hainer, and Cross.[6] Linewidths for air are those that Benedict and Kaplan[20] computed for nitrogen without correction. The temperature exponents are also from Benedict and Kaplan.[20] The linewidths in water vapor are from later work of Benedict and Kaplan[24] on oxygen and water vapor. Values in parentheses in column 6 are estimates from graphs drawn on the basis of the tables of line strengths for various asymmetry parameters computed by Wacker and Pratto.[7] Numbers in parentheses in columns 7-9 are estimates for the lines involved based on averages over similarly arising lines.

Table 7. Water-vapor rotational spectral-line parameters.

FREQUENCY (MHz)	TRANSITION	PARITY	LOWER TERM VALUE (cm^{-1})	UPPER TERM VALUE (cm^{-1})	LINE STRENGTH	LINEWIDTH (AIR) cm^{-1} atm^{-1}	TEMP. EXP.	LINEWIDTH (WATER VAPOR) cm^{-1} atm^{-1}
22,235.22*	$5_{23} \rightarrow 6_{16}$	eo → oe	446.39	447.17	0.0549	.09019	.626	0.4777
183,310.12*	2_{20} 3_{13}	ee → oo	136.15	142.30	0.1015	.09600	.649	0.4937
323,158.5	9_{26} 10_{29}	oe → eo	1283.02	1293.80	(0.087)	.07652	.42	0.4012
323,758.1	4_{32} 5_{15}	ee → oo	315.70	326.50	0.0891	.09292	.619	0.5071
377,418.0	3_{21} 4_{14}	eo → oe	212.12	224.71	0.1224	.09480	.63	0.5280
389,708.8	11_{48} 10_{37}	ee → oo	1525.31	1538.31	(0.068)	.0702	.33	0.3807
435,874.3	6_{61} 7_{52}	ee → oo	1045.14	1059.68	(0.082)	.0500	.29	0.2648
437,673.0	5_{50} 6_{43}	oe → eo	742.18	756.78	0.0987	(.059)	(.36)	(0.3348)
441,570.0	6_{61} 7_{52}	eo → oe	1045.14	1059.87	(0.082)	.05023	.332	0.2709
445,766.9	3_{30} 4_{23}	oe → eo	285.46	300.33	0.1316	.08247	.510	0.4748
465,851.9	5_{51} 6_{42}	oo → eo	742.18	757.72	0.0990	.0629	.38	0.3521
470,948.1	4_{40} 5_{33}	ee → oo	488.19	503.90	0.1165	.0690	.38	0.3987
487,136.0	7_{17} 6_{24}	oo → ee	586.46	602.71	(0.033)	.0861	.51	0.4926
498,527.5	7_{70} 8_{63}	oe → eo	1394.96	1411.59	(0.077)	.0424	.32	0.2051
498,527.5	7_{71} 8_{62}	oo → ee	1394.96	1411.59	(0.072)	.0424	.34	0.205
557,583.4	1_{01} 1_{10}	eo → oe	23.76	42.36	1.5000	.11115	.645	0.4889
617,838.3	4_{41} 5_{32}	eo → oe	483.19	508.80	0.1193	.07606	.60	0.4262
641,520.6	8_{80} 9_{73}	ee → oo	1789.36	1810.76	(0.066)	.0380	.40	0.172
641,520.6	8_{81} 9_{72}	eo → oe	1789.36	1810.76	(0.066)	.0380	.40	0.1715
752,737.5	2_{02} 2_{11}	ee → oo	70.08	95.19	2.0739	.10440	.69	0.4648
833,077.5	8_{35} 9_{28}	oo → ee	1052.72	1080.51	(0.157)	.0798	.51	0.4297
857,958.9	11_{29} 10_{56}	eo → oe	1690.74	1719.36	(0.067)	(.055)	(.20)	(0.309)
859,158.0	9_{46} 10_{19}	oe → eo	2225.87	2254.53	(0.059)	.0357	.48	(0.1535)
859,158.0	9_{47} 10_{18}	oo → ee	2225.87	2254.53	(0.059)	.0357	.48	0.1533
912,518.1	3_{31} 4_{22}	oo → ee	285.26	315.70	0.1613	.08638	.676	0.4689
961,381.6	4_{31} 5_{24}	oo → ee	383.93	416.00	0.2622	.08262	.56	0.4722
987,462.1	1_{11} 2_{02}	oo → ee	37.14	70.08	0.7557	.10316	.660	0.5069

1,077,394.9	$12_{2,11}$	11_{38}	eo → oe	1774.85	1810.79	(0.042)	.061	.25	0.3476
1,098,379.3	3_{03}	3_{o12}	eo → oe	136.74	173.38	2.1809	.09944	.701	0.5590
1,107,672.3	10_{25}	9_{55}	ee → oo	1438.19	1475.14	(0.050)	(.061)	(.25)	(0.631)
1,113,368.1	0_{oo}	1_{11}	ee → oo	0.00	37.14	1.0000	.10034	.689	0.5026
1,142,746.1	$10_{10,0}$	11_{q3}	ee → oo	2702.61	2740.73	(0.054)	(.03434)	(.503)	(0.1297)
1,142,746.1	$10_{10,1}$	11_{q2}	eo → oe	2702.61	2740.73	(0.054)	.03434	.503	0.1297
1,145,743.9	8_{ib}	7_{25}	oe → eo	744.20	782.42	(0.025)	.08008	.498	0.4563
1,154,137.6	2_{21}	3_{m}	eo → oe	134.88	173.38	0.3003	.09515	.61	0.5485
1,159,833.3	5_{41}	6_{34}	eo → oe	610.34	649.03	0.2784	.07131	.399	0.4229
1,161,332.2	3_{12}	3_{21}	oe → eo	173.38	212.12	2.5434	.09487	.682	0.5060
1,163,430.7	7_{61}	8_{54}	eo → oe	1216.38	1255.19	(0.223)	.0516	.29	0.2908
1,169,726.0	6_{51}	7_{44}	oo → ee	388.74	927.76	(0.252)	.0648	.36	(0.374)
1,187,113.0	7_{62}	8_{53}	ee → oo	1216.38	1255.98	(0.223)	.0542	.30	0.3061
1,208,996.6	8_{71}	9_{63}	oo → ee	1591.11	1631.44	(0.199)	.0445	.32	0.2381
1,213,193.5	8_{72}	9_{63}	oe → eo	1591.11	1631.58	(0.199)	.0447	.34	0.2411
1,213,193.5	4_{13}	4_{22}	oo → ee	272.23	315.70	3.6547	.09507	.72	0.5091
1,227,882.5	2_{11}	2_{20}	oo → ee	95.19	136.15	1.2594	.09792	.67	0.4658
1,227,945.1	6_{52}	7_{43}	oe → eo	888.70	931.33	(0.253)	.0688	.45	0.2682
1,294,432.8	7_{61}	8_{27}	oe → eo	842.51	885.69	(0.184)	.0819	.55	0.4577
1,309,721.3	9_{18}	8_{45}	oe → eo	1079.20	1122.89	(0.047)	(.060)	(.25)	(0.34?)
1,323,211.3	5_{32}	6_{25}	oe → eo	508.80	552.94	0.3117	.08313	.571	0.4939
1,329,806.3	9_{81}	10_{74}	eo → oe	2010.19	2054.55	(0.173)	.0390	.39	0.2077
1,329,806.3	9_{82}	10_{73}	ee → oo	2010.19	2054.55	(0.173)	.0390	.39	0.2077
1,342,696.7	8_{17}	7_{44}	oo → ee	882.97	927.76	(0.036)	(.066)	(.30)	(0.375)
1,407,448.3	5_{14}	5_{23}	oe → eo	399.44	446.39	4.2239	.09470	.722	0.5123
1,423,336.4	10_{19}	9_{46}	oo → ee	1293.22	1340.70	(0.059)	(.055)	(.24)	(0.322)
1,435,927.0	6_{33}	7_{26}	oo → ee	661.54	709.44	(0.258)	.0830	.59	0.4542

APPENDIX B

Absorption Coefficient for Oxygen

The regions of the electromagnetic spectrum in which we are chiefly concerned do not include resonances of any other important atmospheric constituent. The wings of the 5-mm complex of magnetic dipole resonances of oxygen, however, are strong enough that their effect must be taken into account in the region near the lowest water-vapor resonance at 1.35 cm. Near 1.64 mm the only absorption of potential consequence besides that of the water-vapor resonance at 183 GHz is contributed by the high-frequency wing of the single oxygen resonance near 2.5 mm. The strength of the oxygen absorption is so slight, however, when compared with the water-vapor absorption that it may be safely neglected for all normal computations.

Since oxygen absorption cannot be totally neglected, it is necessary to provide a working expression to compute its value under atmospheric conditions. The equations given here are taken from Meeks and Lilley,[48] and they, together with Van Vleck,[2] should be consulted for a detailed account of how the equations were derived.

The oxygen molecule has two electrons with unpaired spin. They contribute to a magnetic dipole moment of total strength 2 Bohr magnetons and spin angular momentum quantum number $S = 1$. The dumbbell-shaped oxygen molecule rotates end over end with angular momentum described by odd values of the quantum number N, even values not being permitted by the Pauli exclusion principle. The total angular momentum is the vectorial sum between N and S. Therefore, for a given rotational quantum number N, a total rotational quantum number J may have the values N-1, N, or N+1, depending upon the orientation of S with respect to N. Each of the states of total angular momentum has slightly different energies. Selection rules allow transitions between $(J=N) \rightarrow (J=N+1)$ and $(J=N) \rightarrow (J=N-1)$, the resonant frequencies of which all cluster about the region of 5 mm, except for only one transition whose resonant frequency occurs near 2.5 mm.

The expression for the absorption by these fine-structure transitions is given by

$$\gamma_{O_2}(\nu, P, T) = C_1 P T^{-3} \nu^2 \sum_N S_N \exp(-E_N/kT), \tag{B.1}$$

where γ_{O_2} is the absorption coefficient for oxygen at a given frequency ν, atmospheric pressure P, and atmospheric temperature T. The summation is taken over all N states of non-negligible population, usually up to $N = 45$. The definitions of the other terms in (B.1) are

$$S_N = F_{N+}\mu_{N+}^2 + F_{N-}\mu_{N-}^2 + F_o\mu_{N_o}^2, \tag{B.2}$$

in which N+ and N- refer to the transitions $N \rightarrow N+1$ and $N \rightarrow N-1$, respectively, and the F and the μ have the meanings

$$F_{N\pm} = \frac{\Delta\nu}{(\nu_{N\pm}-\nu)^2 + \Delta\nu^2} + \frac{\Delta\nu}{(\nu_{N\pm}+\nu)^2 + \Delta\nu^2} \tag{B.3}$$

$$F_o = \frac{\Delta\nu}{\nu^2 + \Delta\nu^2} \tag{B.4}$$

$$\mu_{N+}^2 = \frac{N(2N+3)}{N+1} \tag{B.5}$$

$$\mu_{N-}^2 = \frac{(N+1)(2N+1)}{N} \tag{B.6}$$

$$\mu_{N_o}^2 = \frac{2(N^2+N+1)(2N+1)}{N(N+1)}. \tag{B.7}$$

The argument of the exponential function may be written

$$E_N/kT = 2.06844\,N(N+1)/T. \tag{B.8}$$

For γ_{O_2} to be given in decibels per kilometer, C_1 takes the value

$$C_1 = 2.0058$$

when the pressure is in millibars, the temperature is in degrees Kelvin, and the frequency is in gigacycles.

The linewidth $\Delta\nu$, as in the case for water vapor, is proportional to the pressure, but has peculiar properties, because of the very strong overlap of the various individual lines at pressures found in the atmosphere below approximately 30 km. The expression for the linewidth may be written

$$\Delta\nu(P, T) = aP[0.21 + 0.8\beta]\left[\frac{300}{T}\right]^{0.85}, \tag{B.9}$$

with the empirically derived values for a and β as follows:

$a = 1.44$ MHz/mb

$\beta = 0.25;$ for $z < H_1$ ($P > 356$ mb)

$\beta = 0.25 + 0.50\,(h-H_1)/(H_2-H_1);$ for $H_1 \leqslant z \leqslant H_2$

$\beta = 0.75;$ for $z > H_2$ ($P < 25.3$ mb),

where z refers to height above ground, P the total pressure in millibars, and T the temperature in degrees Kelvin.

Acknowledgment

References

1. E. N. Lorenz, "The Predictability of a Flow Which Possesses Many Scales of Motion" (submitted to _Tellus_, 1968).

2. J. H. Van Vleck, "The Absorption of Microwaves by Oxygen," Phys. Rev. _71_, 7 (1947).

3. G. Herzberg, _Molecular Spectra and Molecular Structure: II. Infrared and Raman Spectra of Polyatomic Molecules_ (D. Van Nostrand Co., Princeton, N.J. (1945); especially see Chap. V.

4. C. H. Townes and A. L. Schawlow, _Microwave Spectroscopy_ (McGraw-Hill Book Company, Inc., New York (1955); especially see Chap. 4; also see Eq. 4-25, and p. 102f.

5. J. H. Van Vleck, "The Absorption of Microwaves by Water Vapor," Phys. Rev. _71_, 7 (1947); especially see p. 427.

6. G. W. King, R. M. Hainer, and P. C. Cross, "Expected Microwave Absorption Coefficients of Water and Related Molecules," Phys. Rev. _71_, 7 (1947).

7. P. F. Wacker and M. R. P·atto, _Microwave Spectral Tables; Line Strengths of Asymmetric Rotors_, NBS Monograph 70, Vol. II (U. S. Government Printing Office, Washington, D.C., 1964).

8. H. A. Lorentz, Proc. Amsterdam Akad. Sci. _8_, 591 (1906).

9. J. H. Van Vleck and V. F. Weisskopf, "On the Shape of Collision Broadened Lines," Rev. Mod. Phys. _17_, Nos. 2 and 3 (1945).

10. P. W. Anderson, "Pressure Broadening in the Microwave and Infra-Red Regions," Phys. Rev. _76_, 5 (1949).

11. A. Ben-Reuven, "Transition from Resonant to Nonresonant Line Shape in Micro-wave Absorption," Phys. Rev. Letters _14_, 10 (1965).

12. S. A. Zhevakin and A. P. Naumov, Izvestiya Vuzov (Radiofizika) _6_, 674 (1963).

13. R. G. Gordon, "On the Pressure Broadening of Molecular Multiplet Spectra," J. Chem. Phys. _46_, 448-455 (1967).

14. G. Birnbaum and A. A. Maryott, J. Chem. Phys. _21_, 1774 (1953).

15. A. H. Nethercot, J. A. Klein, J. H. N. Loubser, and C. H. Townes, Nuovo Cimento _9_, Suppl. 3, 358 (1952).

16. G. E. Becker and S. H. Autler, "Water Vapor Absorption of Electromagnetic Radiation in the Centimeter Wave-Length Range," Phys. Rev. _70_, Nos. 5 and 6 (1946).

17. L. Frenkel and D. Woods, "The Microwave Absorption by H_2O Vapor and Its Mixtures with Other Gases between 100 and 300 Gc/s," Proc. IEEE _54_, 4 (1966).

18. C. D. Hodgman (ed.), _Handbook of Chemistry and Physics_ (Chemical Rubber Publishing Company, Cleveland, Ohio, 38th edition, 1956).

19. C. H. Townes and F. R. Merritt, "Water Spectrum near One-Centimeter Wave-Length," Phys. Rev. _70_, 558L (1946).

20. W. S. Benedict and L. D. Kaplan, "Calculation of Line Widths in H_2O-N_2 Collisions," J. Chem. Phys. _30_, 2 (1959).

21. J. H. Van Vleck, in _Propagation of Short Radio Waves_, D. E. Kerr (ed.) (Dover Publications, Inc., New York, 1951); especially see footnote p. 661.

22. J. R. Rusk, J. Chem. Phys. _42_, 493 (1965); see also "Letters," J. Chem. Phys. _43_, 2919 (1965).

23. C. Hemmi, "Pressure Broadening of the 1.63 mm Water Vapor Absorption Line," Technical Report 1, Electrical Engineering Research Laboratory, University of Texas, Austin, Texas, 1966.

24. W. S. Benedict and L. D. Kaplan, "Calculation of Line Widths in H_2O-H_2O and H_2O-O_2 Collisions," J. Quart Spec. Rad. Trans. 4, 453-469 (1964).[2]

25. (a) Ibid., p. 466; (b) p. 465.

26. W. S. Benedict and L. D. Kaplan, J. Chem. Phys. 30 (1959), see p. 395.

27. D. M. Dennison, "Infra-Red Spectra of Polyatomic Molecules," Rev. Mod. Phys. 12, 175 (1940).

28. P. Debye, Polar Molecules (Dover Publications, Inc., New York, 1959).

29. R. v. D. R. Woolley and D. W. N. Stibbs, The Outer Layers of a Star (Oxford University Press, London, 1953).

30. M. Planck, The Theory of Heat Radiation (Dover Publications, Inc., New York, 1959).

31. R. M. Goody, Atmospheric Radiation: I - Theoretical Basis (Oxford Press, London, 1964).

32. S. L. Valley, Handbook of Geophysics and Space Environment, Air Force Cambridge Research Laboratories, Bedford, Mass., 1965; see Chap. 5 for details of these atmospheres.

33. D. H. Staelin, in "Meteorological Experiments for Manned Earth Orbiting Missions," Final Report Contract NASW-1292 by Geophysics Corporation of America, G. Ohring (ed.) (NASA, Washington, D.C., 1966).

34. R. H. Dicke, R. Beringer, R. L. Kyhl, and A. B. Vane, "Atmospheric Absorption Measurements with a Microwave Radiometer," Phys. 70, 340 (1946).

35. D. H. Staelin, Quarterly Progress Report No. 78, Research Laboratory of Electronics, M.I.T., Cambridge, Mass., July 15, 1965, pp. 24-27.

36. E. W. Barrett, L. R. Herndon, and H. J. Carter, "Some Measurements of the Distribution of Water Vapor in the Stratosphere," Tellus 2, 302-311 (1950).

37. D. G. Murcray, F. H. Murcray, W. J. Williams, and F. E. Leslie; J. Geophys. Res. 65, 3641-3650 (1960).

38. H. J. Mastenbrook and J. E. Dinger, "Distribution of Water Vapor in the Stratosphere," J. Geophys. Res. 66, 1437-1444 (1961).

39. A. H. Barrett and V. K. Chung, "A Method for the Determination of High Altitude Water Vapor Abundance from Ground Based Microwave Observations," J. Geophys. Res. 67, 11 (1962).

40. L. A. Bonvini, D. L. Croom, and A. Gordon-Smith; their results are referred to in D. L. Croom, J. Atm. Terr. Phys. 28, 323-326 (1966).

41. M. Gutnick, "How Dry the Sky?," J. Geophys. Res. 66, 2867-2871 (1961).

42. H. J. Mastenbrook, "Water Vapor Observations at Low, Middle, and High Latitudes during 1964 and 1965," NRL Report 6447, Naval Research Laboratory, Washington, D.C., 1966.

43. N. Sissenwine, D. D. Grantham, and H. A. Salmela, "Mid-Latitude Stratospheric Humidity Regime to 30 Km," Interim Notes on Atmospheric Properties No. 73, Air Force Cambridge Research Laboratories, Bedford, Mass., 1966.

44. M. J. Long, "A Preliminary Climatology of Thunderstorm Penetrations of the Tropopause in the United States," J. Apl. Met. 5, 467-473 (1966).

45. E. C. May and A. B. Kahle, "The Satellite Determination of High Altitude Water Vapor," NASA Contractor Report CR-70, Office of Technical Services, Washington, D.C., 1964.

46. D. L. Croom, J. Atm. Terr. Phys. 28, 323-326 (1966); 27, 217-233; 235-243 (1965).

47. N. E. Gaut, "Studies of Atmospheric Water Vapor by Means of Passive Microwave Techniques," Ph. D. Thesis, Department of Meteorology, Massachusetts Institute of Technology, July 17, 1967.

48. M. L. Meeks and A. E. Lilley, "The Microwave Spectrum of Oxygen in the Earth's Atmosphere," J. Geophys. Res. 68, 6 (1963).

49. L. D. Kaplan, J. Opt. Soc. Am. 49, 10 (1959).

50. W. B. Lenoir, Ph. D. Thesis, Massachusetts Institute of Technology, 1965.

51. C. D. Rodgers, "A Discussion of Inversion Methods," Mem. 66. 13, Clarendon Laboratory, Oxford University, 1966.

52. J. I. F. King, Atm. Sci. 21, 324-326 (1964).

53. D. Q. Wark, J. Geophys. Res. 66, 77-82 (1961).

54. D. Q. Wark and H. E. Fleming, "Indirect Measurements of Atmospheric Temperature Profiles from a Satellite," Mon. Wea, Rev. 94, 351-362 (1966).

55. R. M. Goody, The Physics of the Stratosphere (Cambridge University Press, London, 1958).

56. D. H. Staelin, J. Geophys. Res. 71, 2875-2881 (1966).

57. E. Raschke, NASA Contractor Report 595, Goddard Space Flight Center, Washington, D. C. , 1966.

58. F. Moller, Plan. Space Sci. 5, 202-206 (1961).

59. See, for example, W. Nordberg, A. W. McCulloch, L. L. Foshee, and W. R. Bandeen, Bull. Am. Met. Soc. 47, 11 (1966).

60. W. Nordberg, Science 150, 559-572 (1965).

61. C. S. Cox and W. H. Munk, J. Opt. Soc. Am. 44, 838-850 (1954).

62. B. R. Fow and W. D. Mount, "A Feasibility and Design Study for an Airborne Radiometric System to Measure Remotely the Vertical Profile of Temperature, Humidity and Pressure," AFCRL-68-0107, Sperry-Rand Research Center, Sudbury, Mass. , 1968.

63. A. H. Barrett, "Microwave Studies of the Terrestrial Atmosphere," Research Laboratory of Electronics, M. I. T. , 1964 (unpublished manuscript).

64. E. R. Westwater and O. N. Strand, "Application of Statistical Estimation Techniques to Ground-Based Passive Probing of the Tropospheric Temperature Structure," ESSA Technical Report IER 37/ITSA 37, 1965.

65. D. H. Staelin (Private communication, 1967).

66. J. W. Waters and D. H. Staelin, Quarterly Progress Report No. 89, Research Laboratory of Electronics, M. I. T. , Cambridge, Mass. , April 15, 1968, pp. 25-28.

67. D. H. Staelin, Quarterly Progress Report No. 85, Research Laboratory of Electronics, M. I. T. , Cambridge, Mass. , April 15, 1967, pp. 15-16.

68. S. N. Ghosh and H. D. Edwards, "Rotational Frequencies and Absorption Coefficients of Atmospheric Gases," Air Force Survey in Geophysics, Vol. 82, Air Force Cambridge Research Laboratories, Bedford, Mass. , 1958.

DOCUMENT CONTROL DATA · R & D

Security classification of title, body of abstract and indexing annotation must be entered when the overall report is classified)

1. ORIGINATING ACTIVITY (Corporate author)	2a. REPORT SECURITY CLASSIFICATION
Research Laboratory of Electronics Massachusetts Institute of Technology Cambridge, Massachusetts 02139	Unclassified
	2b. GROUP None

3. REPORT TITLE

Studies of Atmospheric Water Vapor by Means of Passive Microwave Techniques

4. DESCRIPTIVE NOTES (Type of report and inclusive dates)

Technical Report

5. AUTHOR(S) (First name, middle initial, last name)

Norman E. Gaut

6. REPORT DATE	7a. TOTAL NO. OF PAGES	7b. NO. OF REFS
December 20, 1968	112	68

8a. CONTRACT OR GRANT NO. DA 28-043-AMC-02536(E) b. PROJECT NO. 200-14501-B31F NASA Grant NGL 22-009-016	9a. ORIGINATOR'S REPORT NUMBER(S) Technical Report 467
	9b. OTHER REPORT NO(S) (Any other numbers that may be assigned this report) None

10. DISTRIBUTION STATEMENT

Distribution of this report is unlimited.

11. SUPPLEMENTARY NOTES	12. SPONSORING MILITARY ACTIVITY Joint Services Electronics Program thru USAECOM, Fort Monmouth, N.J.

13. ABSTRACT

Expressions describing the absorption by water vapor near its two lowest rotational spectral lines (22.235 GHz and 183.310 GHz) have been developed. These expressions are used to investigate the absorption from model and real atmospheres. Absorption measurements taken near the lower frequency line are compared with computed spectra based on data from simultaneous nearby radiosonde ascents. Comparable spectra occur only on days of high static stability. The spectral spike which excessive stratospheric water vapor might produce was searched for, but not found, in the observed absorption data. Under reasonable assumptions about the distribution of water vapor in the stratosphere, this result follows. A method for determining integrated water vapor using zenith opacity at several frequencies has been derived and evaluated. Estimations within ±5% of the true values are consistently obtainable. Finally, the statistical scheme of C. D. Rodgers (Clarendon Laboratory) for inverting spectral data in order to obtain the vertical distribution of water vapor has been evaluated for 34 radiosondes from Boston and vicinity. The procedure is shown to be stable against a variety of errors in the data and statistical assumptions.

DD FORM 1473 (PAGE 1)
1 NOV 65

S/N 0101-807-6811

14 KEY WORDS	LINK A		LINK B		LINK C	
	ROLE	WT	ROLE	WT	ROLE	WT
measurements of atmospheric attenuation						
water-vapor absorption in the atmosphere						
inversion of spectral data						
microwave emission in the atmosphere						
microwave meteorology						
water-vapor distribution from microwave measurements						